



**Titre:** Metal Injection Molding Development: Modeling and Numerical  
Title: Simulation of Injection with Experimental Validation

**Auteur:** Vincent Raymond  
Author:

**Date:** 2012

**Type:** Mémoire ou thèse / Dissertation or Thesis

**Référence:** Raymond, V. (2012). Metal Injection Molding Development: Modeling and  
Citation: Numerical Simulation of Injection with Experimental Validation [Mémoire de  
maîtrise, École Polytechnique de Montréal]. PolyPublie.  
<https://publications.polymtl.ca/1030/>

 **Document en libre accès dans PolyPublie**  
Open Access document in PolyPublie

**URL de PolyPublie:** <https://publications.polymtl.ca/1030/>  
PolyPublie URL:

**Directeurs de  
recherche:** Sylvain Turenne  
Advisors:

**Programme:** Génie mécanique  
Program:

UNIVERSITÉ DE MONTRÉAL

METAL INJECTION MOLDING DEVELOPMENT:  
MODELING AND NUMERICAL SIMULATION OF INJECTION WITH  
EXPERIMENTAL VALIDATION

VINCENT RAYMOND  
DÉPARTEMENT DE GÉNIE MÉCANIQUE  
ÉCOLE POLYTECHNIQUE DE MONTRÉAL

MÉMOIRE PRÉSENTÉ EN VUE DE L'OBTENTION  
DU DIPLÔME DE MAÎTRISE ÈS SCIENCES APPLIQUÉES  
(GÉNIE MÉCANIQUE)  
DÉCEMBRE 2012

UNIVERSITÉ DE MONTRÉAL

ÉCOLE POLYTECHNIQUE DE MONTRÉAL

Ce mémoire intitulé:

METAL INJECTION MOLDING DEVELOPMENT:  
MODELING AND NUMERICAL SIMULATION OF INJECTION WITH EXPERIMENTAL  
VALIDATION

présenté par : RAYMOND Vincent

en vue de l'obtention du diplôme de : Maîtrise ès sciences appliquées

a été dûment accepté par le jury d'examen constitué de :

Mme BROCHU Myriam, Ph.D., présidente

M. TURENNE Sylvain, Ph.D., membre et directeur de recherche

M. PELLETIER Dominique, Ph.D., membre

## ACKNOWLEDGEMENT

I would like to thank everyone at P&WC, at NRC-IMI and at *École Polytechnique Montréal* who helped me to achieve this project. Fred, Jacques, Marc, Mélissa, Orlando, Sébastien, Vincent, Éric, Florin, Jean-François and Sylvain, your support was essential to me. I would also like to acknowledge the FQRNT, CRSNG and Pratt & Whitney Canada for their financial support.

Special thanks to Sylvain and Orlando who kindly revised every versions of my master thesis.

Another special thanks to Mélissa. She gave me the opportunity to work on this challenging project and motivated me throughout the project.

Finally, I wish to thank my family for their patience and their help, especially my girlfriend.

Isa, we have every weekend now!

## RÉSUMÉ

Le moulage par injection de métal en poudre (MIM) est un nouveau procédé de fabrication prometteur dans le domaine de l'aéronautique. Le MIM permet de réduire les coûts de fabrication en éliminant la majorité des opérations d'usinage tout en conférant aux matériaux de bonnes propriétés mécaniques. Pratt & Whitney Canada (P&WC) développe ce procédé afin de fabriquer des pièces MIM pour les moteurs à turbine.

Ce procédé comporte plusieurs étapes. Une de celles-ci consiste à créer une géométrie par l'injection d'un mélange de poudres métalliques et d'un liant dans un moule. Une bonne maîtrise de cette étape est cruciale afin de produire des pièces sans défaut. Afin de diminuer le nombre de rejets et mieux comprendre l'injection, l'utilisation d'un outil de simulation numérique est idéale. Le but de ce projet est donc d'identifier un outil de simulation numérique qui pourra simuler précisément l'étape d'injection du procédé MIM de P&WC.

Les propriétés du mélange nécessaires pour la simulation ont été mesurées expérimentalement. Ensuite, plusieurs séries d'injection à l'aide d'un moule instrumenté et d'une caméra haute vitesse ont permis d'obtenir les données expérimentales nécessaires pour la validation de la simulation. Finalement, à l'aide de Plasview3D, des simulations ont été exécutées avec les propriétés expérimentales du mélange.

Les résultats obtenus sous-estiment grandement le temps de remplissage, mais les profils de pression calculés sont similaires à ceux acquis avec le moule instrumenté. Grâce à une analyse de sensibilité, le modèle de viscosité a été identifié comme une des causes potentielles pour expliquer les écarts observés. En modifiant le niveau de viscosité du modèle par un facteur de 2.5 pour toutes les vitesses de cisaillement, les résultats de la simulation corrèlent bien les résultats expérimentaux obtenus avec deux moules différents. La condition d'entrée a aussi été étudiée et une solution a été proposée afin d'obtenir des résultats plus fidèles.

En conclusion, l'utilisation de Plasview3D a démontré que la simulation de l'injection est possible pour le procédé MIM de P&WC. Cependant, davantage de travaux de caractérisation du mélange, surtout au niveau rhéologique, seront requis afin d'obtenir des résultats précis de simulation.

## ABSTRACT

Metal injection molding (MIM) is a new promising fabrication process in the aeronautical field. The MIM process can reduce part cost due to the lower number of secondary operations and can produce parts with high mechanical properties. Pratt & Whitney Canada is currently developing this process for manufacturing aircraft engine parts.

The process is divided in multiple steps. During one of these steps, the geometry is created by injecting feedstock into a mold cavity. The feedstock is made from a mixture of metal powders and a polymeric binder. This step is critical for the final part quality; it must be well controlled. Numerical simulation of the injection would be a beneficial tool in order to have a better understanding of this critical step. The goal of this work is to find and validate a numerical tool capable of simulating the injection step of P&WC's MIM process.

Properties of the feedstock were measured experimentally. Experimental data needed for the validation was acquired during several injection cycles with an instrumented mold and a high speed camera. The numerical simulation were calculated with Plasview3D using the experimental feedstock properties. Results showed that the numerical simulation underestimates the filling time. However, the calculated pressure profiles are similar to the ones acquired with the instrumented mold. A sensitivity study identified the viscosity level as a potential explanation for the observed discrepancies. It was found that the numerical simulation correlation for two different molds is improved by increasing the viscosity level by a factor of 2.5 for the complete shear rate range of the model. The inlet boundary condition was also studied and a solution was suggested to increase result accuracy.

In conclusion, P&WC's MIM process can be simulated numerically with Plasview3D. However, additional feedstock characterisation work (especially for the viscosity) is needed in order to have precise numerical results.

## TABLE OF CONTENTS

ACKNOWLEDGEMENT .....	III
RÉSUMÉ .....	IV
ABSTRACT.....	V
TABLE OF CONTENTS.....	VI
LIST OF TABLES .....	IX
LIST OF FIGURES.....	X
ACRONYMS AND SYMBOLS .....	XII
LIST OF APPENDICES.....	XIV
INTRODUCTION.....	1
CHAPTER 1. METAL INJECTION MOLDING .....	2
1.1 Process details.....	2
1.1.1 Mixing.....	2
1.1.2 Injection.....	3
1.1.3 Debinding.....	4
1.1.4 Sintering.....	5
1.2 Reasons to choose MIM .....	5
CHAPTER 2. LITERATURE REVIEW .....	7
2.1 Simulation.....	7
2.1.1 CFD background.....	7
2.1.2 Results of previous studies .....	9
2.1.3 Software selection.....	17
2.2 Material characterization.....	19
2.2.1 Viscosity.....	19
2.2.2 PVT.....	24
2.2.3 Specific heat.....	25
2.2.4 Thermal conductivity.....	26
2.2.5 Density .....	27
2.2.6 Solid loading.....	27
2.3 Experimental validation.....	28

2.3.1	Short-shots .....	28
2.3.2	Instrumented mold .....	29
2.3.3	High speed camera.....	31
2.3.4	Tomography .....	32
CHAPTER 3. METHODOLOGY .....		33
3.1	Process experimentation .....	33
3.1.1	Feedstock.....	33
3.1.2	Injection press .....	33
3.1.3	In-cavity measurement.....	33
3.1.4	High speed camera.....	38
3.2	Feedstock Characterization .....	42
3.2.1	Viscosity.....	42
3.2.2	Pressure Volume Temperature (PVT).....	46
3.2.3	Specific heat .....	46
3.2.4	Thermal conductivity.....	47
3.2.5	Density .....	47
3.3	Numerical simulation .....	48
3.3.1	Hardware .....	48
3.3.2	Mesh .....	48
3.3.3	Nondimensionalization.....	49
3.3.4	Pre-processor.....	51
3.3.5	CFD software .....	52
3.3.6	Post-processing.....	52
3.3.7	Numerical plan .....	53
CHAPTER 4. RESULTS AND ANALYSIS .....		54
4.1	PF505171 mold.....	54
4.1.1	In-cavity measurement.....	54
4.1.2	Characterization.....	58
4.1.3	Simulation results .....	63
4.1.4	Summary .....	81
4.2	PF65612 mold.....	82

4.2.1	High speed camera and simulation results .....	82
4.2.2	Summary .....	87
CHAPTER 5. DISCUSSION .....		88
5.1	Viscosity model .....	89
5.1.1	Results summary .....	89
5.1.2	Literature .....	90
5.1.3	Improvements suggestions .....	93
5.2	Inlet condition.....	94
5.2.1	Results summary .....	94
5.2.2	Literature .....	96
5.2.3	Improvements suggestions .....	96
5.3	Heat transfer.....	98
5.3.1	Results summary .....	98
5.3.2	Literature .....	99
5.3.3	Improvements suggestions .....	101
5.4	Characterization models .....	102
5.4.1	Results summary .....	102
5.4.2	Improvements suggestions .....	102
5.5	Mesh.....	104
5.5.1	Results summary .....	104
5.5.2	Improvements suggestions.....	104
5.6	Final thoughts .....	106
CONCLUSION .....		108
REFERENCES .....		111
APPENDICES.....		115

## LIST OF TABLES

Table 2.1 Software summary from literature review .....	18
Table 3.1 Calibration values and linear coefficient for cavity transducers. ....	34
Table 3.2 Experimental plan for in-cavity acquisition.....	38
Table 3.3 Experimental plan for high speed camera.....	42
Table 3.4 Cannon certified viscosity reference standard list.....	44
Table 3.5 Dimensionless parameter relations for simulation.....	52
Table 4.1 Experimental results for in-cavity measurements.....	58
Table 4.2 First simulation parameters. ....	64
Table 4.3 Results of the numerical sensitivity study.....	66
Table 4.4 Simulation results with old and new $\eta_0(T)$ temperature models. ....	75
Table 4.5 PF65612 mold simulation parameters. ....	82

## LIST OF FIGURES

Figure 1.1 Powder fabrication by gas atomization [2].	3
Figure 1.2 Particle size distribution.	3
Figure 2.1 Bilovol <i>et al.</i> simulated filing patterns compared to experimental result [16].	12
Figure 2.2 Thomas <i>et al</i> [26]: Simulation on top row and short-shots at the bottom row.	15
Figure 2.3 Fluid between parallel plates (adapted from Green and Perry [38]).	19
Figure 2.4 Fluid types.	21
Figure 2.5 Capillary (left) and rotational (right) rheometers from [40].	22
Figure 2.6 PVT results (points) with Tait model (lines) from [45].	25
Figure 2.7 Cooling rate effect on mean specific heat for a 316L feedstock [47].	26
Figure 2.8 Short-shots comparison with simulation [45].	29
Figure 2.9 Cavity with pressure sensors positions studied in [3].	30
Figure 2.10 Typical pressures curves in plastic injection molding [3].	31
Figure 2.11 High speed camera result, nearside (b) and backside(a) flow front [51].	32
Figure 2.12 Numerical velocity and flow lines compared to micro tomography [26].	32
Figure 3.1 PF505171: Assembled and exploded view with positioning of sensors.	34
Figure 3.2 Data acquisition system with wiring.	36
Figure 3.3 Data before (left) and after (right) conditioning.	37
Figure 3.4 PF65612: Assembled and exploded view.	39
Figure 3.5 High speed camera system.	41
Figure 3.6 Virtual filled level on the mold front view (displayed in blue, units: inches).	41
Figure 3.7 Traction bar meshed with tetrahedral element with boundary conditions.	49
Figure 4.1 Experimental repeatability test with PF505171 mold.	55
Figure 4.2 Effect of the initial mold temperature on the filling time.	56
Figure 4.3 Experimental data at $P_1$ psi, $0.8 \cdot T_g$ mold temp and $1.7 \cdot T_g$ melt temperature.	57
Figure 4.4 Experimental data and fitted viscosity model (AR-2000).	59
Figure 4.5 Experimental PVT and density measurement.	60
Figure 4.6 Experimental specific heat measurements.	61
Figure 4.7 Experimental thermal diffusivity measurements.	63
Figure 4.8 First simulation results compared with experiments.	64

Figure 4.9 Relative viscosity error with calibrated fluid for AR-2000 at $1.5 \cdot T_g$ .....	68
Figure 4.10 Experimental data and fitted viscosity model for the 2 <sup>nd</sup> rheometer (CVO).....	69
Figure 4.11 Simulation final time step result with CVO-50 viscosity model. ....	70
Figure 4.12 Experimental data at $1.5 \cdot T_g$ for the third rheometer (SR-200).....	71
Figure 4.13 Temperature models used in the viscosity equation for both rheometers. ....	72
Figure 4.14 New temperature models for $\eta_0(T)$ .....	73
Figure 4.15 Simulation results with AR-2000 viscosity model scaled by 2.5.....	76
Figure 4.16 Time-dependent inlet pressure model, $p(t)$ . ....	77
Figure 4.17 Time-dependent filled volume relation, $fvf(t)$ . ....	79
Figure 4.18 Inlet pressure model, $p(fvf)$ . ....	79
Figure 4.19 Simulation results with a variable inlet pressure condition. ....	80
Figure 4.20 Experimental and numerical results comparison, time synchronized. ....	84
Figure 4.21 Experimental and numerical results comparison, position synchronized. ....	85
Figure 4.22 Melt front shape comparison at the beginning off the filling.....	86
Figure 4.23 Melt front position as a function of time.....	87
Figure 5.1 Wall slip and yield stress effect (adapted from Ahn <i>et al.</i> [19]). ....	91
Figure 5.2 Herschel-Bulkley effect on shear rate and velocity profiles (Thornagel [53]). ....	92
Figure 5.3 Integral of the inlet pressure boundary condition as a function of time.....	95
Figure 5.4 Pressure variation on the inlet surface at various time steps.....	96
Figure 5.5 Normalized temperature distribution at the middle plane.....	99
Figure 5.6 Simulation mesh including all geometric features for the PF505171 mold.....	105
Figure 5.7 Refined and simplified mesh with boundary layers for the PF505171 mold.....	105

## ACRONYMS AND SYMBOLS

### ACRONYMS:

CFD	Computational fluid dynamics
FDM	Finite difference method
FEM	Finite element method
FVM	Finite volume method
LDPE	Low density polyethylene
MIM	Metal injection molding
NRC-IMI	National Research Council Canada-Industrial Materials Institute
P&WC	Pratt & Whitney Canada
PIM	Powder injection molding
PSD	Particle size distribution
PVT	Pressure, volume and temperature relation
UDF	User defined function

### SYMBOLS:

$\alpha$	Diffusivity
$\beta$	Compressibility factor
$\phi$	Solid loading
$\dot{\gamma}$	Shear rate
$\eta$	Viscosity
$\eta_0$	Viscosity at low shear rate
$\eta_\infty$	Viscosity at high shear rate
$\mu$	Viscosity
$\nu$	Specific volume
$\rho$	Density
$\sigma$	Standard deviation
$\tau$	Viscous stress tensor

$\nabla$	Vector differential operator
$A$	Area
$C_p$	Specific heat at constant pressure
$D/Dt$	Total derivative
$F$	Force
$f_v$	Filled volume fraction
$\mathbf{g}$	Gravity vector
$h$	Height
$k$	Thermal conductivity
$P_I$	Standard injection pressure for PF505171 mold
$P_T$	Standard injection pressure for PF65612 mold
$p$	Pressure
$Q$	Flow rate
$S$	Residual sum of squares
$T$	Temperature
$T_g$	Glass transition temperature
$T_{trans}$	Transition temperature for Tait PVT model
$t$	Time
$\mathbf{U}$	Velocity vector
$V$	Volume
$X$	Scale factor

## **LIST OF APPENDICES**

APPENDIX 1 – MOVING AVERAGE C# PROGRAM .....	115
APPENDIX 2 – AR-2000 COMPLETE SETTINGS .....	118
APPENDIX 3 – DETAILED SUMMARY OF THE SIMULATIONS .....	122

## INTRODUCTION

The Metal Injection Molding (MIM) process is a cost efficient manufacturing technology that is not completely understood. Several companies are investing in the development of this new technology to enlarge manufacturing capability and reduce costs. Even in the aeronautical field, this new technology is growing. The aircraft engine manufacturer Pratt & Whitney Canada (P&WC) is working on new superalloy parts made by MIM.

P&WC's MIM process is currently in development and some issues still need to be studied. For instance, the production rate is not as high as expected. Rejected parts are frequently produced during the injection step and only detected after sintering. Moreover, mold design relies on experience and iterative steps which can be very expensive. In order to have a better understanding of key factors during the injection step and shorter mold design lead time, computer simulation of part injection would be helpful.

The purpose of this work is to find software that could simulate the injection phase of P&WC's MIM process and then validate the results with experimental data. If results are satisfactory, the simulation will be used to design new molds and improve problematic molds. If possible, it should also predict the powder segregation caused during filling and therefore non-uniform shrinkage during sintering.

This work is divided in five chapters. The first chapter gives an overview of what exactly is the MIM process with basic terminology. In addition, each steps of the MIM process are explained briefly. The second chapter is a literature review about simulation methods, feedstock characterization and experimental data acquisition. Next, chapter three gives the methodology for the same topics found in literature review but in a different order: feedstock characterization, experimental data acquisition and simulation. Parameters and methods needed to replicate the current work are presented in that chapter. It is followed by chapter four in which results are presented and explained. This chapter is divided into two sub-chapters, one for each mold used in this work: the instrumented rectangular bar mold PF505171 and the traction bar mold PF65612. The sixth and final chapter is a discussion about the presented work. Improvement suggestions are given in that chapter. Finally, this work ends with a conclusion.

## CHAPTER 1. METAL INJECTION MOLDING

Powder metallurgy is an established manufacturing technology. One of the oldest variants is the pressing process, where powders are shaped and compacted in a die then sintered. Since the process is limited in term of geometrical complexity (uniaxial compaction), new processes have emerged to overcome shaping problems. Powder injection molding (PIM) is one of them. This technology uses polymeric binders mixed with powders to obtain a low viscosity suspension that can be injected when heated. This process allows the use of a wide range of materials like ceramic, superalloy, steel, etc. When using metallic powders, the acronym for the process becomes MIM, standing for Metal Injection Molding.

The MIM process has been used for numerous commercial parts; medical tools, heat sinks, triggers, watch cases, implants, hard drive magnet, aircraft engine part and others [1]. Generally, the limitation for this process is the maximum dimension of the part, the requested tolerances and the annual production rates. In other words, if the part has a small size, a complex geometry, realistic tolerances (about 0.5% of the dimension [1]) and a large production volume, MIM is profitable in term of price per unit.

### 1.1 Process details

The MIM process is divided in four steps: mixing, injection, debinding and sintering. Many variances exist between producers, but the following is a general review of what is involved in each step.

#### 1.1.1 Mixing

The first step is the combination of raw materials (binders and powder) in a rotational mixer. The mixture of polymeric binders and powder is called a feedstock. For a low viscosity feedstock, spherical powders are preferred to irregular ones. Carbonyl decomposition, plasma atomization, centrifugal atomization and gas atomization are all fabrication methods which produce rounded powders with different typical diameter. For example, the gas atomization method uses the gas velocity to break alloy melt in small droplets (see Figure 1.1). Due to the Rayleigh instability [2], spheroidization occurs during

the flight before solidification. Many parameters influence the final result, including melt viscosity, melt temperature, gas velocity and the diameter of the melt exit.

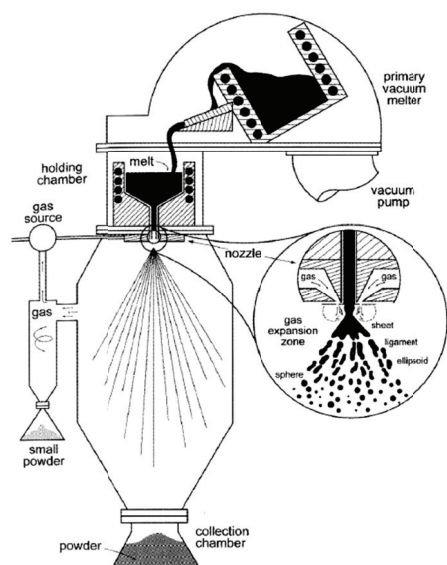


Figure 1.1 Powder fabrication by gas atomization [2].

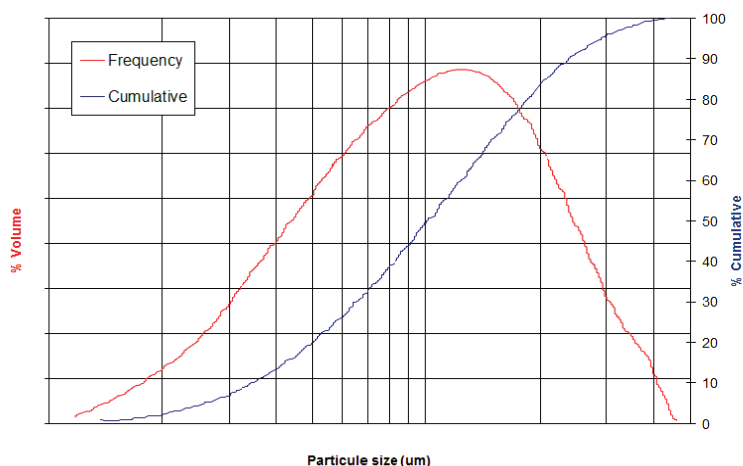


Figure 1.2 Particle size distribution.

The result of gas atomization is generally close to a log-normal distribution (see Figure 1.2). The particle size distribution (PSD), often measured by light scattering, is a key factor for MIM. It defines among others the feedstock viscosity, the maximum solid loading and the sintering behavior. Mixed with powder, the binders have multiple purposes: transport of the powder, strengthen the green part and preserve geometry. The binders are chosen according to the debinding technique and injection parameters.

Generally, the volume fraction of powder is about 60%. This fraction, called solid loading, is a major parameter for the MIM process. It controls the shrink factor, thus the final part dimensions. The more binder is added, greater is the final shrinkage. Considering this phenomenon, feedstock homogeneity is critical during the mixing step to avoid defects in subsequent steps.

### 1.1.2 Injection

The second step is the injection, or molding, which creates the part geometry. The process starts by increasing the feedstock temperature to exceed the melting temperature of the

binder, then a press forces feedstock into the mold cavity. The entrance point, called gate, is sheared and the mold is opened to extract a green part.

The type of viscosity for the feedstock is shear thinning (the viscosity decreases with an increase of the shear rate) which reduces the required pressure during the filling. The viscosity also depends on the temperature and the solid loading of the feedstock. Molds are made of tool steel and are based on a scaled geometry of the final part. The scale factor ( $X$ ) is related to the green and sintered density by equation (1.1):

$$X = \rho_{Sintered}^{(1/3)} \cdot \rho_{Green}^{(-1/3)} \quad (1.1)$$

This relation reveals a critical fact: for a fixed final density, a variation of the green density causes a dimensional variation. Hence, like for the mixing step, gradients of density need to be minimized. The fabrication of molds can be simple but the addition of features like vents, cooling/heating channels, ejector pins, thermocouples and others complicate their design.

Depending on operation parameters, many issues can occur during injection (voids, jetting, short-shot, flashing, segregation...). Since the injection is an early step in MIM and because some of these issues are only revealed after sintering, avoiding them is important.

### 1.1.3 Debinding

The third step is debinding. The purpose of this step is to remove the binder and to produce initial densification in order to provide some strength to the parts to facilitate handling. Three methods are frequently used: thermal decomposition, wicking and solvent extraction.

Wicking for instance, extracts the liquid binder by capillary action at high temperature. This is done by embedding the part in a bed of powder which produces the capillary force. This bed preserves geometry and does not react with the part. The wicking action creates a flow from the middle of the part to the surface, so increasing the thickness of the part lengthens the debinding step. The remaining binder is thermally decomposed at higher temperature. Finally, a pre-sintering bonds particles together to give strength to the brown part.

### **1.1.4 Sintering**

The final step is sintering, where the part reaches its final density (>95% of full density). The part is placed on a setter in a furnace and exposed to a reducing or inert atmosphere. The temperature rises just under the melting point of the material following a specific profile.

The sintering cycle is similar to any conventional sintering. The reduction of surface energy is the main driving force for sintering. As a result, parts made of small particles need less energy to densify. Many transport and diffusion mechanisms could be involved during sintering: viscous flow, plastic flow, evaporation-condensation, volume diffusion, grain boundary diffusion and surface diffusion [3].

## **1.2 Reasons to choose MIM**

There are numerous reasons to choose this fabrication process, examples are given below:

First, the process can manufacture parts out of materials with low machinability since complex geometric features can be directly molded with a good dimensional tolerance without machining. Furthermore, new geometric feature, that were usually challenging to manufacture with conventional techniques, can be made with MIM and produce new part concepts.

Second, MIM has a high production rates capability that can reduce lead time for part production once the mold is manufactured and the process parameters are fine-tuned.

Third, this process can reduce part cost thanks to the lower number of secondary operations and the high production rate stated previously.

Fourth, parts produced by MIM have higher mechanical properties and better tolerances than casting because the shrinkage is more predictable in powder injection molding and the resulting pore size is much smaller than that observed in cast parts.

Finally, less material is wasted with MIM as the process produces the final part shape with no or little machining. In addition, defective green parts can be recycled by adding them to the feedstock.

## CHAPTER 2. LITERATURE REVIEW

The next chapter will look at recent studies and give the necessary theoretical knowledge needed for the simulation of MIM. This chapter is divided in three parts. First, a review of the available software will be presented and evaluated. From this review, a software selection will be made for the current project. The second part will present various methods used to obtain the needed parameters for fluid characterization or modeling. Finally, the last part will review different experimental validation techniques.

### 2.1 Simulation

The simulation of MIM is quite complex; a non-isothermal three-dimensional flow of a shear-thinning two-phase fluid flow. This complexity combined with a younger industry, explains the only recent availability for MIM 3D simulation. Early developments were made with plastic injection molding software adapted to MIM's particularities. Now, many software applications are sold specifically for MIM simulation.

To understand the key differences between software, a brief summary about computational fluid dynamics (CFD) will follow.

#### 2.1.1 CFD background

CFD is a numerical methodology used in a wide range of domains to solve fluid flow problems. This method divides the fluid domain into cells to create a mesh. Then boundary conditions are imposed and the modeling equations are solved. The velocity vector, the pressure and the temperature at each time step are the solution output. Equations modeling the flow are defined in the next sub-section followed by a presentation of different discretization methods to solve them.

##### 2.1.1.1 Governing equations

Commonly, Navier-Stokes equations [4] are chosen to represent the conservation of momentum for fluids:

$$\rho \frac{\partial \mathbf{U}}{\partial t} + \rho (\mathbf{U} \cdot \nabla) \mathbf{U} = -\nabla p + \mu \nabla \cdot (\nabla \mathbf{U} + \nabla \mathbf{U}^T) + \rho \mathbf{g} \quad (2.1)$$

Where:

$$\begin{aligned}
 \rho &= \text{Density} \\
 \mathbf{U} &= \text{Velocity vector} \\
 t &= \text{Time} \\
 p &= \text{Pressure} \\
 \mu &= \text{Viscosity} \\
 \mathbf{g} &= \text{Gravity vector} \\
 \nabla &= \text{Vector differential operator}
 \end{aligned}$$

The mass conservation must also be respected:

$$\frac{D\rho}{Dt} + \rho(\nabla \cdot \mathbf{U}) = 0 \quad (2.2)$$

In the case of an incompressible flow, it simplifies to the continuity equation:

$$\nabla \cdot \mathbf{U} = 0 \quad (2.3)$$

Finally, in the case of non-isothermal flow, the energy equation combined with Fourier's law is used for temperature variation:

$$\rho C_p \left( \frac{\partial T}{\partial t} + (\mathbf{U} \cdot \nabla) T \right) = \nabla \cdot (k \nabla T) - (\boldsymbol{\tau} : \nabla \mathbf{U}) \quad (2.4)$$

Where the new variables are:

$$\begin{aligned}
 C_p &= \text{Specific heat} \\
 T &= \text{Temperature} \\
 k &= \text{Thermal conductivity} \\
 \boldsymbol{\tau} &= \text{Viscous stress tensor} \\
 D/Dt &= \text{Total derivative}
 \end{aligned}$$

### 2.1.1.2 Discretization methods

Various discretization methods are employed for resolving these equations on the studied domain. Finite Difference Method (FDM), Finite Element Method (FEM) and Finite Volume Method (FVM) are the most common methods.

The FDM is based on Taylor series to approximate the derivatives. This method usually requires a structured grid and when it is used for complex shapes, the meshing may be problematic [5]. But with an appropriate type of grid, this method is very efficient. The FEM

is mathematically more rigorous. The partial differential equations (PDE) are multiplied by a test function and integrated on the domain to obtain the variational form (including integration by part to decrease the differential order). Unlike the FDM, FEM can be easily applied to complex shapes since it intrinsically uses an unstructured grid. This method may require stabilization terms when solving the Navier-Stokes equations. A more detailed explanation on the method can be found in Fortin's book [6]. The FVM also permits to solve complex shapes. This method is based on the balance of surface fluxes between neighbouring control volumes. An integral form of the PDE is used with the divergence theorem on each volume. This method is employed in commercial aerodynamics programs such as Fluent, but is rarely used in filling simulation.

Other methods exist, and special combinations are possible. For example, the two dimensional formulation of the FEM can be combined with the FDM to simulate three dimensional flow in thin-walled geometries. This method is often called a 2.5D method and uses the Hele-Shaw flow assumption [7]. This is an approximation that reduces the computer resources needed by neglecting some effects in the thickness direction.

Most of these methods have been used for a long time. Which of them is the most appropriate depends on the problem characteristics.

## **2.1.2 Results of previous studies**

The following section is a review of MIM simulation papers with description of their results or capabilities. Efforts were made to make this review comprehensive enough to guide the choice of software for this project. It is obvious that some of them have not been reviewed since they are often in-house codes not released yet. Results are sorted by software; nine of them are presented in alphabetic order.

### **2.1.2.1 ANSYS**

The first mention of ANSYS for MIM simulation is found in a paper written by Zheng and Qu. in 2006 [8]. Their results are given by "finite element analysis software ANSYS", without further details. Their numerical results showed a region where the feedstock temperature

was higher than the initial inlet temperature. They attributed this phenomenon to viscous heating. They also predicted areas of possible weld line in the mold. However, no experimental data validates their results. Their analysis is also limited to a two dimensional problem.

Samanta *et al.* studied the influence of multiphase versus single phase model in a simple 3D geometry [9]. In their case, user defined functions (UDF) were used in Fluent with the SIMPLE algorithm (FVM) to simulate PIM. Their results with the multiphase model showed that a higher binder concentration at the mold cavity surface reduced heat transfer compared to the single phase model, even if the calculated solid loading variation was very small (<0.03%). Again, no experimental data was presented to validate this study. In addition, the feedstock used had a 37% solid loading which is lower than typical MIM feedstock (~60% [1]).

Lately, Yin *et al.* used another product of ANSYS to simulate micro MIM; ANSYS CFX [10]. They related different defects found in miniature gears to the position of the gate and numerical velocity field.

#### **2.1.2.2 Moldex3D**

In 2009, Jenni and Wilfinger published a paper about the simulation of MIM by implementing a powder-binder add-on for Mouldex3D<sup>1</sup> [11]. Unfortunately, their work was not successful since the add-on was never used with Moldex3D, only in Matlab. However, the authors proposed an efficient way for experimental determination of segregation in a MIM part by differential scanning calorimetry (DSC).

Another study by Andrews *et al.* in 2010 used Moldex3D for micro MIM [12]. Different gate locations on two different three-dimensional geometries were tested to minimize the shear stress. Some errors were found in their results (temperature discontinuities) but were corrected by a later release of Moldex3D. Once again no experimental data supported their numerical predictions.

---

<sup>1</sup> Mouldex3D will be interpreted as Moldex3D since the notation with the letter “u” was not found in any other paper nor on a commercial website.

### 2.1.2.3 MoldFlow

The earliest mention of MoldFlow for the simulation of MIM found in the literature is the 1997 review on new development in MIM [13]. Petzoldt *et al.* reported the ability of MoldFlow to detect weld lines. Some results for temperature distribution and filling patterns are given without much detail.

A very relevant paper by Bilovol *et al.* compares MoldFlow to ProCAST and C-Mold (which doesn't exist anymore, bought by MoldFlow in 2000[14]). They used an instrumented mold (pressure and temperature) to verify the simulations from these software. First they compared the flow pattern of the simulations with a short-shot (see-section 2.3.1 for definition); the result is shown in Figure 2.1. MoldFlow calculations were in good agreement with experimentation for short-shot and weld line prediction. Next, the authors studied the temperature and pressure evolution at specific locations. One observed drawback of MoldFlow was the lack of plotting capability for temperature or pressure. An important experimental observation was made; the feedstock temperature rises after its passage through the gate, viscous heating was suggested to explain this phenomenon. According to the authors, MoldFlow produced good temperature prediction. As for the pressure prediction, results were found to be at least three times lower than the measured pressures. This was the worst result of all the tested software. In conclusion, the authors recommended ProCAST for MIM simulation.

Zheng *et al.* also used pressure sensors to verify MoldFlow simulation [15]. Unlike the previous study, their results were in good agreement with experimental pressure using the Hele-Shaw flow assumption and a second order model to fit the viscosity. Based on their simulation, the authors redesigned the gate in the model and adjusted parameters to obtain a suitable part after injection.

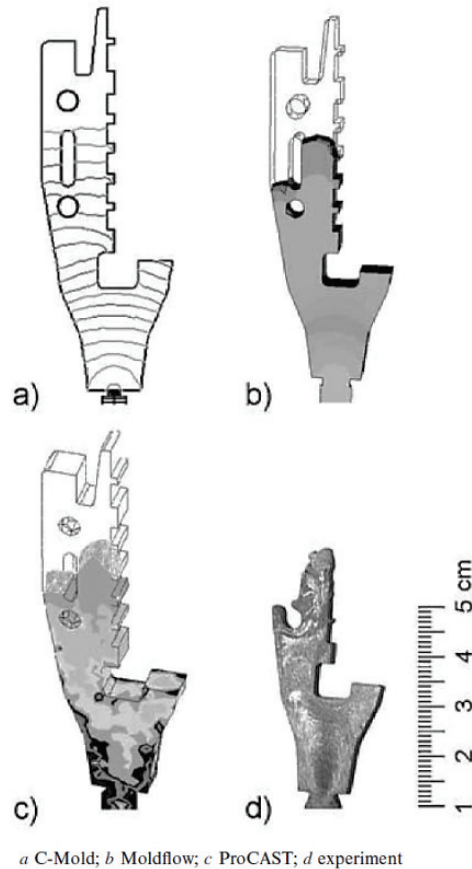


Figure 2.1 Bilovol *et al.* simulated filing patterns compared to experimental result [16].

#### 2.1.2.4 PIMSolver

Cetatech's PIMSolver is a commercial software made for MIM. Its discretization method is a combination of FEM and FDM in the thickness direction. The governing equations are simplified by the Hele-Shaw assumption for thin parts; therefore it is a 2.5 dimensional simulation. A slip model can be added in the solver. Atre *et al.* used PIMSolver to study the effect of input parameters during filling [17]. With a traction bar and plate geometry, they varied the inputs; process parameters, cavity shape, feedstock and binder rheology. Simulation of each case was then made and predefined key outputs of the final part were recorded. They defined the sensitivity as the percentage of change in the output by the percentage of change in the input. The sensitivity was then sorted by qualitative levels. A very useful table is given for the correlation between input and outputs with corresponding level of sensitivity.

Urval *et al.* presented another study based on PIMSolver for optimization of micro MIM parts [18]. They studied the impact of the thickness on different factors: the maximum pressure, the temperature distribution and the maximum shear rate. Compared to experimental results, PIMSolver slightly over-estimated the filling profile (filled volume versus time). The authors suggested that the location of their pressure transducer used for experimental acquisition might be a cause of discrepancy since it was not close enough to the pressure application point. The lack of slip layer and slip velocity model for the feedstock is another cause of discrepancy mentioned by the authors.

In 2008 Ahn *et al.* compared experimental and numerical pressures to verify the effects of slip layer and temperature boundary conditions [19]. They found that numerical pressure was in better agreement with experimental results when a slip layer and integrated cooling were considered. This slip layer acted as an insulator and reduced the heat transfer, therefore the temperatures were higher. Later, the same authors wrote an additional paper about these results but gave a list of possible optimisation of MIM possible with PIMSolver [20]. For example, they suggest minimizing the pressure to choose a suitable filling time.

In conclusion, even if all these publications showed that PIMSolver can accurately simulate the injection of MIM parts, it is essential to remember that this software is limited to thin-walled shapes.

#### **2.1.2.5 Plasview3D**

Plasview3D is the in-house program for mold filling simulation at the National Research Council-Industrial Materials Institute (NRC-IMI). This software is a three-dimensional parallel solver for fluid flow that uses FEM. The code was originally written for 3D plastic injection molding, but has since been used for MIM. A paper by Ilinca *et al.* in 2002 reported the successful use of Plasview3D for a rectangular MIM part [21]. Two pressure sensors were used inside the cavity to obtain experimental measurements that were compared to the numerically predicted pressure at corresponding locations. During the filling stage, the simulation showed good agreement with these two pressure histories. For the packing stage, predicted pressure curves were closer to experimental ones when the tool deformation was taken into account. The same year, Ilinca *et al.* presented new results for a

more complex “M” part [22]. The predicted flow pattern was favourably compared with the short-shots and behaviors like folding were observed in the simulation. In addition, their results correctly predicted the asymmetrical filling of the cavity. This instability was explained by the high temperature dependence of the viscosity which amplified a slight inlet velocity delta. They showed that improvement could be made by enlarging the gate thickness. It should be noted that the authors found better agreement with experimentation when the inertia was considered with a no slip condition.

Plasview3D has a segregation capability (solid loading variations within the feedstock); Ilinca and Hétu published their results in 2008 [23]. They used the diffusive flux model proposed by Phillips *et al.* [24] for segregation and a modified Krieger-Dougherty model for solid loading dependence of the viscosity. Couette flow, piston-driven flow and sudden contraction-expansion flow were simulated and compared with experimental data for model validation. The calculated solid loading profiles were similar to experiments. However, two methodological aspects in this paper are different from P&WC’s MIM process; the liquid and solid phases do not have the same density and the mean particle size is much lower than the smallest particle size used in this study. Consequently, a validation of those models with P&WC’s feedstock would be needed. The same results are presented more briefly in a conference paper [25].

At the same conference, Thomas *et al.* also presented a study with Plasview3D [26]. The cause of a recurrent defect was identified by studying the filling behavior with the numerical simulation. The software permitted to predict the jetting (irregular filling patterns) in a dental implant as shown in Figure 2.2. Furthermore, with micro tomography and the calculated flow lines, the authors observed that a binder-rich layer was formed at the gate and then followed the flow path.

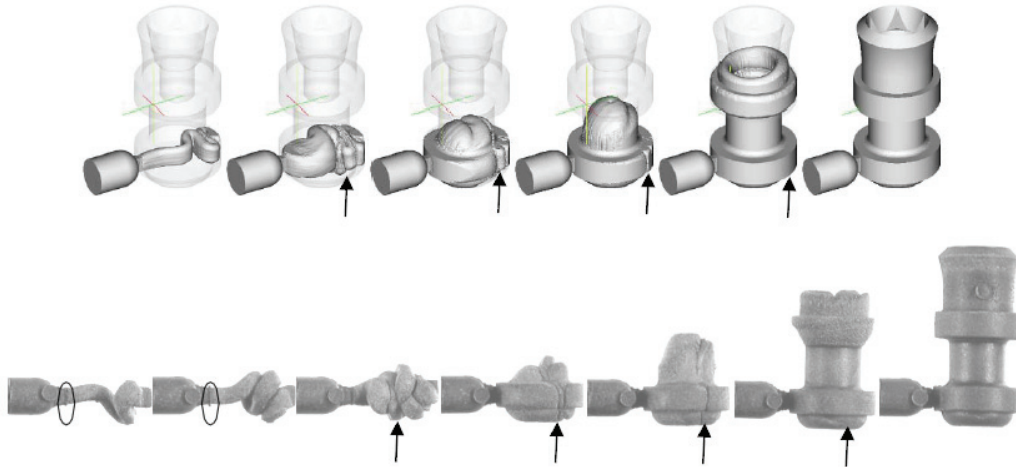


Figure 2.2 Thomas *et al* [26]: Simulation on top row and short-shots at the bottom row.

### 2.1.2.6 Pohang University

No name has been found in literature for this non-commercial software developed by Kwon *et al.* from Pohang University of Science and Technology. In 1995, Kwon and Park [27] wrote an article about the yield stress and slip phenomena giving the methodology description of their numerical code. Their code is based on a combination of FEM and FDM with the Hele-Shaw assumption, hence a 2.5D program. They also added slip layer and slip velocity models to their software. Using a modified Cross model to account for the yield stress, they numerically studied the effect of the viscosity with or without yield, the slip layer thickness and the slip velocity on isothermal and non-isothermal flow of PIM. They concluded that the slip layer model and yield stress model should be considered for non-isothermal flow since the slip layer thickness affects the heat transfer. A case study on a PIM turbine rotor is also presented with the effect of adding a gate on temperature and pressure without experimental comparison.

In 2002, Hwang and Kwon performed full three-dimensional simulation by solving the Stokes equation (inertial forces neglected) with FEM [28]. A method called “volume fill factor” was used in conjunction with a smoothing scheme to track the flow front during filling. They predicted the flow front profile shape and position in a tool insert mold with a feedstock and a polymer. The goal was to simulate and experimentally validate two types of fluid behavior; one with slip (feedstock) and the other without (LDPE). They showed that

the velocity profile and the filling pattern were affected by the slip condition. Their simulations were compared with short-shots but the mesh used was too coarse to precisely define the velocity profiles.

#### **2.1.2.7 ProCAST**

The previously described paper of Bilovol *et al.* compared ProCAST to two other software programs for MIM [16]. They concluded that ProCAST was the most suitable for MIM. Indeed, ProCAST predicted well the filling patterns and the weld line location. Still, the calculated cavity pressures and temperatures did not match the experimental data.

The same authors studied different viscosity models with ProCAST [29]. Only the experimental pressure data was used for comparative evaluation of the viscosity models. An erratic numerical pressure curve was obtained when the viscosity model had a high viscosity at very low shear rate.

P&WC evaluated ProCAST for its MIM process in 2007 [30, 31]. The filling of a traction bar was simulated with estimated feedstock characteristics as a first attempt. A Newtonian viscosity model with temperature dependence and a pressure-dependent heat transfer coefficient (between 4000 and 10000 W/m<sup>2</sup>·K) were used. Length of non-filled part was compared with ProCAST calculated length. The numerical results were not exact and the need for a better viscosity model and mold temperature control was mentioned.

#### **2.1.2.8 Sigmasoft**

Only one article was found reporting MIM simulation with Sigmasoft [32]. Thornagel reported the simulation of a watch strap. By trial and errors, some ribs were added to the mold to eliminate a segregation defect called “black lines”. With particle tracers, the author explained the effect of the ribs as traps for the binder-rich layer near the wall. No details about Sigmasoft nor about the simulation are given by the author.

#### **2.1.2.9 FEAPIM (UMR CNRS)**

The last software of this literature review is a non-commercial code from the university of Franche-Comté and *Centre national de la recherche Scientifique* (CNRS), France. Using FEM

for solving the Stokes equations on a three-dimensional domain, this software employs a multiphase (mixture theory) approach to simulate the injection of MIM. Consequently, two sets of momentum, continuity and energy equations are solved in addition to a momentum exchange term for interactions between phases. The benefit is that this approach allows direct prediction of segregation in the molded parts. Gelin *et al.*, reported successful simulation of a multi component mold with their software [33]. Short-shots were made to validate the simulation. The flow front position was in good agreement with experimentation in a complex cavity. Two segregation mappings were presented, but no experimental data allowed them to confirm their result. Taking a closer look at the calculated flow front profiles, some irregularities can be observed (the flow front seems to oscillate rather than present a parabolic profile). No comments are made to explain the shape of the flow front.

Another paper by Gelin *et al.* presented more numerical results for the same mold and for a divergent-convergent mold [34]. A solid loading variation of 3% was observed in the simulation of the later mold. The flow front position was the only verified data even if they had an instrumented mold with pressure and temperature sensors. Methodological aspects for the viscosity model for the two phases are not described by the authors. Similar papers give a brief summary of these simulation results with the same mold [35, 36].

A recent paper provided more details on solid loading distribution on a wheel geometry. Gelin *et al.* [37] used FEAPIM to simulate the green density variation as an input for sintering simulation. They compared the experimental tensile strength of a traction bar to the numerically simulated one at different temperatures. They obtained a good overall tendency. The main drawback for this software is the need for solid phase viscosity data, which is not simple since viscosity measurements are usually done with fluids.

### **2.1.3 Software selection**

In order to get a good overview of the available solutions for the simulation of P&WC's MIM process, a summary of all reviewed software with key characteristics is given below (Table

2.1). Associated papers are given in the last column, in addition to the nearest location from P&WC's plant 1 for each software programs based on available data.

Since all previous studies are founded on the conventional MIM process, there is no guarantee that they can successfully simulate P&WC's MIM process. For example, the boundary conditions are dissimilar; imposed inlet velocity for conventional molding versus imposed inlet pressure for the current work. Viscosity and pressure are also of a different order for this project. So, the flexibility of the software is of great importance: multiple boundary conditions should be implemented in the software and usage of custom viscosity models should be allowed. Furthermore, P&WC's typical parts are usually very complex, leading to a need for a true 3D simulation. Segregation capability is also of great interest since many dimensional variations and mechanical defects are linked to solid loading variations. In aeronautics, these deviations must be kept small to guarantee airworthiness while simultaneously allowing an acceptable production yield.

Table 2.1 Software summary from literature review.

Software	Domain	Method	Segregation study	Nearest Location	Commercialized	Articles
ANSYS (Fluent, CFX, other)	3D	FVM/FEM	no	Waterloo	yes	[8-10]
Moldex3D	3D	FVM	no	USA	yes	[11, 12]
MoldFlow	3D	FEM	no	Montreal	yes	[13, 15, 16]
PIMSolver	2.5D	FEM/FDM	no	S. Korea	yes	[17-20]
Plasview3D	3D	FEM	yes	Boucherville	no	[21-23, 25, 26]
Pohang University (T.H. Kwon <i>et al.</i> )	3D	FEM	no	Korea	no	[27, 28]
ProCAST	3D	FEM	no	USA	yes	[16, 29-31]
SigmaSoft	?	?	no	USA	yes	[32]
FEAPIM	3D	FEM	yes	France	no	[33-37]

After this literature review, the Plasview3D software was selected for this project for its proven full 3D and segregation capabilities. The fact that this software is not commercialized is not an issue. In fact this aspect gives much more flexibility to adapt the code for the specific needs of P&WC. Finally, the NRC-IMI allowed P&WC to use their high end computer equipment and provided assistance for code modifications. Hence, every numerical results of the current work will be calculated with the Plasview3D software.

## 2.2 Material characterization

All parameters in equations (2.1) and (2.4), the viscosity, density, specific heat and thermal conductivity, must be prescribed to simulate the flow adequately. In the case of MIM, the fluid is called a feedstock. For the characterization of the feedstock, these properties are obtained by various methods explained in the next section.

### 2.2.1 Viscosity

The first characteristic is the most difficult to obtain since the feedstock is a suspension and has special behaviors like shear thinning and thixotropy (segregation). Viscosity is dependent on shear rate, temperature, solid loading and pressure. Special care is needed to get representative experimental data; using samples only once, reducing the total time of tests and using a precise temperature controller just to name a few. Before presenting potential equations and methodology for modeling the feedstock viscosity, a short introduction on viscosity is given below.

#### 2.2.1.1 Basics

Viscosity is roughly the resistance of a fluid to flow. An easy example to describe this property is the parallel plates shown in Figure 2.3.

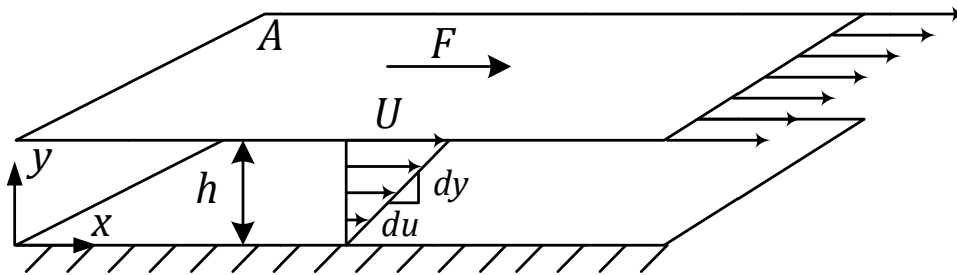


Figure 2.3 Fluid between parallel plates (adapted from Green and Perry [38]).

The bottom plate is fixed while a constant force  $F$  is applied on the top plate which moves at constant speed when a steady state is reached. Assuming that there is no slip at walls, the velocity profile is linear:  $u_y = U \cdot y/h$ . The shear stress  $\tau$  (in Pa) imposed is the ratio of the force  $F_x$  on the acting surface  $A$ :

$$\tau_{yx} = \frac{F_x}{A} \quad (2.5)$$

The shear rate is defined in this case as the velocity gradient in the  $y$  direction in reciprocal seconds:

$$\dot{\gamma} = \frac{du}{dy} = \frac{U}{h} \quad (2.6)$$

The relationship of shear stress and shear rate is expressed as:

$$\tau = \eta \cdot \dot{\gamma} \quad (2.7)$$

The viscosity  $\eta$  is expressed in Pa·s ( $\mu$  is also often used as a symbol). Fluids are generally separated in two categories, Newtonian and non-Newtonian. If the fluid's viscosity is not shear rate dependent, i.e. the shear stress increases linearly with the shear rate, the fluid belongs to the Newtonian category. Shear thinning, shear thickening, Bingham plastics are examples of non-Newtonian fluids. Figure 2.4 summarizes most fluid behaviors in a simple figure; the viscosity can be observed as the local slope. In general, viscosity curves are illustrated by the viscosity as a function of shear rate in logarithmic scales. The two upper curves exhibit a yield stress; the fluid needs a minimum stress prior to flow initiation. This behavior can be modeled with the Herschel-Bulkley model with Papanastasiou modification [22, 26].

Another fluid rheological characteristic is the time-dependence. If the viscosity of a fluid decreases when submitted to constant shear rate, the fluid is thixotropic. On the opposite, if its viscosity increases, it is a rheopectic fluid [39]. In MIM, the feedstock can be considered as a thixotropic fluid since the viscosity decreases with time due to particle deagglomeration or segregation.

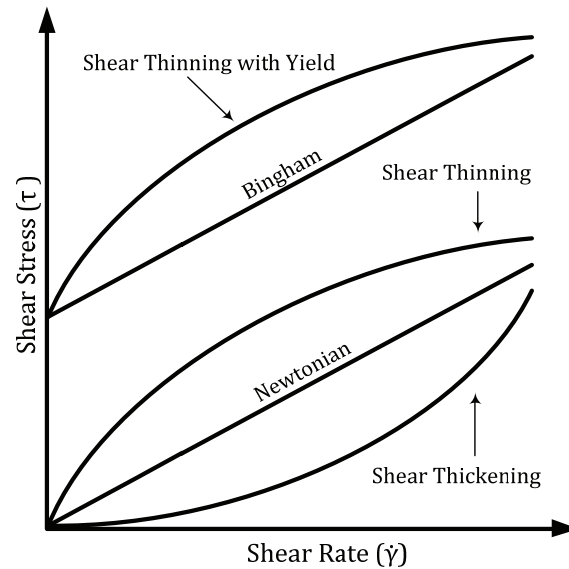


Figure 2.4 Fluid types.

### 2.2.1.2 Methods and Models

Two types of rheometers are generally used to obtain viscosity curves; capillary and rotational (Figure 2.5). The former uses pressure to force the fluid into small diameter die (Poiseuille flow). Knowing the flow rate ( $Q$ ) and the pressure drop, viscosity can be calculated with the Rabinowitch equation if the fluid is non-Newtonian [40]. This method can reach very high shear rates and is relatively simple. However low shear rates are difficult to obtain with this method. The rotational rheometer is based on drag flow. The Couette type flow or flow between concentric cylinders is shown in Figure 2.5. The center cylinder is inserted into fluid and rotates; the angular velocity and the torque are used to determine the shear rate and shear stress for calculation of the viscosity. It can be used to measure viscosity from low to high shear rates. The free surface can be a limiting factor at high shear rate since it can induce measurement errors. Additional geometries are in the same rotational category: plate-plate, cone and plane, vane and others. Rotational rheometers are complex and expensive.

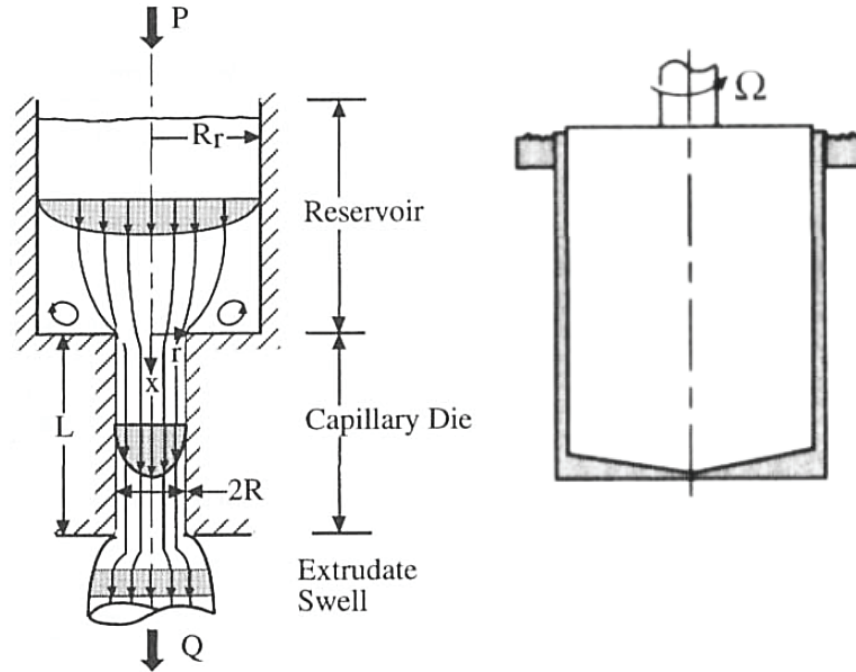


Figure 2.5 Capillary (left) and rotational (right) rheometers from [40].

Both of these methods need to be temperature controlled to satisfy the isothermal assumption during measurement. One can mix both methods to obtain precise viscosity curves from high to low shear rates [26].

Many models can be used to fit viscosity measurements of MIM feedstock. For a limited range of shear rates, the power law can be used [8, 41]:

$$\eta(\dot{\gamma}) = m \cdot \dot{\gamma}^{(n-1)} \quad (2.8)$$

Using logarithmic scales, the model behaves like a linear function with the “ $(n-1)$ ” coefficient as the slope.

$$\ln(\eta) = (n-1) \cdot \ln(\dot{\gamma}) + \ln(m) \quad (2.9)$$

Therefore, if  $n < 1$  (negative slope) the model is used for shear thinning fluids. In the opposite, if  $n > 1$  (positive slope) the model is used for shear thickening fluids. The model is simple but cannot be used when initial and final Newtonian plateaus are observed. Other

models exist but the following are the most frequent in literature. The first is the Cross model [40]:

$$\eta(\dot{\gamma}) = \eta_{\infty} + \frac{\eta_0 - \eta_{\infty}}{1 + (K\dot{\gamma})^{(1-n)}} \quad (2.10)$$

This model was found in different form with or without modification for yield stress in papers [9, 16, 17, 21, 22, 26-28]. The second is the Carreau-Yasuda model [40]:

$$\eta(\dot{\gamma}) = \eta_{\infty} + \frac{\eta_0 - \eta_{\infty}}{\left[1 + (\lambda\dot{\gamma})^a\right]^{\frac{1-n}{a}}} \quad (2.11)$$

This model can be found in papers [29] and [16]. When the “ $a$ ” parameter equals two, this equation is known as the Carreau model. In both models, when the shear rate tends toward zero, the viscosity equals  $\eta_0$  and when the shear rate tends toward infinite, the viscosity equals  $\eta_{\infty}$ . All variables are determined by fitting the model to experimental data.

It is also essential to define temperature dependence of the viscosity. In general, the Williams-Landel-Ferry model (2.12) or Arrhenius dependence (2.13) is used for variation of the  $\eta_0$  viscosity. Like in viscosity models, all variables are experimentally determined by doing viscosity tests at different temperatures. Generally, the  $\eta_{\infty}$  is not used for fitting viscosity and other variables are not considered temperature-dependent in MIM. Thus, no temperature model was found in literature for other coefficients of the viscosity models.

$$\eta_0(T) = \eta_r \cdot \exp\left(\frac{-C_1 \cdot (T - T_r)}{C_2 + T - T_r}\right) \quad (2.12)$$

$$\eta_0(T) = B \cdot \exp\left(\frac{T_b}{T}\right) \quad (2.13)$$

Finally, pressure can change viscosity. When submitted to high pressure (100 MPa) the viscosity of polymers increases [42, 43]. Still, this dependence is often ignored for MIM since there is a high solid fraction that is not affected by pressure.

### 2.2.2 PVT

The relationship between Pressure, Volume and Temperature is abbreviated as PVT. This data is needed for modeling the density evolution with pressure and temperature. During mold filling, the fluid is considered incompressible (2.3) since the feedstock compressibility factor is lower than  $\sim 10^{-9} \text{ Pa}^{-1}$  with maximum pressure variation of  $\sim 10^7 \text{ Pa}$  [44]. The compressibility factor ( $\beta$ ) is calculated with equation (2.14), where “ $v$ ” is the specific volume [3].

$$\beta = -\frac{1}{v} \left( \frac{dv}{dp} \right)_T = \frac{1}{\rho} \left( \frac{d\rho}{dp} \right)_T \quad (2.14)$$

After filling, the incompressibility assumption is no longer valid; the PVT data is needed since the pressure gradients are much higher during the packing phase. This data can be obtained from a dilatometer. This apparatus performs isobaric tests for a temperature range and records the volume variation to determine the specific volume as a function of pressure and temperature (PVT). The two-domain Tait model is appropriate for modeling PVT data (see equations (2.15) to (2.19)). The parameter  $v_0$  is the specific volume function at atmospheric pressure and  $B$  is the pressure sensitivity function [45]. Nine fitting coefficients are necessary:  $b_1$  to  $b_4$  are domain dependent and  $b_5$  to  $b_9$  are constants. A phase transition temperature,  $T_{trans}$ , determines the separation between the two domains of the Tait model. Two sets of coefficients  $b_1$  to  $b_4$  are then needed, the first set for temperature below  $T_{trans}$  (solid state) and the second for temperatures higher than  $T_{trans}$  (melt state).

$$v(T, p) = v_0(T) \left[ 1 - 0.0894 \cdot \ln \left( 1 + \frac{p}{B(T)} \right) \right] + v_t(T, p) \quad (2.15)$$

$$T_{trans} = b_5 + b_6 p \quad (2.16)$$

$T < T_{trans}$	$T > T_{trans}$	
$v_0(T) = b_{1s} + b_{2s}(T - b_5)$	$v_0(T) = b_{1m} + b_{2m}(T - b_5)$	(2.17)
$B(T) = b_{3s} \exp(-b_{4s}(T - b_5))$	$B(T) = b_{3m} \exp(-b_{4m}(T - b_5))$	(2.18)

$$v_i(T, p) = b_7 \cdot \exp(b_8(T - b_5) - b_9 p) \quad (2.19)$$

Figure 2.6 shows a typical PVT graph with a Tait model fitting. Discontinuities can be observed at the boundary between domains, which are limited by  $T_{trans}$  function.

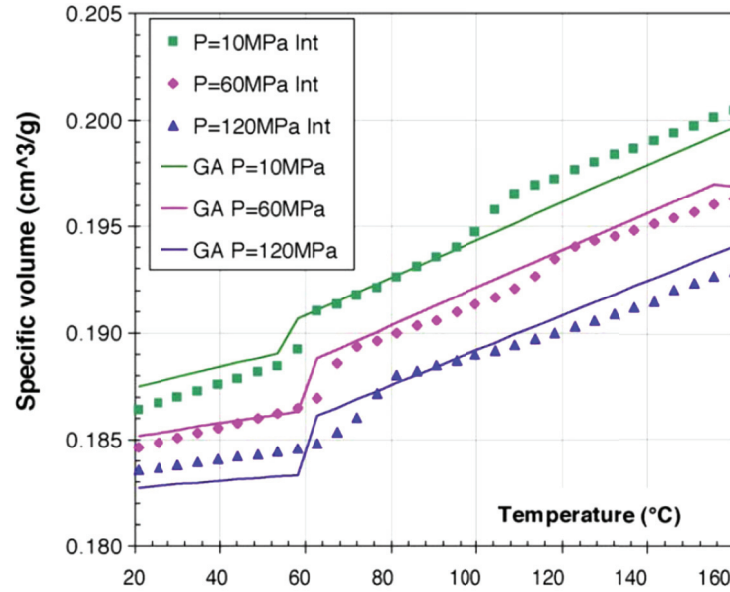


Figure 2.6 PVT results (points) with Tait model (lines) from [45].

### 2.2.3 Specific heat

The specific heat ( $C_p$  at constant pressure and  $C_v$  at constant volume) is defined as the amount of energy needed, per unit of mass, to raise the temperature by one degree.

Expressed in  $\frac{kJ}{kg \cdot K}$  or in  $\frac{J}{kg \cdot K}$ , the specific heat is temperature dependent and has peak

values during phase changes. A mean value of this properties is often used, but custom models can be implemented for simulation [21]. Differential scanning calorimetry is used to determine this variable over the operating temperature range of the feedstock [45, 46]. The test is conducted during heating or cooling. The choice of the heating or cooling rate can affect the results: Kowalski and Duszczuk [47] reported a decrease of the mean specific heat with increasing cooling rate with a stainless steel MIM feedstock as illustrated in Figure 2.7. They attributed this phenomenon to the undercooling effect. Since the feedstock is submitted to very high cooling rate, the authors concluded that higher rates give more

representative data. If the specific heat is lower, the melt temperature will decrease more rapidly, resulting in a higher viscosity and an increased pressure drop during mold filling.

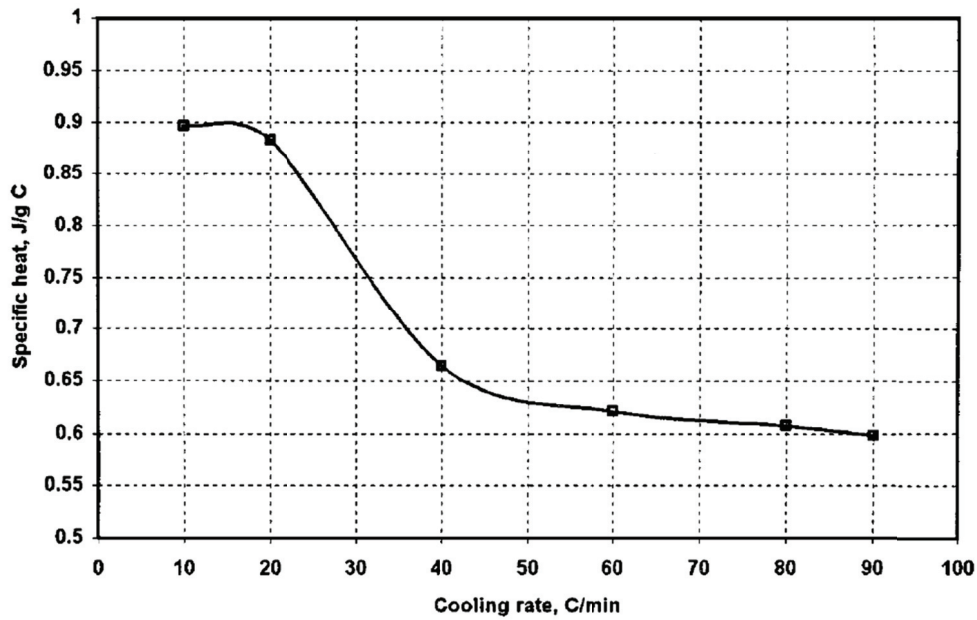


Figure 2.7 Cooling rate effect on mean specific heat for a 316L feedstock [47].

## 2.2.4 Thermal conductivity

The second parameter from the energy equation (2.4) is the thermal conductivity, defined as the ability to conduct heat. The flash method is used to obtain the solid or melt thermal diffusivity ( $\alpha$ ), which is linked to conductivity by equation (2.20) [46].

$$k = \alpha \cdot C_p \cdot \rho \quad (2.20)$$

All parameters in equation (2.20) are temperature dependent. Consequently, for a precise measurement of the thermal conductivity, each of them should be known as a function of temperature. Models exist for linking the thermal conductivity of the liquid and solid phase. The Maxwell model[48], the Lewis & Nielsen [48] and the Rayleigh-Devries models [45] have been used in the literature. One major problem for these models for MIM is the high solid fraction that can lead to erroneous estimations since the assumption that the particles are always separated by binder is no longer realistic. Kowalski *et al.* [48] reported that experimental measurement of conductivity is needed for accurate simulation of MIM.

### 2.2.5 Density

The density is defined in the PVT analysis since it corresponds to the reciprocal of the specific volume.

$$\rho = \frac{1}{v} \quad (2.21)$$

A reference density at ambient temperature and pressure is still needed. The Archimedes' principle can be used to determine density of the feedstock. For a precise measurement, this method requires a large sample volume to obtain a significant buoyancy effect on the total weight during water immersion. In addition, bubbles in water reservoir need to be avoided. With water, this method is only appropriate for material with higher than water density, making binder measurement impossible. A pycnometer is a more precise apparatus to measure density and it can characterize binders as well as metal powders. This method uses the Boyle's law (isothermal case of the ideal gas law [4]); the volume variation is calculated from pressure variation. The density is then calculated by dividing the sample mass (known prior to the test) by its volume.

### 2.2.6 Solid loading

For segregation modeling, the effect of solid loading on all previous properties is needed. For the viscosity, models like that of Krieger can describe the solid loading effect on viscosity [44, 49, 50]:

$$\eta(\phi) = \left(1 - \frac{\phi}{\phi_m}\right)^{-1.82} \cdot \eta_s \quad (2.22)$$

Where:

$\eta_s$  = Solvent viscosity (binder)

$\phi$  = Solid loading

$\phi_m$  = Solid loading where the viscosity becomes infinite

For energy related coefficient, no model applied to MIM has been found. The segregation phenomena in MIM and modelling of non-isothermal flow are challenging areas of research

for the future. Repeating PVT, specific heat and thermal conductivity tests at different solid loadings would make modeling possible for a specific feedstock, but it is costly and time consuming.

## **2.3 Experimental validation**

Since many assumptions and approximations are required to simulate MIM, numerical results have to be verified by experimentation. Four methods have been found in literature and are explained below.

### **2.3.1 Short-shots**

Injecting short-shots is a widely used method in MIM [22, 26, 28, 34, 45]. It consists in interrupting the flow before the front reaches the end of the mold cavity. The uncompleted parts are examined to determine the flow path during the filling and compared with numerical simulations. For a conventional molding machine, the screw movement is controlled during the filling by operators. Specific screw speeds are imposed depending on mold geometry. Knowing the effective area of the piston, the screw speed can be converted in flow rate. These operating characteristics make short-shot molding easy, since the screw can be stopped during its stroke, giving unfilled parts with corresponding filled ratio. Figure 2.8 gives an example of short-shots used to validate simulation results [45].

For this project, short-shots are not possible due to a different injection principle: the velocity of the melt is not imposed; rather a constant inlet pressure is imposed. Consequently, interruptions are very difficult to achieve and repeatability issues are common. For these reasons, this method will not be applied to the current project.

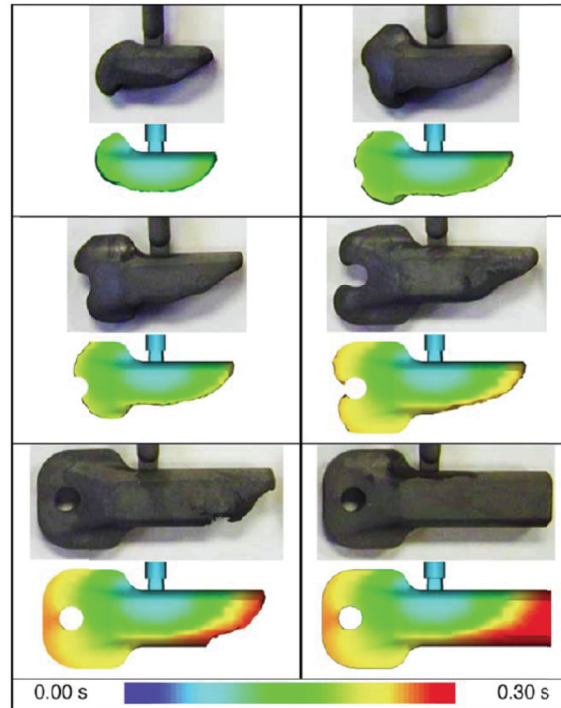


Figure 2.8 Short-shots comparison with simulation [45].

### 2.3.2 Instrumented mold

The cavity of the mold can be instrumented with transducers and thermocouples to study the evolution of pressure and temperature. Ilinca *et al.* used two pressure transducers inside a rectangular mold cavity [21]. A third pressure transducer and a thermocouple gave the nozzle pressure and temperature. Their thermocouple was set directly in the melt. The recorded data was used for the validation of their simulations. Bilovol *et al.* also added transducers and thermocouples to a mold for the comparison of three software [16]. A Kistler piezoelectric transducer recorded the pressure and three type K thermocouples recorded wall temperatures with sampling at 20 Hz. These results gave the authors a basis for their comparison. They also studied viscosity models with pressure curves [29]. Ahn *et al.* [19] used three pressure transducers (model 6183AE), also from Kistler. The signal was enhanced by an amplifier and recorded by a data acquisition board. The effect of wall temperature distribution and slip layer was studied with the recorded data. Their simulation correlation was better when the cavity wall temperature distribution was taken into account. Finally, five pressure transducers were added to a plastic injection mold in a

study presented in a book by Kamal *et al.* [3]. Even if results were obtained from the behavior of molten polymer, the study is well defined and gives many factors that have an impact on pressure curves, such as the viscosity model, the mold deformation and gate thickness. A schematic illustration of the instrumented cavity is given in Figure 2.9.

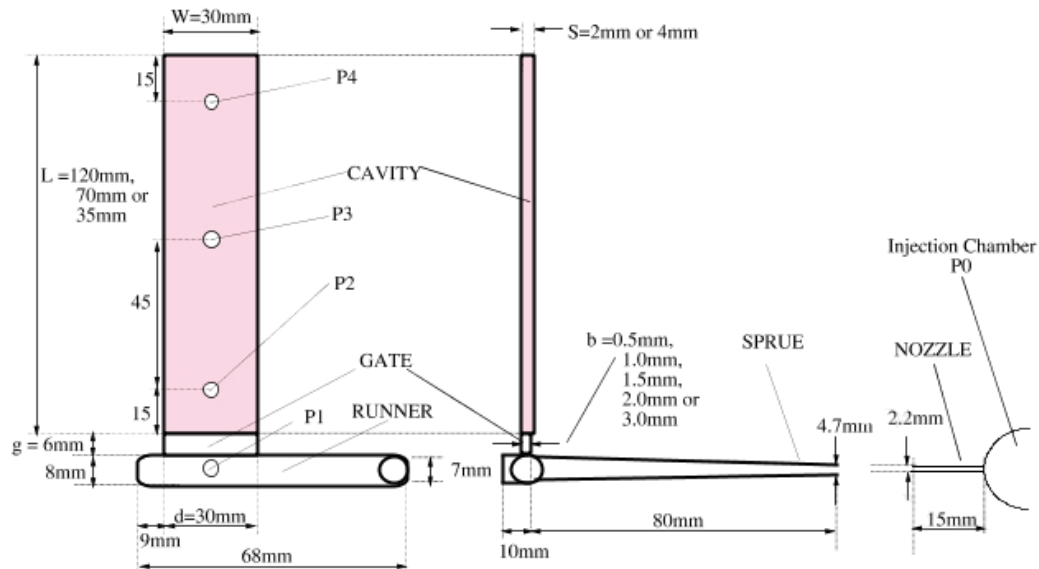


Figure 2.9 Cavity with pressure sensors positions studied in [3].

Using pressure curves, the authors identified the three main stages during injection: filling, packing and cooling (see Figure 2.10). The pressures P0 to P4 are represented by different line formats. Important pressure drops are observed between positions 1 to 4. This method can be easily implemented in a simple P&WC mold and can provide valuable characteristics (e.g. pressure level, melt front position and filling time) of the cavity flow for simulation or experimental studies. For precision measurements, transducers have to be selected specifically for this project to respect the pressure range.

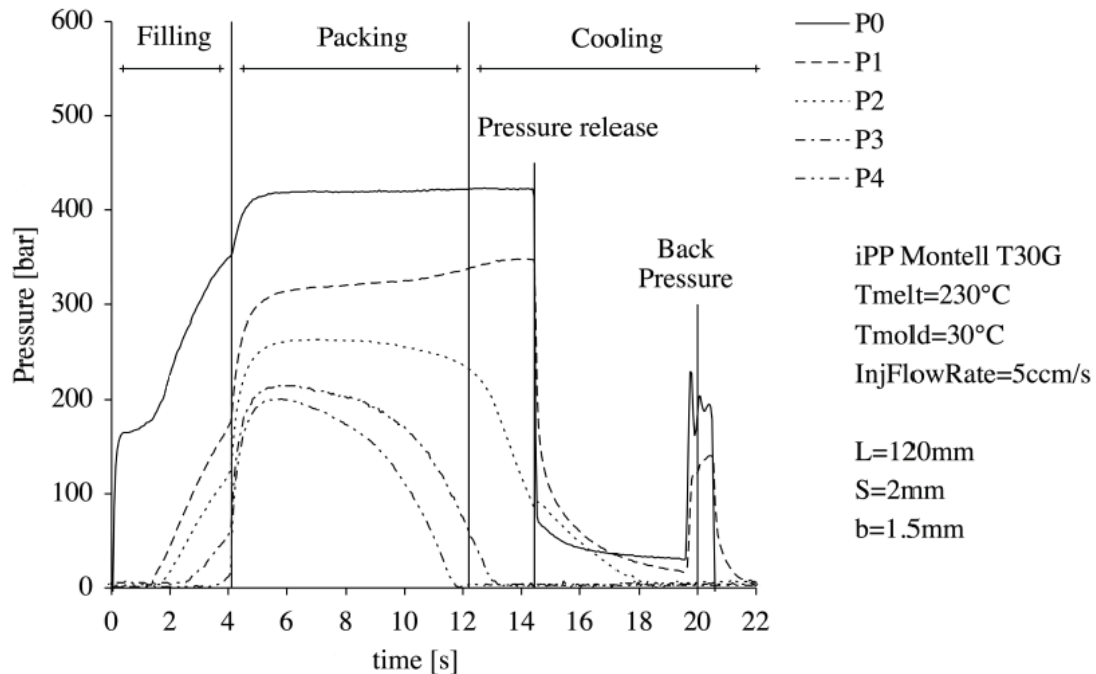


Figure 2.10 Typical pressures curves in plastic injection molding [3].

### 2.3.3 High speed camera

The third method of validation is to directly record the flow inside the cavity with a high speed camera. No paper was found on using this method for PIM. However this technology has been used for plastic molding and is well detailed in the literature. Yokoi *et al.* studied flow front and bubble formation with a camera [51]. They made an apparatus for flow front tracking and observed instabilities in the flow (two distinctive flow fronts) for high injection rates. They used a HAS-TURTLE camera for capturing flow front in a rectangular mold with two glass windows (see Figure 2.11). A complete chapter explains different visualization techniques in reference [3]. Mirrors can be used to change image orientation or to illuminate the mold from a different angle. For conventional molding, thick glass or multi-layered glass are needed to sustain the high cavity pressure ( $\sim 200$  MPa) and the temperature of the feedstock ( $\sim 200^\circ\text{C}$ ) [1]. Clamping force and pressure acting on the surface make construction of visualization mold challenging.

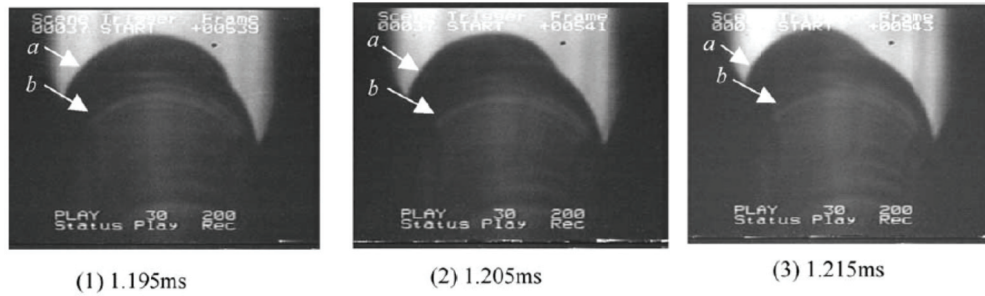


Figure 2.11 High speed camera result, nearside (b) and backside(a) flow front [51].

### 2.3.4 Tomography

The last method is tomography. This method is used to visualize density variation inside a part. Multiple section analyses are performed and assembled to reconstruct the initial part. For micro tomography, the final reconstitution is made with very small voxel (volume element, three-dimensional pixel) for smaller parts precision. X-ray micro tomography can be used to observe binder separation in MIM, like in Thomas *et al.* paper [26]. A 6  $\mu\text{m}$  cubic voxel resolution was obtained with the X-tek HMXST 225 X-ray microfocus system. They observed binder separation at the gate where the shear rate was higher. After a numerical filling simulation, they found some correspondences between flow lines and the binder layer profiles (see Figure 2.12). The authors suggested that the cause of this large defect is segregation at the gate that was propagated by the flow through the mold. This method generates very large results files and is expensive. Quantitative results (in term of solid loading) are difficult to obtain since a calibration is needed for each new material.

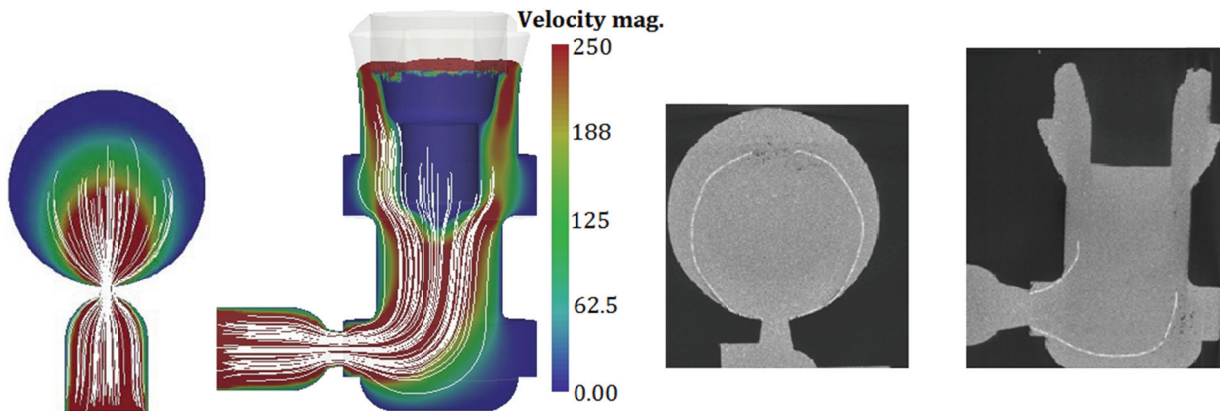


Figure 2.12 Numerical velocity and flow lines compared to micro tomography [26].

## CHAPTER 3. METHODOLOGY

This chapter presents the materials, equipment, software, procedures and experimental plans for the realisation of this project. It is divided in three parts: process experimentation, feedstock characterization and numerical simulation.

### 3.1 Process experimentation

#### 3.1.1 Feedstock

The PWME-10-34 feedstock was used for this study. It is made of nickel superalloy powder, produced by gas atomization at Sandvik Osprey, and a mix of thermoplastics. The  $d_{90}$  (90 % of the powder size distribution) was below 22  $\mu\text{m}$ . Standard procedures at P&WC were used to measure and mix every ingredients. The feedstock solid loading was constant for all tests.

#### 3.1.2 Injection press

The production press 17040-01 of P&WC was used for this study. Three parameters need to be set in the interface: Injection pressure, injection time and feedstock (melt) temperature. The press can also control mold temperature but none of the molds used in this study had the necessary cooling channels.

#### 3.1.3 In-cavity measurement

##### 3.1.3.1 Mold

In-cavity measurements were performed with a rectangular mold with four pressure transducers and four thermocouples. Omega pressure transducers were mounted flush with the mold surface, each separated by one inch and aligned on the centerline. The relation between voltage and pressure was defined with the factory calibration sheets. Values from these calibrations were used to fit a linear equation ( $p(mV) = m \cdot (mV) + b$ ) for each transducer, a summary is presented in Table 3.1. The pressures are shown in relative value from the injection pressure “ $P_I$ ” used with this mold to respect intellectual property.

Table 3.1 Calibration values and linear coefficient for cavity transducers.

	Sensor 1	Sensor 2	Sensor 3	Sensor 4
Type	PX610	PX610	PX610	PX610
Pressure (psig)	Output (mV)	Output (mV)	Output (mV)	Output (mV)
0	0,049	-0,028	-0,040	0,004
142.9% of $P_i$	4,410	4,476	4,650	5,176
285.7% of $P_i$	8,810	9,088	9,401	10,436
m	11,414	10,970	10,592	9,586
b	-0,483	0,500	0,531	0,104

According to Omega technical services, these units have a response time of about 1 ms. Type K thermocouples were installed at the same distances from the gate but with a 0.281" offset in the width direction (see Figure 3.1 for a detailed view of the mold with sensors positions). The distance between the thermocouple tips and the mold wall is half the thickness of the part: 1/16". These thermocouples were positioned directly in the middle of the melt to avoid walls thermal inertia effect on readings. Closed bead thermocouples of 1/16" were used for durability and fast response times. All the temperatures are normalized by the glass transition temperature of the binder to respect intellectual property.

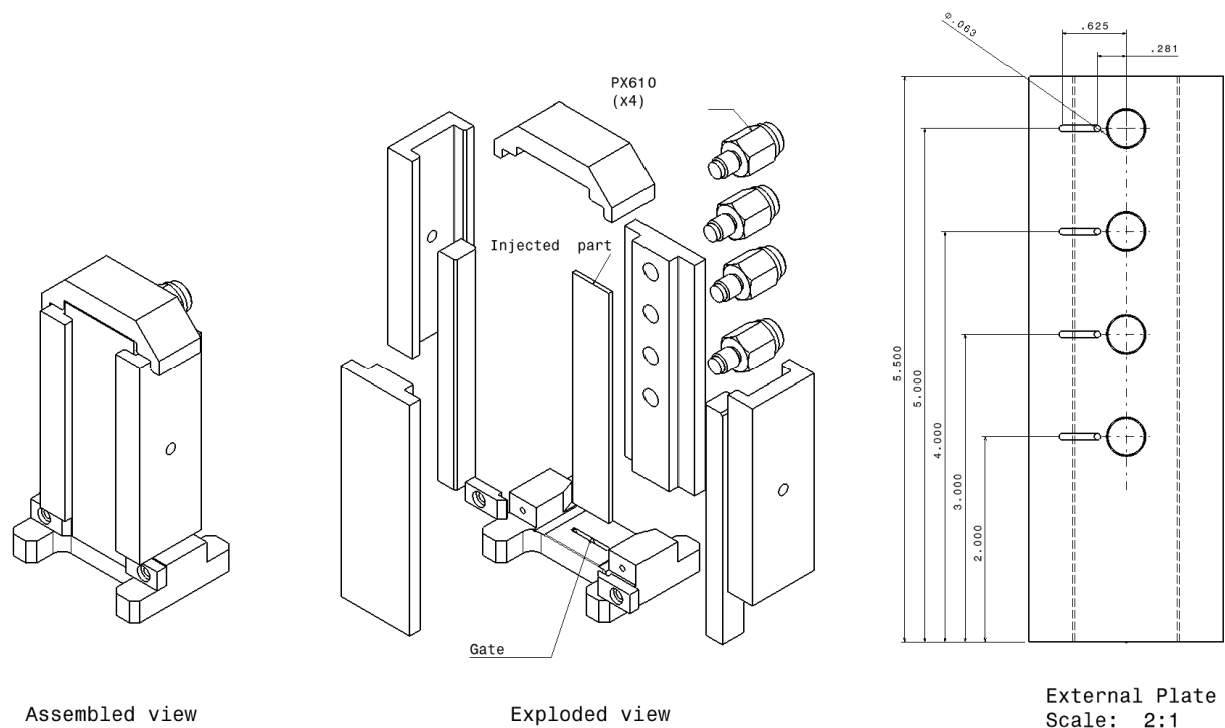


Figure 3.1 PF505171: Assembled and exploded view with positioning of sensors.

In addition, an acquisition block was placed between the mold and the press to obtain inlet conditions. This block had one pressure transducer, two type K thermocouples and was temperature-controlled by the press. The transducer used at the inlet, a GP:50 217, had no calibration sheet. The full scale divided by the maximum voltage was used to convert the output signal to psig.

### 3.1.3.2 Set-up

The data acquisition system included the following items:

- 2 Computers (PC01 and PC02)
- DaqView software(for each computer)
- 2 Acquisition boards (Omega Personal DAQ-3000 and DAQ-3005)
- 6 Type K thermocouples
- 4 PX610 transducers
- 1 GP:50 217 transducer
- 2 DC sources
- PF505171 mold
- Acquisition block
- Injection press (17040-01)
- Electric wires for the recording trigger

Figure 3.2 illustrates how the system was connected together. One acquisition board was set to record the pressures and the other to record the temperatures. Both of them were working in differential mode: necessary for connecting thermocouples to the acquisition board and preferable for the pressure transducers to minimize signal interference between inputs. Every temperature channel had cold junction compensation and was set for type K signal input. For synchronisation, the analog output of the DAQ-3000 was wired in parallel

to each recording trigger input. This output was controlled manually in one of the computer. Scan rate was set to 5 kHz with an oversampling of 16. The output files were ASCII text files with timestamps relative to the trigger point. The acquisition block temperature was set to the melt temperature on the thermostatic heater to avoid feedstock cooling in the block.

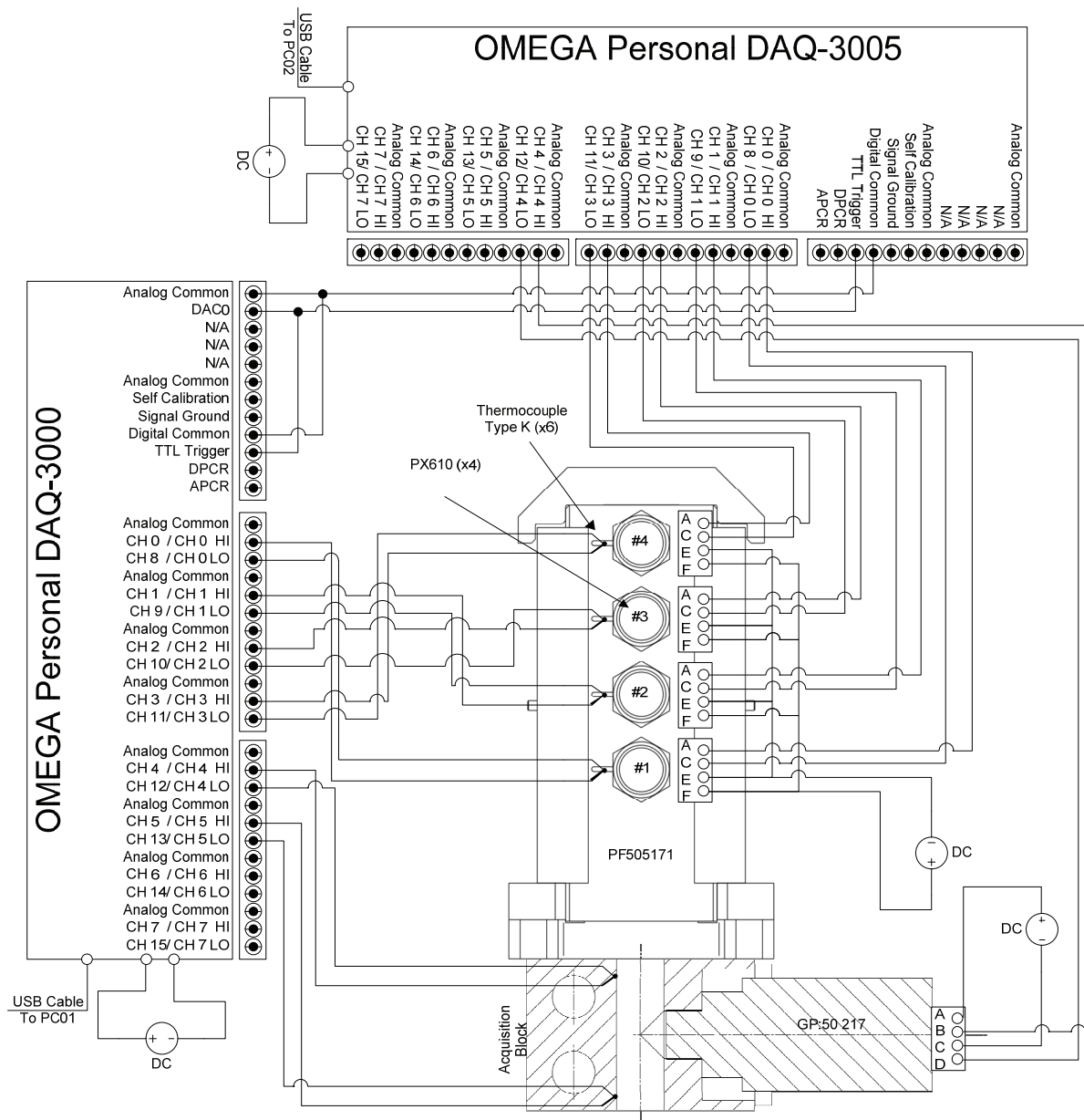


Figure 3.2 Data acquisition system with wiring.

### 3.1.3.3 Data conditioning

Since files generated by each injection with this setup are huge (~20 MB text files), the first step was to reduce their size before any treatment. With the help of Richard Masson from P&WC, a small C # moving average program was compiled (See Appendix 1). This program allows user to define subsets size and calculates columns average for each subset. Additionally, the program transforms time in decimal seconds and removes unnecessary lines and columns. With this program, pressure results passed from 5 kHz to 500 Hz with a subset of 10 samples and temperature results passed from 5 kHz to 20 Hz with a subset of 250 samples. The subsets size for the temperature was chosen larger in order to filter the noisy signal of thermocouples. Figure 3.3 shows the difference between raw and treated data for pressure and temperature signals.

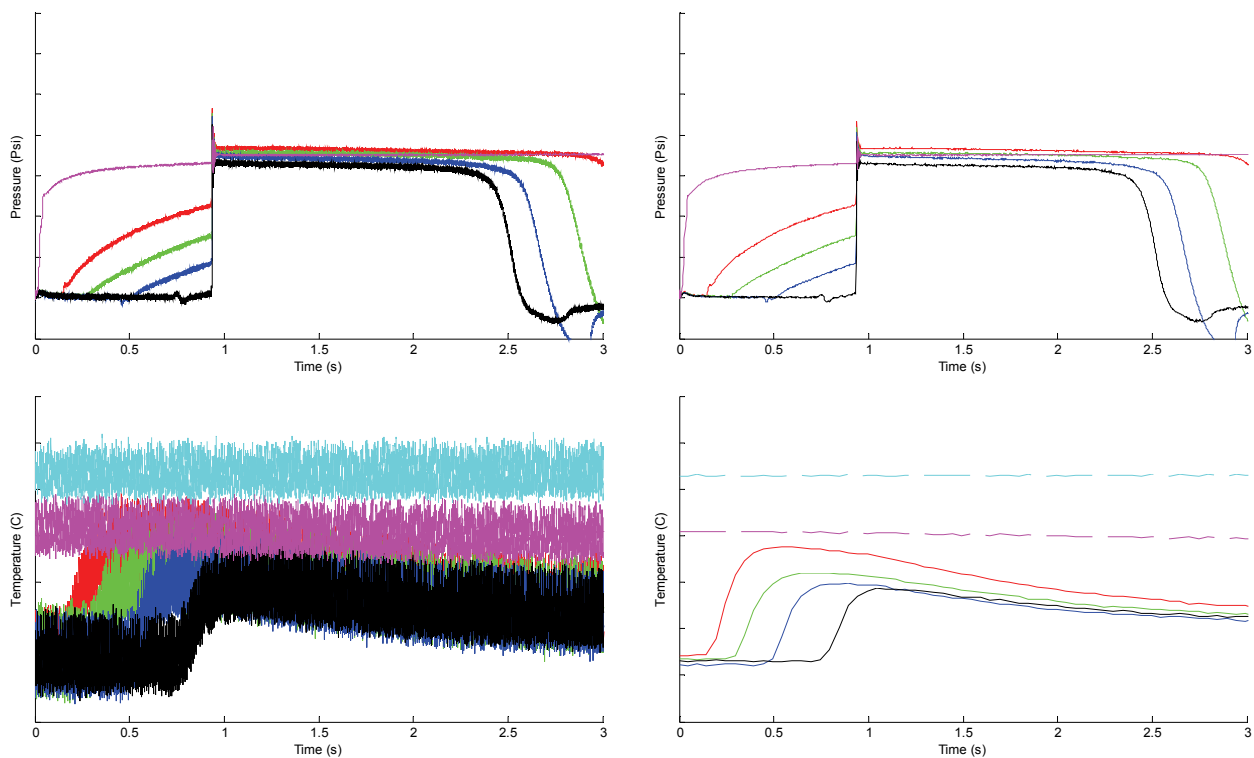


Figure 3.3 Data before (left) and after (right) conditioning.

The treated files were imported in Matlab for signal conversion and plotting. For transducers, initial offset was calculated from the average of the first 100 readings (before injection start) and scaled with the specific factors described previously. Thermocouples signals were already in Celsius, no scale or offset were involved (for the current project, the

complete temperature reading system was calibrated once by Dynaterm before acquisition). The last step was to normalize time for easier comparison between tests. The time zero was attributed to the first inlet pressure value over 1 psig. The same time offset was applied to every channel.

### 3.1.3.4 Experimental plan

A total of 45 samples were injected for pressure and temperature measurements. First a repeatability test was performed at  $P_1$  psig. Then the pressure effect was studied with five other pressures. For the study of the mold temperature, two temperatures setting were used with the  $P_1$  pressure. These mold temperatures are not exact since imprecise temperature labels were used to determine the mold condition. Thus, these temperature variations can be considered rather as a qualitative test: cold, hot and standard. Finally, three pressures were tested with a lower melt temperature. Table 3.2 summarizes conditions (pressure and temperature are normalized for intellectual property reasons) and number of samples for these tests.

Table 3.2 Experimental plan for in-cavity acquisition.

Mix	Mold	Injection Parameters			Number of Samples	Use
		Pressure (psig)	Feedstock Temp. / $T_g$ (°C / °C)	Mold Temp. / $T_g$ (°C / °C)		
PVMIE-10-34	PF656171	$P_1$	1,7	0,8	8	Repeatability
		28,5% of $P_1$			4	Pressure effect on temperature and pressure in the mold
		42,9% of $P_1$			4	
		71,4% of $P_1$			4	
		142,9% of $P_1$			4	
		171,4% of $P_1$			4	
		$P_1$	1,7	0,6	4	Effect of mold temperature
		$P_1$		0,9	4	
		$P_1$	1,6	0,7	3	Effect of lower melt temperature
		142,9% of $P_1$			3	
		171,4% of $P_1$			3	
Total				45		

## 3.1.4 High speed camera

### 3.1.4.1 Mold

The traction bar mold PF65612 was selected for high speed camera visualization. Every parts of the mold are normally made of tool steel. For this project, one steel part has been replaced on one side by a machined polycarbonate part. The polycarbonate was selected for

its transparency, impact strength, stiffness and temperature resistance. Replacement parts were milled in a half-inch sheet of abrasion-resistant polycarbonate from McMaster-Carr (product number 8707K151). The external and internal faces were not milled since the thickness was already at the right dimension. Repetitive injections showed that the material was not scratched by the feedstock. As a result, only a single part of polycarbonate was needed for all experiments. An assembled and exploded view of the traction bar mold is given by Figure 3.4.

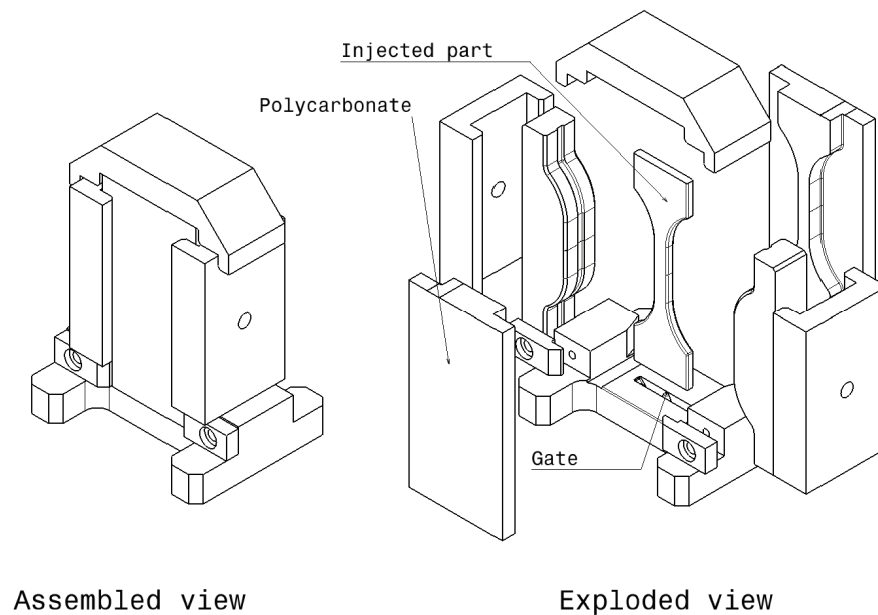


Figure 3.4 PF65612: Assembled and exploded view.

### 3.1.4.2 Set-up

The high speed camera system included the following items:

- Computer
- Portable hard drive
- Phantom V7.3 high speed camera
- Phantom recording software
- 6 Halogen lamps
- 3 Tripod stands (two for the lamps and one for the camera)

- PF65612 mold
- Injection press (17040-01)

Figure 3.5 shows a top view of how items were positioned during acquisition. The camera was placed normal to the clear part on a tripod stand. The halogen lamps were mounted by groups of three on each sides of the camera, oriented toward the mold. The camera recorded the injection behind the safety clear shield mounted in front of the press.

The Phantom V7.3 camera was set to a resolution of 256 X 512 pixels at 4000 frames per seconds. The triggering was made manually with a push button before each injection. After the recording of a sample, the video was shortened to remove sequences before and after the filling. The stored videos had an approximate size of 1 GB each.

#### **3.1.4.3 Data conditioning**

Videos were analysed with Phantom Cine Viewer 649 software. The “sharpen” image processing filter was the only modification applied to all videos. For evaluation of the flow front position, five virtual filled levels were defined on the mold as shown by Figure 3.6. These levels were used to analyse the video results for simulation comparison: When the front was visually reaching one of the levels, the time was recorded. The first level was used to set the zero-time reference. Images were extracted from the video with the same software.

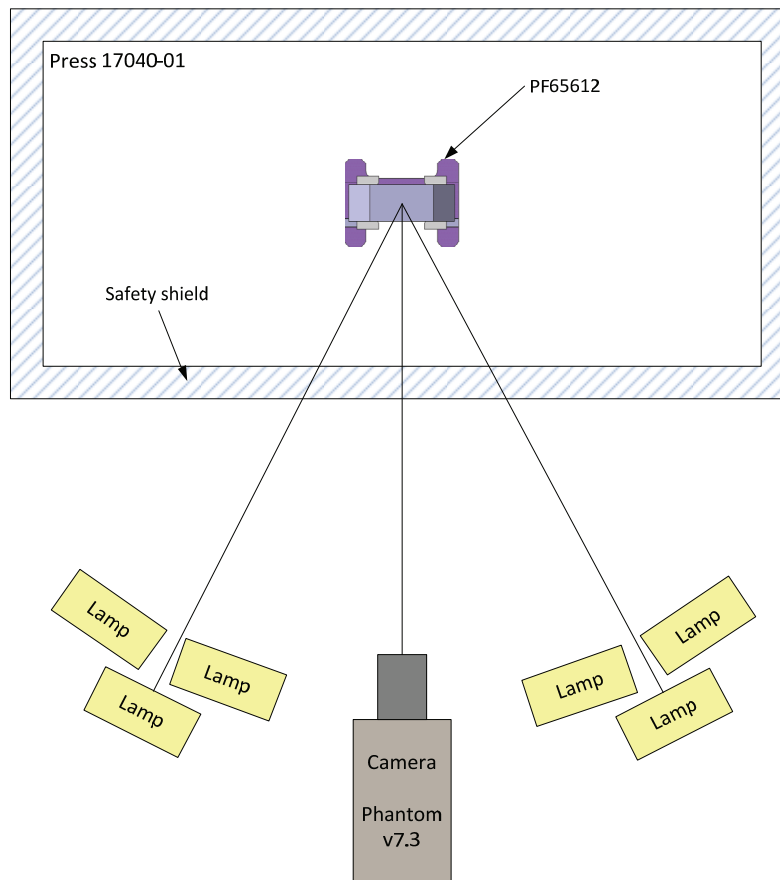


Figure 3.5 High speed camera system.

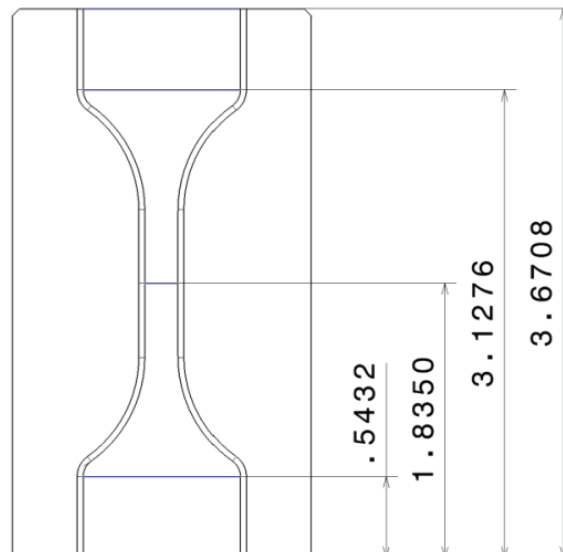


Figure 3.6 Virtual filled level on the mold front view (displayed in blue, units: inches).

### 3.1.4.4 Experimental plan

As for in-cavity measurements, a repeatability test was performed using the mold standard pressure. For this mold, the standard pressure is lower than the PF505171 mold since it is shorter with a similar cross-section:  $P_T$  psig. The purpose of the second test was to observe the pressure effect on the filling behavior. Five pressures were tested from 20% to 240% of  $P_T$ . Finally, the mold temperature effect was verified with two different mold temperatures. Once again these temperatures are not exact since this mold was not temperature-controlled and inaccurate temperature labels were used for control. These tests are summarized in an experimental plan presented by Table 3.3.

Table 3.3 Experimental plan for high speed camera.

Mix	Mold	Injection Parameters			Number of Samples	Use
		Pressure (psig)	Feedstock Temp./Tg (°C / °C)	Mold Temp./Tg (°C / °C)		
PWME-10-34	PF66612	$P_T$	1,5	0,8	7	Repeatability
		20% of $P_T$			2	Pressure effect on filling
		40% of $P_T$			2	
		140% of $P_T$			2	
		200% of $P_T$			2	
		240% of $P_T$	5			
		$P_T$	1,5	0,6	2	Effect of mold temperature on filling
		$P_T$		0,9	2	
		Total				

## 3.2 Feedstock Characterization

### 3.2.1 Viscosity

Viscosity measurements on feedstock PWME-10-34 were performed on three rheometers. Each of these devices had specific parameters and geometries described below.

#### 3.2.1.1 Rheometers and parameters

The first rheometer was a Bohlin CVO-50 from Malvern owned by *École de technologie supérieure*. The methodology previously developed by Frédéric Wallman was used. He has studied the effect of multiple parameters on measurement repeatability and has established the standard procedure for feedstock viscosity measurement with this rheometer for P&WC:

1. Heat stator cylinder to the desired value

2. Insert pre-heated feedstock in the cup ( $\sim 2\text{ml}$ )
3. Install C14 DIN 53019 bob
4. Insert bob and set the gap to  $7365\ \mu\text{m}$
5. Set parameters in the software
6. Start the test

The parameters were shear rates from 0 to  $1200\ \text{s}^{-1}$  with 30 points in log scale, 1 s delay time and 10 s integration time. For temperature and solid loading homogeneity, tests also included a pre-conditioning for 5 min at a shear rate of  $100\ \text{s}^{-1}$ . For each test, a new sample of feedstock is used to eliminate deviation caused by segregation at high shear rates.

The second rheometer was an AR-2000 from TA Instruments owned by *École Polytechnique Montréal*. It was also equipped with a fluid heater for temperature control. For this rheometer, a vane tool combined to a serrated cup was used. This geometry was selected to avoid slip and segregation [40]. The bob diameter was two times larger than the one used with the Bohlin. The methodology for viscosity measurement was similar to the previous one:

1. Install vane tool and calibrate
2. Perform a rotational mapping
3. Set the zero gap
4. Set parameters in the software
5. Heat stator cylinder to the desired value
6. Remove the vane tool
7. Insert pre-heated feedstock in the cup ( $\sim 15\text{ml}$ )
8. Reinstall the vane tool
9. Start the test

The steps 1 to 3 are mandatory only at the beginning of a test series or if the geometry is changed. The shear rate varied from  $0.1$  to  $1000\ \text{s}^{-1}$  with 7 points per decade, the gap was set to  $8000\ \mu\text{m}$ , the consecutive tolerance was 5% and the maximum point time was 5 s. The complete settings for the AR-2000 are given in Appendix 2.

The last rheometer is a SR-200 from Rheometric Scientific owned by NRC-IMI. The tests were performed by Pierre Sammut, technician at NRC-IMI. It was used in controlled shear

stress mode with two 25 mm diameter parallel plate separated by a 1 mm gap. The temperature was set to 1.5 times the mean glass temperature transition with a nitrogen atmosphere. The purpose of this rheometer was for validation of the viscosity data obtained from the previous devices.

### 3.2.1.2 Calibrated fluids

For verification of the AR-2000 rheometer, three calibrated Newtonian fluids were tested. These viscosity reference standards were custom made by Cannon by specifying the desired temperature and viscosity. These specifications were selected to get a representative verification of the normal operating conditions. Table 3.4 lists all the calibrated fluid used.

Since the calibrated fluids are Newtonian, they should have a constant viscosity at any shear rates. Consequently, viscosity tests were performed on these fluids for a large range of shear rates to observe the Newtonian plateau and compare the recorded viscosity with the certified one. For clarity and the protection of P&WC intellectual property, the results were converted in relative error using the difference divided by the certified value.

Table 3.4 Cannon certified viscosity reference standard list.

Standards	R5000	R12500	R30000
Lot number	110308	110308	110308
Temperature	$1,5 \cdot T_g$	$1,5 \cdot T_g$	$1,5 \cdot T_g$
Dynamic Viscosity/ Mean Polymer Mix Viscosity	40,86	100,84	250,2
Certification date	8/3/2011	8/3/2011	8/3/2011
Expiration date	31/3/2013	31/3/2013	31/3/2013

### 3.2.1.3 Curve fitting

The final step for viscosity measurements is fitting a model to the experimental data. The Cross model was used for every viscosity curves (see equation (2.10) in the previous chapter). The Carreau-Yasuda model could have also fitted the experimental data, but no data in the initial Newtonian plateau were acquired to adequately define the additional parameter “ $a$ ”. A normalized least square method was used to fit the Cross model to viscosity measurements. The normalization was added to avoid the large viscosities to dominate the optimization over small viscosities. With the Microsoft Excel Solver add-in, a

non-linear minimization of the normalized sum of squared residuals “ $S$ ” defined by equation (3.1) was performed:

$$S = \sum_{i=1}^n \left( \frac{y_i - f(x_i)}{y_i} \right)^2 \quad (3.1)$$

$n$  = Number of data

$i$  = Increment

$x_i$  = Independent variable

$y_i$  = Dependent variable

$f(x_i)$  = Estimated Dependent variable

For viscosity fit, the “ $x_i$ ” is the measured shear rate, the “ $y_i$ ” is the measured viscosity and “ $f(x_i)$ ” is the numerical viscosity at the measured shear rate. Automatic scaling option,  $10^{-5}$  convergence factor and a constraint precision of  $10^{-6}$  were the parameters selected in Excel solver.

In addition to the Cross model, the temperature-dependence of the viscosity needs to be modeled. Since the chosen viscosity model had an initial and final plateau ( $\eta_0$  &  $\eta_\infty$ ), two temperature models were required. As in the literature review (see sub-section 2.2.1.2), a Williams-Landel-Ferry model (WLF) was used to fit the initial viscosity  $\eta_0$ . For the final viscosity  $\eta_\infty$ , an exponential model was used. The least square method was used without normalization since the range of values was smaller. The same optimization method was used to minimize “ $S$ ” in the equation (3.2):

$$S = \sum_{i=1}^n (y_i - f(x_i))^2 \quad (3.2)$$

The following procedure has been applied to define the viscosity as a function of shear rate and temperature:

1. Fit Cross model  $\eta(\dot{\gamma}) = \eta_\infty + \frac{\eta_0 - \eta_\infty}{1 + (K\dot{\gamma})^{(n-1)}}$  to data at a reference temperature with four variables ( $K$ ,  $n$ ,  $\eta_0$  &  $\eta_\infty$ )
2. Record non temperature-dependant variables for the next fits ( $K$  &  $n$ )

3. Fit model to experimental data for each temperature using the two remaining variables ( $\eta_0$  &  $\eta_\infty$ )
4. Plot  $\eta_0(T)$  &  $\eta_\infty(T)$
5. Fit temperature WLF model to  $\eta_0(T)$  and exponential model to  $\eta_\infty(T)$
6. Combine equations and verify fit with experimental data.

### 3.2.2 Pressure Volume Temperature (PVT)

The PVT test was performed by Richard Gendron with a custom apparatus at IMI-NRC. The system is composed of cylindrical chamber with a moving piston (more details are available in Piche *et al.* [52]). For isobaric measurements, the linear movement of the piston is recorded during cooling or heating at a constant pressure. Knowing the diameter of the piston, the volume change can be calculated and used to determine the specific volume or density. A first test was done with the binder to seal the passages around the test chamber and avoid measurement errors. Then, the feedstock was tested at about 10 MPa from ambient temperature to standard melt temperature. No other pressures were tested since the operating pressure during injection is lower than 10 MPa which is the minimum pressure possible with this apparatus. Tests can be performed at higher pressures and extrapolated to get the low-pressure behavior, but for representative data they should be performed inside the range of operating conditions. No suitable apparatus was found during the current project to get PVT data near the operating conditions.

### 3.2.3 Specific heat

The specific heat was defined with a Q2000 DSC from TA Instruments by Shirley Mercier at IMI-NRC. The direct specific heat method was used. Four tests were performed with a heating rate of 20°C/min. Each test was done with a different reference temperature to set the zero heat flow. These temperatures were chosen outside the phase transition range; 0, 0.5, 1.6 and 2.4 times the glass transition temperature of the feedstock. Two other tests were performed to verify the effect of a lower heating rate (10°C/min).

### 3.2.4 Thermal conductivity

The thermal conductivity was calculated from the thermal diffusivity by equation (2.20). Thermal diffusivity was obtained from the laser flash method with a Flashline 5000 from Anter Corporation at IMI-NRC. The test involves heating one side of the sample with a laser and record the time needed before the heat flux raises the temperature on the opposite side. The samples were cylindrical with a diameter of 0.4375" and a thickness of 0.075" and they were directly taken from an injected traction bar with PWME-10-34 feedstock. Five samples were tested at three temperatures:  $0.5 \cdot T_g$ ,  $0.8 \cdot T_g$  and  $1.4 \cdot T_g$ .

### 3.2.5 Density

The room temperature density of powder and feedstock was determined with an AccuPyc 1330 pycnometer owned by IMI-NRC. This gas pycnometer consists of two chambers of known volume, a pressure transducer and a valve. It calculates the sample volume by recording the pressure before and after an increase of the total volume. An adapted formula from Boyle's law is used:

$$V_{sample} = V_{Chamber} - \frac{V_{ref}}{\frac{P_1}{P_2} - 1} \quad (3.3)$$

$V_{sample}$  = Volume of the sample

$V_{Chamber}$  = Volume of the sample chamber

$V_{ref}$  = Volume of the reference chamber

$P_1$  = Gauge pressure when the  $V_{Chamber}$  and  $V_{ref}$  are not connected

$P_2$  = Gauge pressure when the  $V_{Chamber}$  and  $V_{ref}$  are connected

The sample weight is measured prior to the test on a precision balance by the operator to allow the calculation of the density. The test is generally repeated until a satisfactory standard deviation is observed between repetitions.

Because the density measurements were performed earlier in this project, this test was not performed on the PWME-10-34 feedstock like for other characterisations. The density of PWME-10-18 feedstock, acquired with the pycnometer, was rather used as the theoretical

ambient conditions density for simulation. This feedstock was made with the same procedures, the same solid loading and the same powder alloy as PWME-10-34 feedstock. The only difference was the fabrication lot number.

### **3.3 Numerical simulation**

#### **3.3.1 Hardware**

All simulations were performed on a computer cluster with 128 Intel Xeon 3.4 GHz processors owned by the IMI-NRC. The number of processors used varied from 16 to 40 depending on the mesh size and availability, resulting in a computational time between 1 and 7 hours per tests.

#### **3.3.2 Mesh**

The cavity geometries were created and converted in step 203 format with Catia V5. Then, these geometries were imported and meshed with MSC Patran with linear tetrahedral elements. Mesh seeds were used to define the number of element in the thickness, length and width direction. The size of the tetrahedral element used was generally around 0.025" with refinement near the rounded corners. The resulting nodes were optimized using a GBBS-Pool-Stk method based on the profile criteria. Two boundary conditions were applied: pressure on the inlet of the mold and convection on external surface of the mold (entered values are not important since the pre-processor overwrites them). Finally, the meshes were exported in a neutral format. Figure 3.7 shows an example of the resulting mesh.

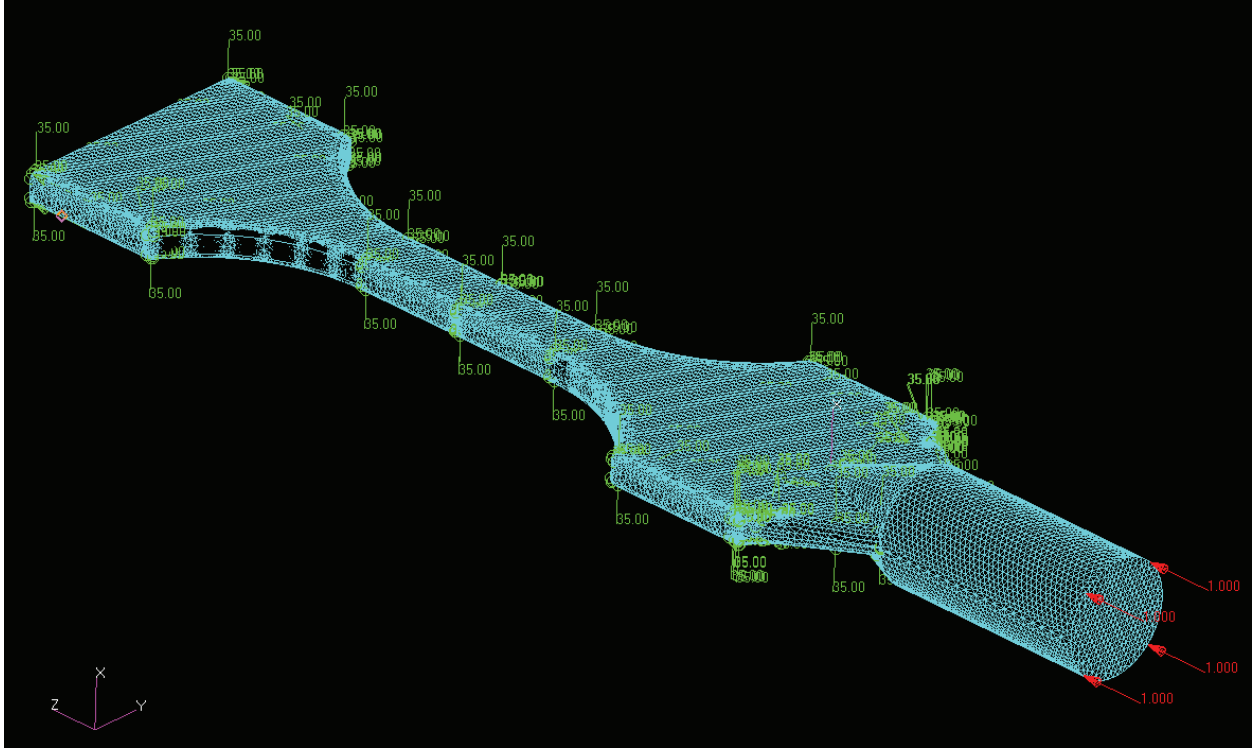


Figure 3.7 Traction bar meshed with tetrahedral element with boundary conditions.

### 3.3.3 Nondimensionalization

To avoid unit errors, the simulations were all performed with dimensionless parameters. The next sub-section defines the steps used for nondimensionalization.

Starting with the momentum equation (2.1), the dimensionless parameters are:

$$\tilde{\rho} = \frac{\rho}{\rho_0}, \quad \tilde{\mathbf{U}} = \frac{\mathbf{U}}{U_0}, \quad \tilde{t} = \frac{t}{t_0} = \frac{t \cdot U_0}{L_0}, \quad \tilde{\nabla} = \nabla \cdot L_0, \quad \tilde{p} = \frac{p}{p_0}, \quad \tilde{\mu} = \frac{\mu}{\mu_0} \quad \text{and} \quad \tilde{\mathbf{g}} = \frac{\mathbf{g}}{g_0}$$

Where the tilde identifies a dimensionless parameter and a subscript 0 identifies a reference value. A dimensionless form of Navier-Stokes equation can be obtained by using the above relations:

$$\frac{\rho_0 U_0^2}{L_0} \cdot \tilde{\rho} \left( \frac{\partial \tilde{\mathbf{U}}}{\partial \tilde{t}} + (\tilde{\mathbf{U}} \cdot \tilde{\nabla}) \tilde{\mathbf{U}} \right) = -\frac{p_0}{L_0} \cdot \tilde{\nabla} \tilde{p} + \frac{\mu_0 U_0}{L_0^2} \cdot \tilde{\nabla} \cdot \left( \tilde{\mu} (\tilde{\nabla} \tilde{\mathbf{U}} + \tilde{\nabla} \tilde{\mathbf{U}}^T) \right) + \rho_0 g_0 \cdot \tilde{\rho} \tilde{\mathbf{g}} \quad (3.4)$$

After rearrangement:

$$\tilde{\rho} \left( \frac{\partial \tilde{\mathbf{U}}}{\partial \tilde{t}} + (\tilde{\mathbf{U}} \cdot \tilde{\nabla}) \tilde{\mathbf{U}} \right) = -\frac{p_0}{\rho_0 U_0^2} \cdot \tilde{\nabla} \tilde{p} + \frac{\mu_0}{\rho_0 U_0 L_0} \cdot \tilde{\nabla} \cdot \left( \tilde{\mu} \left( \tilde{\nabla} \tilde{\mathbf{U}} + \tilde{\nabla} \tilde{\mathbf{U}}^T \right) \right) + \frac{L_0 g_0}{U_0^2} \cdot \tilde{\rho} \tilde{\mathbf{g}} \quad (3.5)$$

Then, some reference values need to be chosen:

$$t_0 = 1 \text{ s}, \quad p_0 = 1 \text{ Pa} \quad \text{and} \quad L_0 = 1 \text{ inch} = 25.4 \times 10^{-3} \text{ m}$$

The reference length is one inch since the meshes were in inches.

Next, the other reference values were defined in order to simplify quotients:

$$\rho_0 = \frac{p_0}{U_0^2} = \frac{p_0 \cdot t_0^2}{L_0^2} = 1550 \frac{\text{kg}}{\text{m}^3} \quad (3.6)$$

$$\mu_0 = \rho_0 \cdot U_0 \cdot L_0 = \frac{\rho_0 \cdot L_0^2}{t_0} = 1 \text{ Pa} \cdot \text{s} \quad (3.7)$$

$$g_0 = \frac{U_0^2}{L_0} = \frac{L_0}{t_0^2} = 25.4 \times 10^{-3} \frac{\text{m}}{\text{s}^2} \quad (3.8)$$

Finally, the dimensionless equation is obtained:

$$\tilde{\rho} \left( \frac{\partial \tilde{\mathbf{U}}}{\partial \tilde{t}} + (\tilde{\mathbf{U}} \cdot \tilde{\nabla}) \tilde{\mathbf{U}} \right) = -\tilde{\nabla} \tilde{p} + \tilde{\nabla} \cdot \left( \tilde{\mu} \left( \tilde{\nabla} \tilde{\mathbf{U}} + \tilde{\nabla} \tilde{\mathbf{U}}^T \right) \right) + \tilde{\rho} \tilde{\mathbf{g}} \quad (3.9)$$

The same procedure for removing units was used for the energy equation (2.4) without viscous heating and pressure effects:

$$\tilde{C}_p = \frac{C_p}{C_{p0}}, \quad \tilde{T} = \frac{T - T_R}{\Delta T_0} \quad \text{and} \quad \tilde{k} = \frac{k}{k_0}$$

$$\frac{\rho_0 C_{p0} \Delta T_0}{t_0} \cdot \tilde{\rho} \tilde{C}_p \left( \frac{\partial \tilde{T}}{\partial \tilde{t}} + (\tilde{\mathbf{U}} \cdot \tilde{\nabla}) \tilde{T} \right) = \frac{k_0 \Delta T_0}{L_0^2} \tilde{\nabla} \cdot (\tilde{k} \tilde{\nabla} \tilde{T}) \quad (3.10)$$

After rearrangement:

$$\tilde{\rho} \tilde{C}_p \left( \frac{\partial \tilde{T}}{\partial \tilde{t}} + (\tilde{\mathbf{U}} \cdot \tilde{\nabla}) \tilde{T} \right) = \frac{k_0}{U_0 L_0 \rho_0 C_{p0}} \tilde{\nabla} \cdot (\tilde{k} \tilde{\nabla} \tilde{T}) \quad (3.11)$$

Then, the  $C_{p0}$  reference value needs to be chosen and  $k_0$  calculated in order to remove the quotient in the hand side:

$$C_{p0} = 1000 \frac{\text{J}}{\text{kg}^\circ\text{C}}, \quad T_0 = 0 \text{ }^\circ\text{C}, \quad \text{and } \Delta T_0 = 1 \text{ }^\circ\text{C}$$

$$k_0 = U_0 L_0 \rho_0 C_{p0} = \mu_0 C_{p0} = 1000 \frac{\text{W}}{\text{m}^\circ\text{C}} \quad (3.12)$$

The convection coefficient applied to the boundary should also be dimensionless:

$$h_0 = \frac{k_0}{L_0} = 39.37 \times 10^3 \frac{\text{W}}{\text{m}^2^\circ\text{C}} \quad (3.13)$$

Finally, the dimensionless equation is obtained:

$$\tilde{\rho} \tilde{C}_p \left( \frac{\partial \tilde{T}}{\partial \tilde{t}} + (\tilde{\mathbf{U}} \cdot \tilde{\nabla}) \tilde{T} \right) = \tilde{\nabla} \cdot (\tilde{k} \tilde{\nabla} \tilde{T}) \quad (3.14)$$

The dimensionless equation of the continuity equation, after simplification with the dimensionless parameter definitions, is:

$$\tilde{\nabla} \cdot \tilde{\mathbf{U}} = 0 \quad (3.15)$$

Table 3.5 summarizes relations for all dimensionless values. These relations are needed to interpret the scale of the displayed results.

### 3.3.4 Pre-processor

The constants, boundary conditions, and simulation parameters were all defined in the pre-processor.

The density, the specific heat, the thermal conductivity, the melt temperature, the inlet pressure, the convection coefficient and the mold temperature were entered.

A forced convection was applied to the domain surface (excluding the one inch inlet canal where an isothermal boundary was imposed). The inlet was set to a normal pressure and constant melt temperature. The gravity vector was set in the negative Z direction. The non-slip condition was imposed on the wall surfaces.

The solver was set for an unsteady, convective and incompressible flow. The filling level (level-set function) was set to the mold entrance point. Variable time steps were used with the backward Euler time integration scheme.

Table 3.5 Dimensionless parameter relations for simulation.

$\tilde{\rho}$	=	$\rho [\text{kg}/\text{m}^3]$	/	$1550 [\text{kg}/\text{m}^3]$
$\tilde{U}$	=	$U [\text{m}/\text{s}]$	/	$25.4 \times 10^{-3} [\text{m}/\text{s}]$
$\tilde{t}$	=	$t [\text{s}]$	/	$1 [\text{s}]$
$\tilde{L}$	=	$L [\text{m}]$	/	$25.4 \times 10^{-3} [\text{m}]$
$\tilde{\nabla}$	=	$\nabla [1/\text{m}]$	/	$39.37 [1/\text{m}]$
$\tilde{p}$	=	$p [\text{Pa}]$	/	$1 [\text{Pa}]$
$\tilde{\mu}$	=	$\mu [\text{Pa} \cdot \text{s}]$	/	$1 [\text{Pa} \cdot \text{s}]$
$\tilde{g}$	=	$g [\text{m}/\text{s}^2]$	/	$25.4 \times 10^{-3} [\text{m}/\text{s}^2]$
$\tilde{T}$	=	$T [^\circ\text{C}]$	/	$1 [^\circ\text{C}]$
$\tilde{C}_p$	=	$C_p [\text{J}/\text{kg} \cdot ^\circ\text{C}]$	/	$1000 [\text{J}/\text{kg} \cdot ^\circ\text{C}]$
$\tilde{k}$	=	$k [\text{W}/\text{m} \cdot ^\circ\text{C}]$	/	$1000 [\text{W}/\text{m} \cdot ^\circ\text{C}]$
$\tilde{h}$	=	$h [\text{W}/\text{m}^2 \cdot ^\circ\text{C}]$	/	$39.37 \times 10^3 [\text{W}/\text{m}^2 \cdot ^\circ\text{C}]$

### 3.3.5 CFD software

As written in the previous chapter, all simulations were done using Placeview3D. This software solves the Navier-Stokes equations and energy equation with the finite element method. Linear elements for the velocity and pressure (P1-P1) are used with a Galerkin least-square (GLS) stabilization method. The P1-P1 elements satisfy the Brezzi condition (element choice for existence and uniqueness of the solution) when used with this stabilization method [44]. Custom viscosity models were integrated directly into the code, so a unique version of the program was necessary for each model.

### 3.3.6 Post-processing

Data generated by the simulation was visualized with the open-source software ParaView. The pressure and temperature curves were generated with Matlab.

### **3.3.7 Numerical plan**

All the simulation and parameters are presented in a table in Appendix 3. Two molds were simulated; the PF505171 and PF65612 (see Figure 3.1 and Figure 3.4 respectively).

## CHAPTER 4. RESULTS AND ANALYSIS

The results and analysis for experimentation, characterization and simulation are presented in this chapter. It is divided in two sections, one for the instrumented mold (PF505171) and the other for the traction bar mold (PF65612). The characterization results are included in the first section (4.1).

### 4.1 PF505171 mold

#### 4.1.1 In-cavity measurement

The data acquired with the PF505171 mold is the starting point of this work. Every simulation is validated through this experimental data. Therefore, the instrumentation and process variability needs to be taken into consideration prior to any comparison. For this purpose, a repeatability test was performed. Eight samples were injected and the results are shown in Figure 4.1. The press parameters are: an inlet pressure of  $P_l$ , a mold temperature of  $0.8 \cdot T_g$  and a melt temperature of  $1.7 \cdot T_g$  (first line of Table 3.2).

In Figure 4.1, the upper graph is the pressure as a function of time (s) and the lower graph is the temperature as a function of time (s). Both of them use the same time scale. The colors of the lines are related to the distance from the gate of the pressure transducer or thermocouple: Red, green, blue and black curves are signals from sensors located at a distance of 2 in, 3 in, 4 in and 5 in from the gate respectively. The magenta and cyan colored curves are used for sensors located in the data acquisition block upstream of the mold (see Figure 3.2). This convention will be respected throughout the document.

Figure 4.1 shows all repeatability samples plotted together. The temperatures and pressures levels are very similar. The biggest discrepancy between these samples is the time at which the pressure suddenly increases (vertical asymptote in the upper graph). This rapid increase in pressure happens when the melt front reach the end of the cavity, thus indicating the time needed to fill the mold. The filling times for this repeatability test are between 0.85 s and 1.3 s for an average of 1 s. Another difference can be observed by looking closely to the inlet pressure (magenta curves in upper graph) between 0 to 0.1 s.

During one of the test, the pressure peak does not behave like the other tests curves. The pressure suddenly reaches  $P_1$  for a short period of time and then decreases. This particular test is also the one with the highest filling time (1.3 s). This behavior might be explained by a reduced effective gate area caused by feedstock heterogeneity or a misaligned mold. The mean filling time value is 0.96 s with a 0.09 s standard deviation (9.4%) excluding the outlying test result.

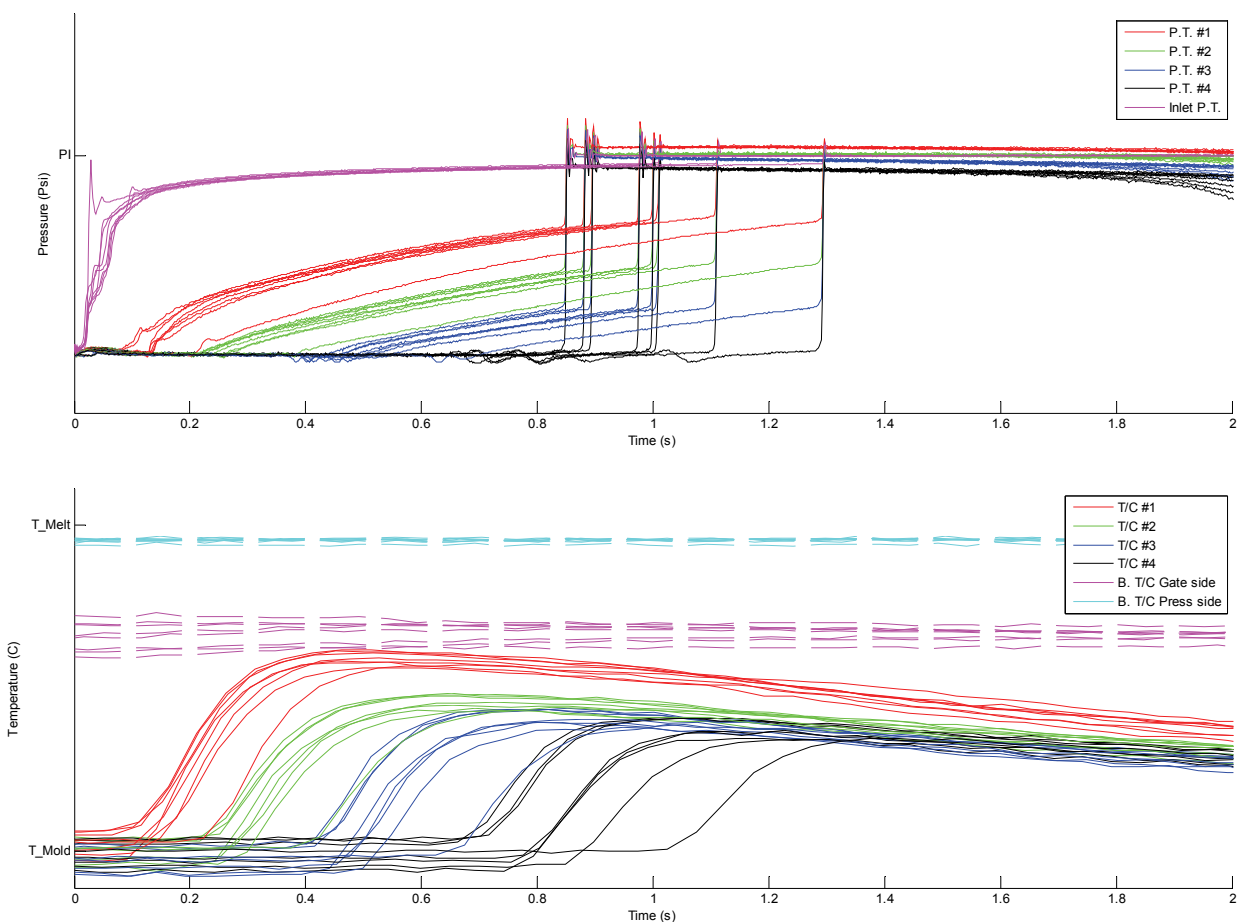


Figure 4.1 Experimental repeatability test with PF505171 mold.

To explain the filling time variability, the initial mold temperature is plotted against the filling time in Figure 4.2. Only the initial temperature of the #1 thermocouple is plotted for clarity. Excluding the sample with the initial inlet pressure peak (top right circle with a 1.3 s filling time), a tendency can be observed in the repeatability test: the filling time is inversely proportional to the initial mold temperature. This tendency is expected since the

temperature difference between the mold and feedstock controls the heat transfer rate and thus the viscosity and the pressure loss. Therefore, the filling time variability observed can be explained in part by the non-constant mold temperature.

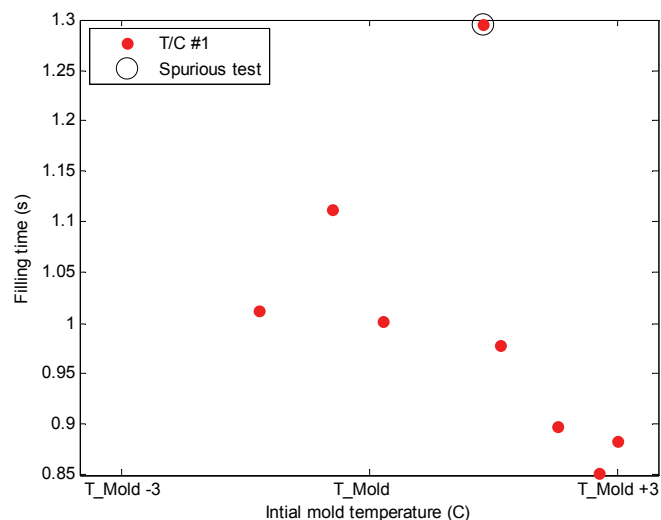


Figure 4.2 Effect of the initial mold temperature on the filling time.

To minimize the number of curves in the graphs, the sample with the filling time closest to the average will be used for numerical comparisons (see Figure 4.3). The graph can be separated in two injection regions using the terminology of reference [3]: the filling region and then the packing region. During the filling phase, the feedstock reaches the sensors and thermocouples chronologically according to their position from the gate. The pressure levels are lower than the imposed value since there is pressure loss upstream. The temperature near the gate in the data acquisition block (magenta curve in the lower graph of Figure 4.3) is lower than the melt temperature. This temperature drop is caused by the heat transfer between the acquisition block (initially at  $1.7 \cdot T_g$ ) and the mold (initially at  $0.8 \cdot T_g$ ). The other side of the block is less affected since the injection press is heated.

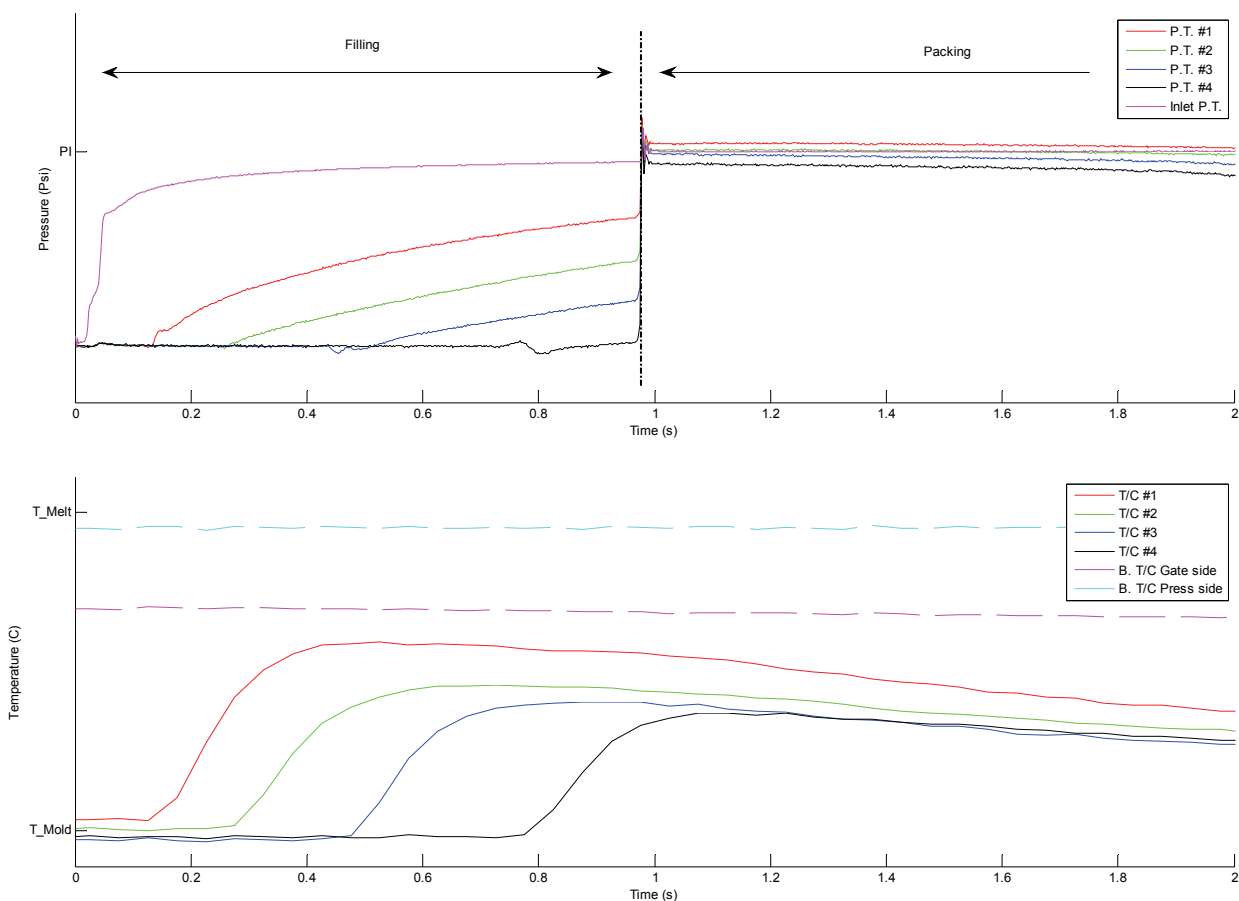


Figure 4.3 Experimental data at  $P_1$  psi,  $0.8 \cdot T_g$  mold temp and  $1.7 \cdot T_g$  melt temperature.

In addition to the repeatability test, experimental data was acquired to study the effect of pressure, the effect of mold temperature and the effect of feedstock temperature. The mean filling time and the mean maximum temperature at the first thermocouple for all the in-cavity measurements are synthesized in Table 4.1. The first part of the table (highlighted in blue) shows the pressure effect: when the imposed pressure increases, the filling time shortens and the feedstock reaches the cavity with a higher temperature. This effect is anticipated in a pressure driven flow. Note that the two lower pressures were not sufficient to fill the mold completely (the filling state is given in %). The second part of the table (highlighted in blue-gray) shows the mold temperature effect. A colder mold increases filling time and reduces the feedstock temperature faster in the cavity. Finally, the last part of the table shows the feedstock temperature effect at various pressures. A lower initial feedstock temperature increases filling time and reduces feedstock temperature inside the cavity.

Note that when the melt temperature is reduced by  $0.1 \cdot T_g$ , the temperature inside the cavity is not reduced by  $0.1 \cdot T_g$ . This is caused by the lower temperature gradient between the feedstock and the mold which reduces the heat transfer rate.

Table 4.1 Experimental results for in-cavity measurements.

Mix	Mold	Injection Parameters			Mean Filling time (s)	Mean maximum feedstock temp. at T/C #1 / $T_g$ ( $^{\circ}\text{C} / ^{\circ}\text{C}$ )
		Pressure	Feedstock Temp. / $T_g$ ( $^{\circ}\text{C} / ^{\circ}\text{C}$ )	Mold Temp. / $T_g$ ( $^{\circ}\text{C} / ^{\circ}\text{C}$ )		
PVMME-10-34	PF505171	28,6% of $P_1$	1,7	0,7	Not filled (% filled= ]54.5, 72.7[ )	1,18
		42,9% of PI			Not filled (% filled= ]72.7, 90.9[ )	1,25
		71,4% of PI			1,7385	1,32
		$P_1$			0,9626	1,33
		142,9% of PI			0,5450	1,36
		171,4% of PI			0,4055	1,37
		$P_1$	1,7	0,6	1,0526	1,31
		$P_1$		0,9	0,8884	1,36
		$P_1$	1,6	0,7	1,4095	1,27
		142,9% of PI			0,6977	1,30
		171,4% of PI			0,5045	1,32

## 4.1.2 Characterization

As mentioned in the literature review, the viscosity, the PVT, the specific heat and the thermal conductivity of the feedstock are the required properties for the simulations. This section presents the characterization results for each of these properties.

### 4.1.2.1 Viscosity

The viscosity model is built using experimental data from a AR-2000 rheometer, the Cross model, a WLF model for  $\eta_0(T)$  and an exponential model for  $\eta_{\infty}(T)$ . This model determines the viscosity at any temperature and any shear rate and is defined by equation (4.1).

$$\frac{\eta(\dot{\gamma}, T/T_g)}{\eta_{Polymers}} = 660.8 \cdot e^{(-1.646 \cdot T/T_g)} + \frac{\left( \left( 38220 \cdot e^{\left( \frac{-3084.5(T/T_g - 0.56)}{7925 + 0.02(T/T_g - 0.56)} \right)} \right) - \left( 660.8 \cdot e^{(-1.646 \cdot T/T_g)} \right) \right)}{1 + (92.43 \cdot \dot{\gamma})^{0.8851}} \quad (4.1)$$

Where  $\eta / \eta_{Polymers}$ ,  $\dot{\gamma}$  and  $T/T_g$  are respectively the normalized viscosity (relative to the mean polymer mix viscosity), the shear rate in reciprocal seconds and the feedstock temperature divided by the glass transition temperature in Celsius. Figure 4.4 shows the

fitted model with experimental data. The experimental viscosity is illustrated by the symbols and the model by the solid lines. Each color represents a temperature: Red for  $1.4 \cdot T_g$ , green for  $1.5 \cdot T_g$ , blue for  $1.6 \cdot T_g$ , magenta for  $1.7 \cdot T_g$  and cyan for  $1.8 \cdot T_g$ . Rheometer data confirms that the feedstock has a shear thinning behavior and has a Newtonian plateau at high shear rates. However, the behavior for lower shear rates ( $<10^{-1} \text{ s}^{-1}$ ) cannot be determined since no experimental data is available in that range. The feedstock viscosity could possibly exhibit a Newtonian plateau [40] or have a yield stress [27].

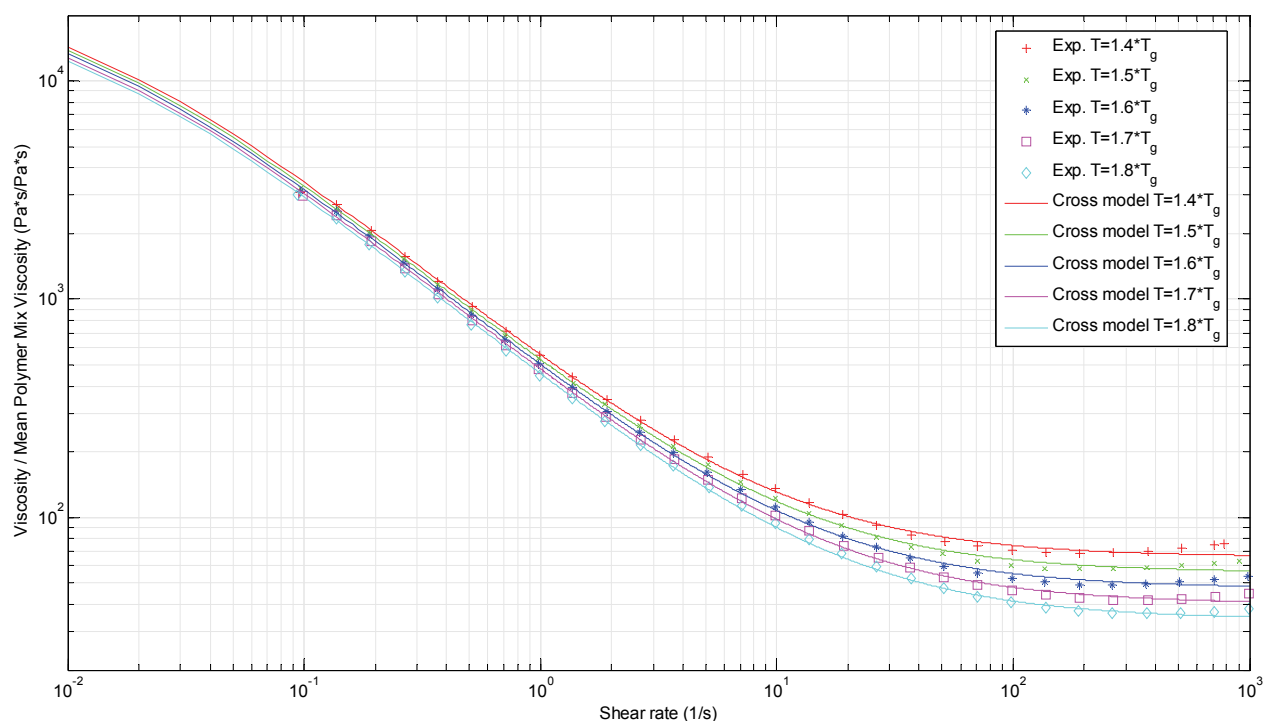


Figure 4.4 Experimental data and fitted viscosity model (AR-2000).

The model fits well the experimental data. Some minor discrepancies can still be observed in the low and high shear rate ranges. A first difference is observed at a shear rate of  $10^{-1} \text{ s}^{-1}$ , experimental data for the five temperatures are almost superposed and do not match the model. This could be explained by the precision of the rheometer at very low speed. For these tests, the angular velocity is about  $8.5 \times 10^{-3} \text{ rad/s}$ , the velocity tolerance of  $0.1 \text{ rad/s}$  is thus becoming insufficient for precise measurement. The second difference can be observed at high shear rates where the experimental viscosity is not exactly Newtonian in the final plateau; the viscosity slightly increases near the  $400 \text{ s}^{-1}$  region for every temperature. Two hypothetical causes are proposed to explain this behavior. First, the

experimental error could be higher in this region since the rheometer is very close to its maximum torque limit. Secondly, the viscosity could also be overestimated due to secondary flow generated at a higher shear rate range.

#### 4.1.2.2 PVT

Results for the feedstock density are given in Figure 4.5. The PVT result is illustrated with a blue curve.

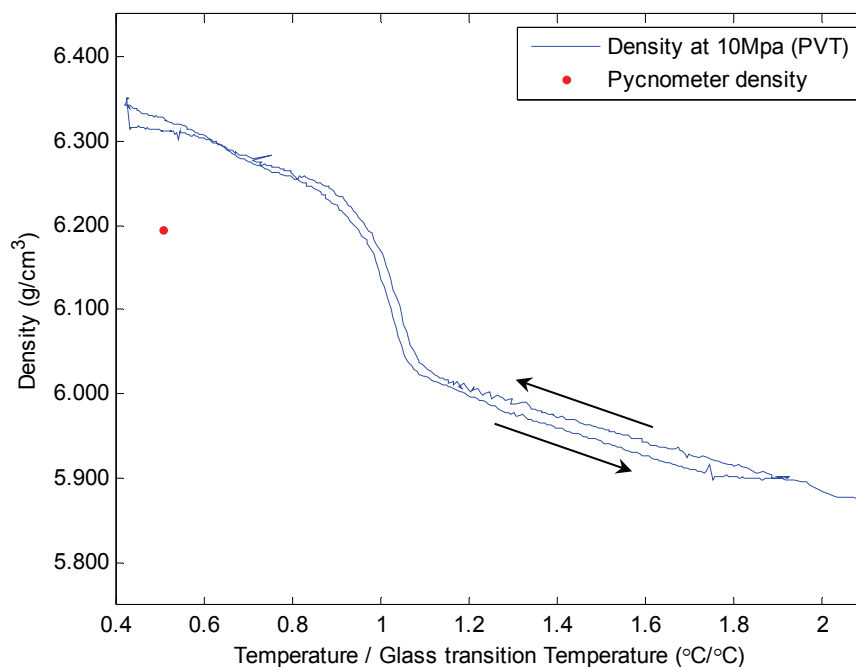


Figure 4.5 Experimental PVT and density measurement.

The pressure was set to 10 MPa (1450 psi) during this test which corresponds to the minimum pressure of the apparatus. A small hysteresis error can be observed between cooling and heating. The red dot gives the feedstock solid density at ambient temperature and atmospheric pressure: 6.1946 g/cm<sup>3</sup> with a standard deviation of 0.0021 g/cm<sup>3</sup>. Using the PVT and pycnometer results at room temperature, it can be observed that a pressure increase of 1430 psi induces a density increase of ~2.1%. In comparison with the published results [19, 45], the characterized feedstock has a higher pressure dependency. This behavior was expected since the P&WC feedstock is made with a different polymer mix. No model was fitted to the experimental data since no adequate apparatus was found to accurately define the pressure dependency in the operating range of P&WC's process. Due

to this lack of accurate data and for simplification, only the pycnometer density was used in the simulations without any temperature or pressure dependency.

#### 4.1.2.3 Specific heat

The specific heat results are shown in Figure 4.6. Four reference temperatures (heat flow set to zero) were used between  $0 \cdot T_g$  and  $2.4 \cdot T_g$ . The specific heat seems to increase slightly when the reference temperature is higher. No data were taken in the phase transition range  $\sim]0.6 \cdot T_g, 1.4 \cdot T_g[$ , but the specific heat is expected to be higher due to the latent heat. Two heating rates were tested:  $20^\circ\text{C}/\text{min}$  (blue curve) and  $10^\circ\text{C}/\text{min}$  (black dots). Contrary to the paper cited in the literature review [47], the difference in the results between these two heating rates are insignificant ( $<1\%$  in the current results opposed to  $\sim 5\%$  for Kowalski [47]). However, with the current results, no statement can be made on the behavior of the specific heat at higher heating rates. For the simulations, a value of  $0.5 \text{ J/g}\cdot^\circ\text{C}$  is a good estimation of the specific heat if a constant model is used

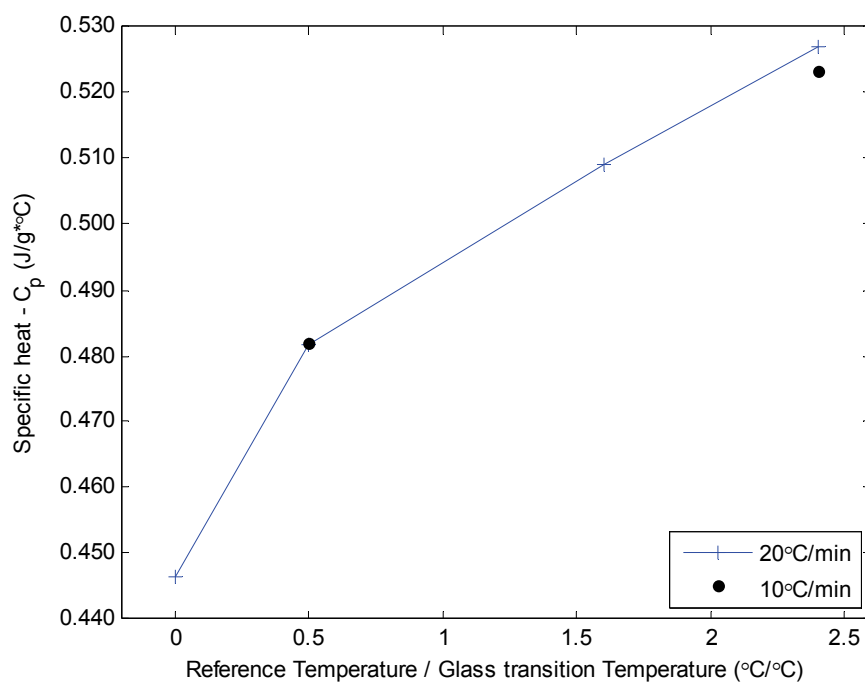


Figure 4.6 Experimental specific heat measurements.

It must be mentioned that this value was not used in every simulation since these results were only obtained near the end of the project. The first simulation calculations were

performed using an erroneous results ( $2.2 \text{ J/g}\cdot\text{°C}$ ) caused by a wrong zero flow reference temperature selection for the DSC measurement (too close to the phase change). This value is erroneous since it is equivalent to the specific heat of the polymers alone; the specific heat of a mixture should decrease when adding metallic powders. Only the values in Figure 4.6 should be used for further simulations.

#### **4.1.2.4 Thermal conductivity**

To calculate the thermal conductivity of the feedstock with equation (2.20), the thermal diffusivity results illustrated in Figure 4.7 are needed. The mean values for the five samples are represented by the blue curve. The variation between samples is relatively important (see error bars corresponding to one standard deviation). This variation could be explained by solid loading inconsistency between samples caused by segregation during the injection process. Additional tests with samples made of different solid loadings could validate this assumption.

Once again, since the thermal conductivity depends on the specific heat value which was only obtained later in the project, an erroneous thermal conductivity value without temperature dependence was used for the simulation:  $10.912 \text{ W/m}\cdot\text{°C}$ . This value was obtained by multiplying a constant thermal diffusivity of  $8 \times 10^{-7} \text{ m}^2/\text{s}$  by the pycnometer density and the erroneous specific heat. Later in this chapter, the effect of the thermal conductivity on simulations will be further discussed.

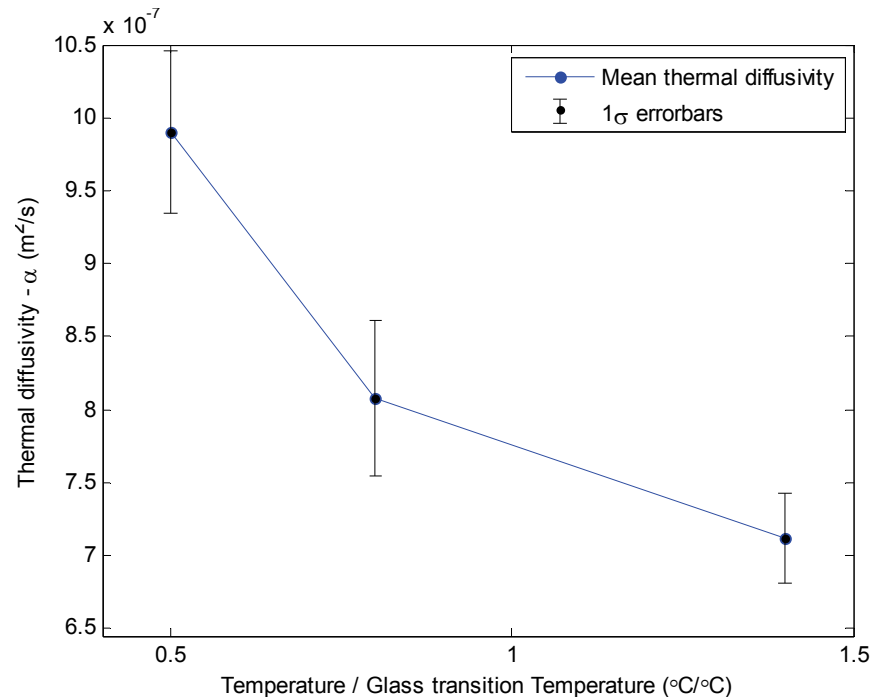


Figure 4.7 Experimental thermal diffusivity measurements.

### 4.1.3 Simulation results

#### 4.1.3.1 First trial

With the in-cavity measurements and the feedstock characterization described in the previous sub-sections, the first numerical simulation can be performed. Only one parameter was not defined experimentally; the convection coefficient ( $h$ ) on the mold walls. This parameter was estimated to be  $10\,000\text{ W/m}^2\cdot\text{°C}$  based on preliminary simulation trials and on previous internal work [31]. The simulation results are superposed on the in-cavity experimental measurements in Figure 4.8. The experimental results are illustrated by a solid line and the simulation results are illustrated by points which correspond to each solution time steps. As described previously, the pressure results are displayed on the upper part of Figure 4.8 and the temperature results in the lower part. Each color represents a different pressure transducer or thermocouple location. The parameters used for this simulation are given in Table 4.2.

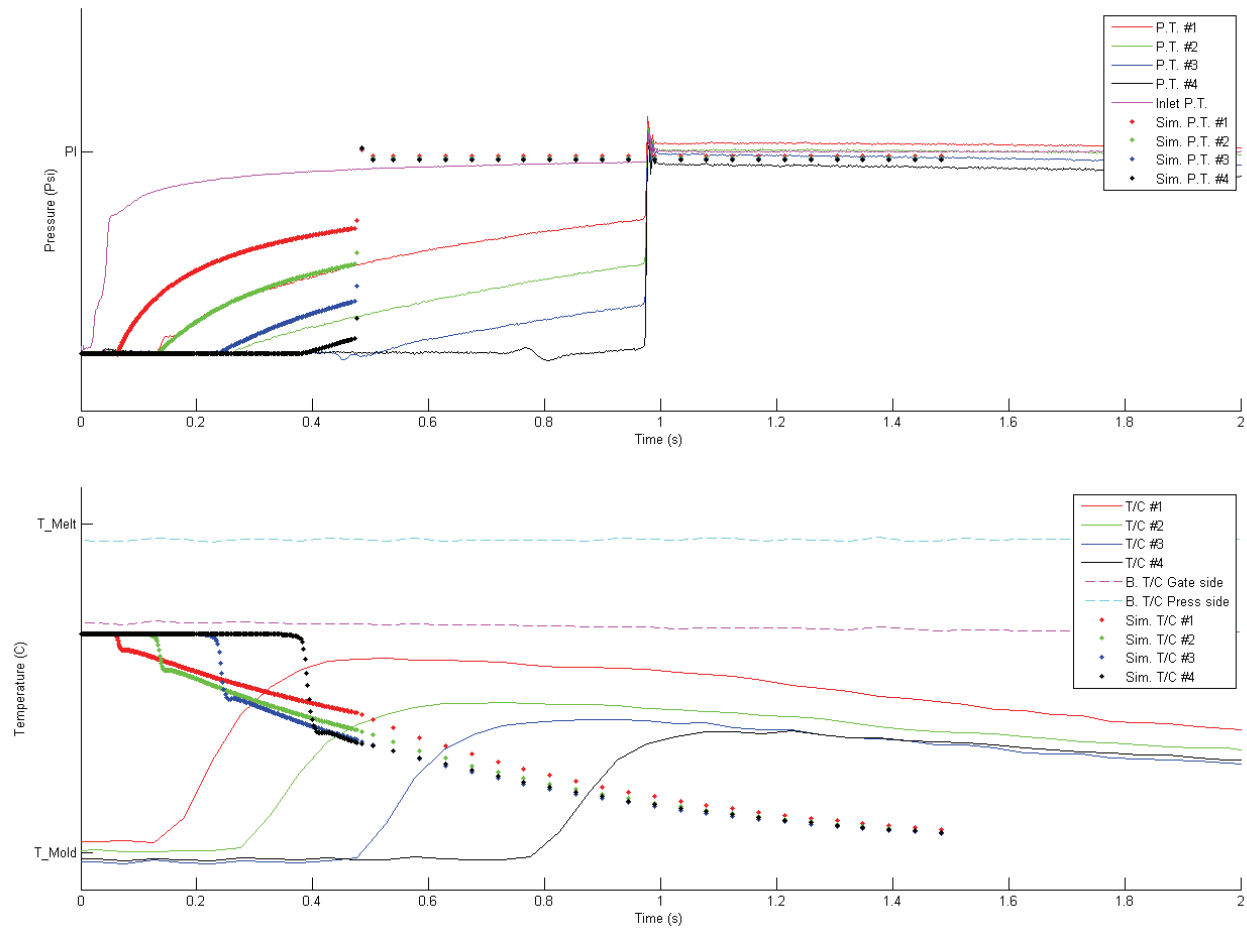


Figure 4.8 First simulation results compared with experiments.

Table 4.2 First simulation parameters.

<i>Inlet pressure</i>	=	$P_i$	[Pa]
<i>Melt Temp.</i>	=	$1.4 \cdot T_g$	[°C]
<i>Mold Temp.</i>	=	$0.7 \cdot T_g$	[°C]
<i>Density</i> ( $\rho$ )	=	6200	[kg/m <sup>3</sup> ]
<i>Specific Heat</i> ( $C_p$ )	=	0.5	[J/g · °C]
<i>Thermal Conductivity</i> ( $k$ )	=	10.912	[W/m · °C]
<i>Convection Coefficient</i> ( $h$ )	=	10000	[W/m <sup>2</sup> · °C]
<i>Gravity</i> ( $g$ )	=	9.80665	[m/s <sup>2</sup> ]
<i>Viscosity</i> ( $\mu$ or $\eta$ )	=	Equation (4.1)	[Pa · s]
<i>Number of Elements</i>	=	373228	(see Figure 3.7)

Figure 4.8 clearly demonstrates that the present simulation does not correlate with experimentation. The most noticeable discrepancy is the filling time. The simulation predicts a filling time of  $\sim 0.5$  s while the experimental filling time is  $\sim 1$  s. This means that the simulated melt front is moving too fast inside the mold cavity. Unlike conventional injection molding, where the flow rate is imposed by a moving piston, the flow rate is not controlled in the P&WC pressure-based process. Thus, the filling time only depends on the viscosity and heat transfer for a given pressure. Despite the filling time, the pressure levels seem to be reasonably accurate for all pressure transducer locations. In addition, the temperature curves do not match the experiments. Since the heat transfer is time-dependent, inaccurate results for the temperatures are expected when the filling time is underestimated. It should be mentioned that the simulated initial feedstock temperature was selected to match the thermocouple reading at the mold entrance (magenta curve in the lower figure) and not the injection press setting ( $T_{\text{Melt}}$ ) for more representative results. Furthermore, the initial air temperature inside the mold is set to the initial feedstock temperature in the program following the best practices for Plasview3D. This explains the initial plateau observed at the beginning of each simulated temperature curves. The initial plateau and the asymptotic temperature drop in the temperature curve should not be taken in consideration for comparison.

Since there are several simulation parameters and many dependent variables, more simulations are needed to explain the discrepancies between the results. In order to determine the cause of the discrepancies, the next sub-section will study the effect of some simulation parameters on the results.

#### **4.1.3.2 Sensitivity Study**

The identification of the simulation parameters that are causing the discrepancies observed in the last sub-section is challenging since many parameters are involved and are often interdependent. Evaluating independently their effect on specific results can help to understand and quantify their effect on the simulation. For this purpose, the sensitivity was calculated to quantify the dependence of results (output) based on the simulation

parameters (input) for various parameters. The sensitivity is defined by equation (4.2), found in reference [17].

$$Sensitivity = \frac{\frac{(New\ output\ value - Initial\ output\ value)}{Initial\ output\ value}}{\frac{(New\ input\ value - Initial\ input\ value)}{Initial\ input\ value}} \quad (4.2)$$

With equation (4.2) and multiple simulations, the results in Table 4.3 are obtained. The initial values were defined by a simulation with parameters shown in Table 4.2 except for a specific heat of 2.2 J/g·°C; the only value available when the sensitivity test was performed. Even if the specific heat value used for the sensitivity test is overestimated, the results were analysed assuming that this difference had little impact on the sensitivity study.

Three output results were studied: the filling time, the maximum temperature seen at the first thermocouple in the flow path and the cooling rate at the same thermocouple. Six inputs were studied:  $\rho$ ,  $C_p$ ,  $h$ ,  $k$ ,  $T\_Melt$  and  $\mu$ .

Table 4.3 Results of the numerical sensitivity study.

		Numerical Sensitivity (%)		
		Output		
		Filling time	Max feedstock Temp. at T/C #1	dT/dt at T/C #1
Input	Density $\rho$	0,03	0,00	<b>-2,20</b>
	Specific Heat $C_p$	-0,43	0,04	<b>-155,14</b>
	Convection Coefficient $h$	0,10	-0,01	<b>9,39</b>
	Thermal Conductivity $k$	0,02	0,00	0,30
	Melt Temperature $T\_Melt$	<b>-1,81</b>	<b>1,00</b>	<b>-1,44</b>
	Viscosity $\mu$	<b>1,41</b>	-0,01	<b>12,77</b>

\* Sensitivity evaluated with  $T\_Melt = 1.7 \cdot T_g$

A positive sensitivity value means that an input value increase gives an output value increase and vice versa for negative values. A high absolute sensitivity results identifies a strong dependence between the input and the output.

The results show that the initial melt temperature and the viscosity are the main driving inputs for the filling time result. One should note that these two inputs are related by the

viscosity model since it is temperature dependent; a temperature variation also causes a viscosity change. The feedstock temperature is already decreased from the injection press setting to match the temperature recorded at the mold entrance ( $T_{Melt} = 1.4 \cdot T_g$ ). A very low and unrealistic initial temperature would be needed to obtain the right filling time. Thus, the viscosity model should be the major cause explaining the non-correlated filling time between experimentation and simulation.

In regard to the maximum temperature seen at the first thermocouple, the only significant factor found is the initial melt temperature. While for the cooling rate, almost every parameter influences its behavior. However, the specific heat has the greatest influences amongst others. As mentioned previously, the heat transfer phenomenon is time dependent. Having the wrong filling time greatly influences the final results. So until the filling speed matches the experiments, efforts will first be oriented toward determination of a representative viscosity model. This decision is also supported by the fact that the MIM process at P&WC operates with a lower viscosity feedstock than the conventional process found in literature [19, 26, 27, 29, 46]. Additional precautions might be needed for rheological characterization of a lower viscosity feedstock in order to avoid phenomena such as secondary flow and segregation.

In addition to the six inputs, the effect of the mesh size was studied with a convergence analysis. The finest mesh (1 393 092 elements) decreased the filling time by 3.35% compared to the coarser mesh (267 408 elements). These results excluded the mesh size as a major discrepancy cause.

Finally, the effect of the inlet pressure is not included in the sensitivity study because the pressure levels were satisfactory in the first test results. However, the numerical simulation assumes a constant pressure for the inlet boundary condition during the entire injection cycle. Experimental results show (magenta curve in Figure 4.8) that the inlet pressure is not exactly constant at the beginning of the filling. A lower inlet pressure during the first milliseconds of the filling could also explain the smaller filling time in the numerical simulations. Consequently, following the viscosity validation, the inlet boundary condition model will be studied.

### 4.1.3.3 Viscosity model validation

To determine if the viscosity model used in the first simulation is accurate, calibrated fluid were tested in the AR-2000 rheometer. A total of three fluids with different viscosity were tested at the same temperature: R5000, R12500 and R30000 (in increasing viscosity order). The relative errors between the theoretical and experimental values were calculated with a shear rate ranging from  $10^{-2}$  to  $10^2$   $s^{-1}$ . Results are plotted in Figure 4.9.

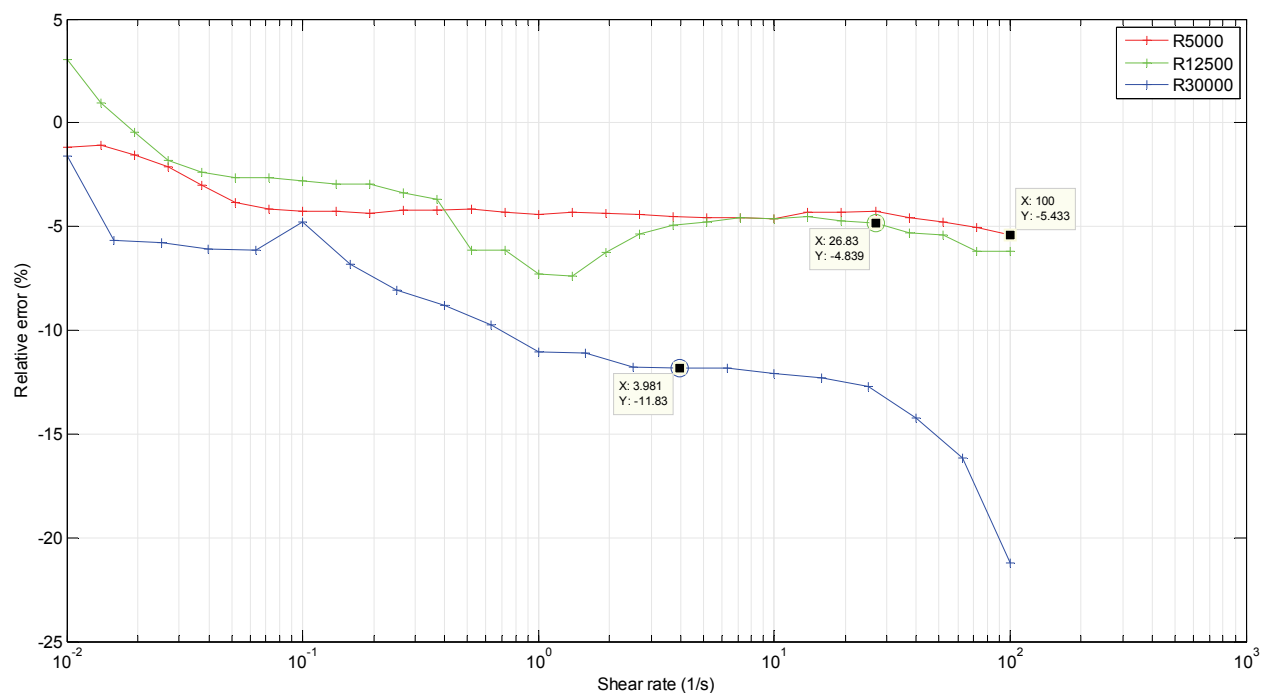


Figure 4.9 Relative viscosity error with calibrated fluid for AR-2000 at  $1.5 \cdot T_g$ .

These results show that the relative viscosity error is shear rate dependent. Therefore, the shear rate must be considered to establish the relative error for each calibrated fluid viscosity. Three representative errors are identified in the graph (data cursor). They were selected by locating the shear rates where the feedstock viscosity matches the calibrated fluid viscosity. The final errors range from -11.83 to -5.43% toward lower viscosity, meaning that the rheometer is underestimating the viscosity for the complete validation range. Yet, even with a -12% error on the viscosity, the filling time in the simulation do not increases enough to reach the experimental value of  $\sim 1$  second.

Due to the deviations observed in the measurements of the AR-2000 rheometer with calibrated fluids, a second rheometer, the Bohlin CVO-50, was used. The results are shown in Figure 4.10 with the previous model represented by thin lines.

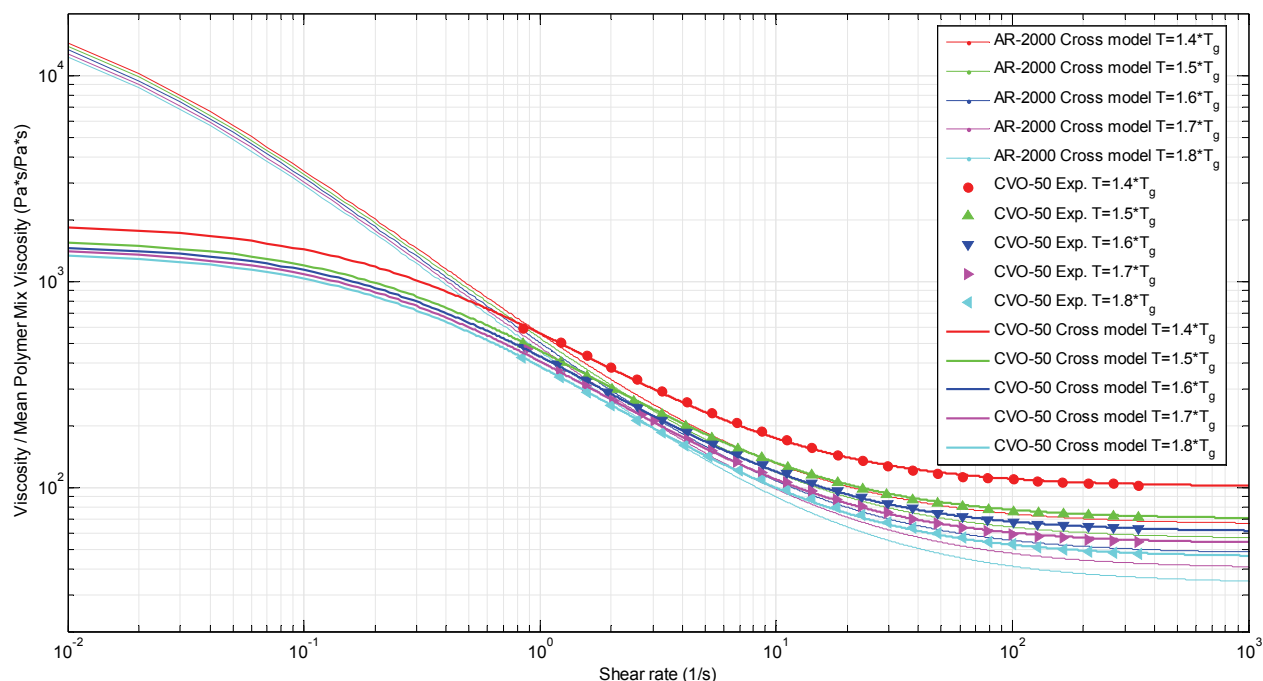


Figure 4.10 Experimental data and fitted viscosity model for the 2<sup>nd</sup> rheometer (CVO).

Two major distinctions appear between the two rheometer results. First the initial viscosity at lower shear rate ( $\eta_0$ ) is almost one order lower than the first model. This behavior cannot be confirmed since no experimental data were taken near  $10^{-1}\text{s}^{-1}$  with this rheometer; it is in the extrapolation region of the model. Furthermore, this lower viscosity at low shear rate should not increase the correlation with experimentation. It should rather decrease the filling time in the simulation by reducing pressure loss. The second distinction is the temperature dependency of the viscosity. Experimental data shows a non-linear increase in viscosity between  $1.5 \cdot T_g$  (green triangles) and  $1.4 \cdot T_g$  (red circles). This increased temperature dependency can surely increase the filling time since more pressure losses will occur in the mold during feedstock cooling.

This new viscosity model, fitted with data acquired with the CVO rheometer, was implemented in Plasview3D and the numerical simulation was repeated. The parameters used for this simulation are the same as those used in the sensitivity test except for the new

viscosity model. The simulation predicted an unfilled mold after reaching the maximum injection time of 1.5 s. A section view (y-z plane) of the simulation final time step is presented in Figure 4.11 with black dots identifying the four pressure transducer locations.



Figure 4.11 Simulation final time step result with CVO-50 viscosity model.

Figure 4.11 shows that the mold is not only unfilled, the feedstock never reached the first instrumented location after 1.5 s. The velocity magnitude (dimensionless) at this point is clearly too low to reach the end of cavity with additional time steps. Another simulation was performed with a higher melt temperature ( $T_{Melt} = 1.7 \cdot T_g$ ) and a lower convection coefficient ( $h = 4000 \text{ W/m}^2 \cdot \text{C}$ ). With these changes, the feedstock reached the first two sensor locations but never reached the end of the mold as in the experimental results. This confirms that the viscosity model has a large impact on the final simulation results.

Since simulations with the first viscosity model underestimated the filling time and simulations with the second viscosity model predicted an unfilled mold (short-shot), a final viscosity measurement was tried with a different approach; controlled shear stress mode with the SR-200 rheometer (see Figure 4.12).

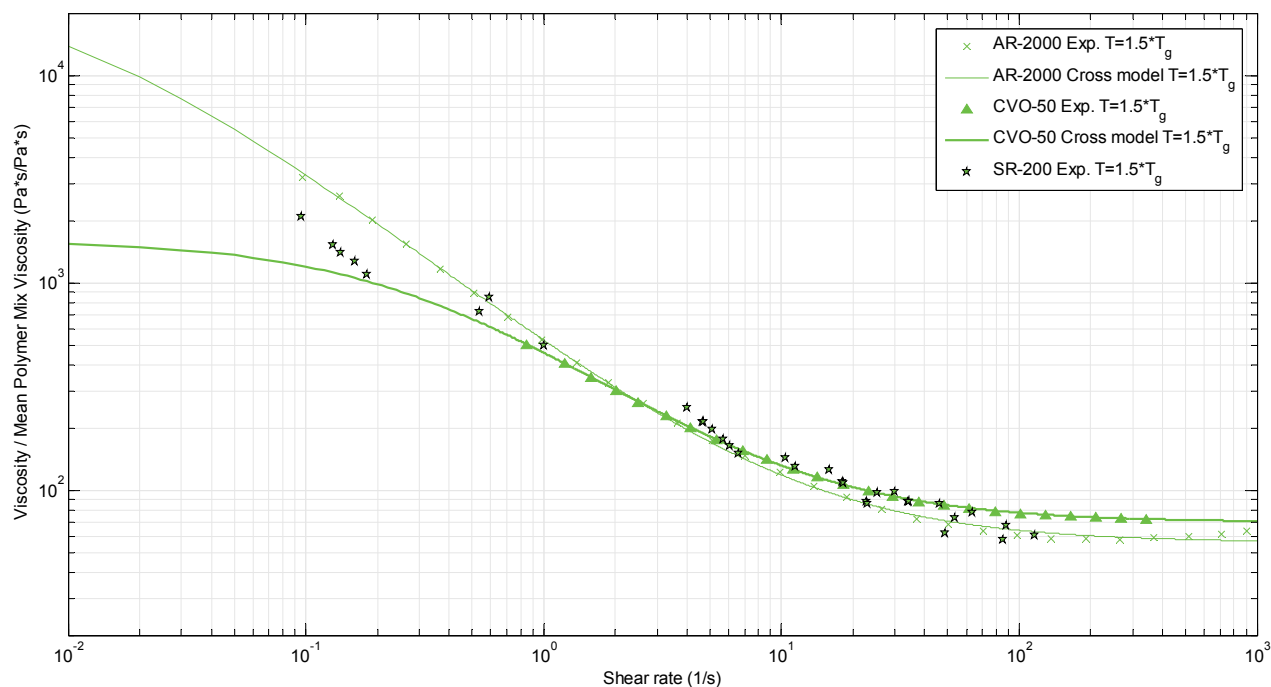


Figure 4.12 Experimental data at  $1.5 \cdot T_g$  for the third rheometer (SR-200).

As seen in Figure 4.12, the viscosity results are generally in-between the other rheometers results for a temperature of  $1.5 \cdot T_g$ . Since only one temperature was tested and because the final results are very noisy, no model was fitted for the SR-200 rheometer experimental data. However, these results reconfirm that the viscosity levels measured with the other rheometers at a temperature of  $1.5 \cdot T_g$  are correct. Assuming that the viscosity levels are accurate enough, the temperature dependencies should be the major factor explaining differences in results between the two models.

In order to compare the temperature dependencies of both models, Figure 4.13 illustrates the two temperature dependencies used in the Cross model for the AR-2000 and CVO-50 rheometers. The temperature effect used for the low shear rate viscosity ( $\eta_0(T)$ ) and for the high shear rate viscosity ( $\eta_\infty(T)$ ) are displayed respectively in the left and right parts of Figure 4.13.

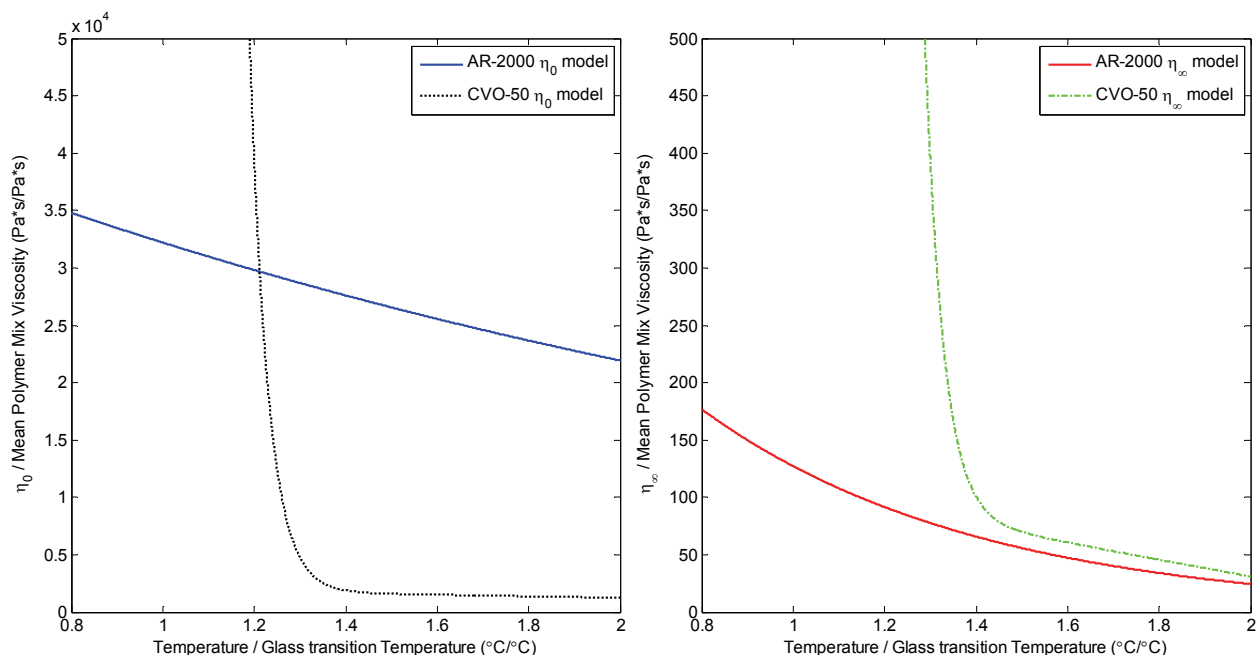


Figure 4.13 Temperature models used in the viscosity equation for both rheometers.

The differences between the AR-2000 and CVO-50 models are significant. For the  $\eta_0(T)$ , there is more than one order of magnitude difference in the viscosity at temperature lower than  $1.4 \cdot T_g$  (this difference was detected in the previous analysis). In addition, the CVO-50 model shows a rapid exponential behavior under  $1.4 \cdot T_g$  while the AR-2000 is almost linear from  $0.8 \cdot T_g$  to  $2.0 \cdot T_g$ . The rapid viscosity increase in the CVO-50 model is anticipated since the feedstock begins to solidify at low temperature (remember that the glass transition is at  $1.0 \cdot T_g$  for all graphs). For the  $\eta_{\infty}(T)$ , the level are similar over  $\sim 1.44 \cdot T_g$ , but at lower temperature they are dissimilar. Like in the  $\eta_0(T)$  relation, an exponential behavior is modeled with the CVO-50 data.

It is important to remember that no measurements were taken at temperature lower than  $1.4 \cdot T_g$ ; both models are extrapolated from higher temperature data. Thus, in order to define more accurate models, experimental data at lower temperature is needed. Still, some numerical simulations were made to determine if a change in the temperature model for the AR-2000 viscosity model can reduce the filling time. The tests were oriented toward the  $\eta_0(T)$  model since the difference between the two models was the largest. Due to time

limitation, the  $\eta_\infty(T)$  model variation effect was not studied. Figure 4.14 shows the three  $\eta_0(T)$  models tested.

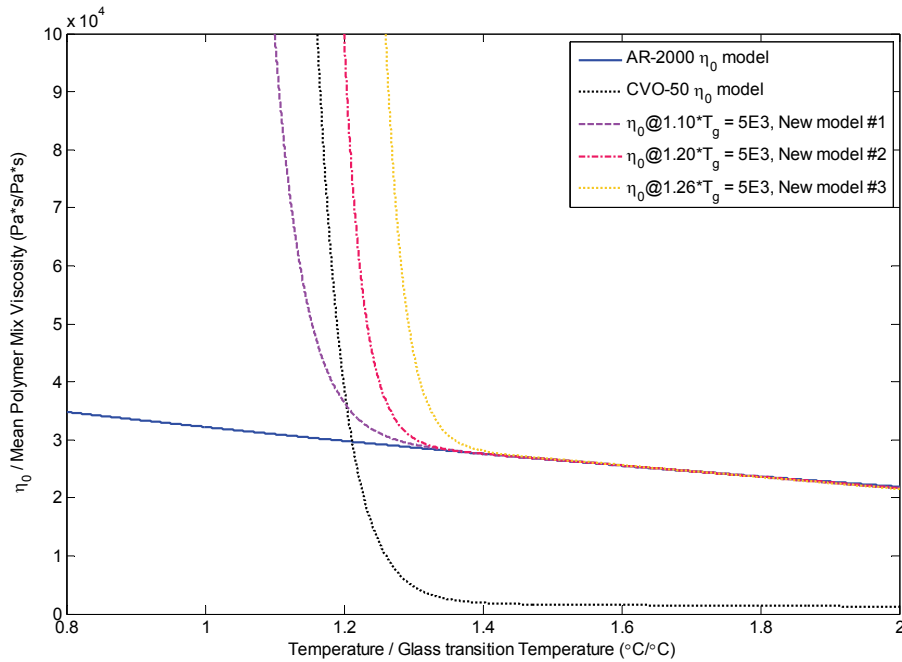


Figure 4.14 New temperature models for  $\eta_0(T)$

These models were calculated with the least square technique using a combination of a linear and exponential functions (see general equation(4.3)). The same values at lower temperature from the first AR-2000 model were used, but a new high viscosity point was added at lower temperature. This new point forced the model to exhibit the same exponential form observed in the CVO-50 model around the solidification temperature. For the first new model, a viscosity of 5000 Pa·s was imposed at  $1.10 \cdot T_g$ . For model #2 and #3, a viscosity of 5000 Pa·s was imposed at  $1.20 \cdot T_g$  and  $1.26 \cdot T_g$  respectively.

$$\eta_0(T) = b + m \cdot (T - a) + c \cdot \exp(-d \cdot (T - e)) \quad (4.3)$$

Where  $b$ ,  $m$ ,  $a$ ,  $c$ ,  $d$  and  $e$  are the fitting parameters.

These three new models of temperature were added to the viscosity model and implemented in the Plasview3D code. A simulation for each of them was performed using the parameter shown in Table 4.2 (except for the viscosity model and the convection coefficient). The simulation summary for these calculations is presented in Table 4.4. The

filling time, the relative filled volume and the short-shot time are the extracted results. The latter result is defined as the time taken to obtain the maximum relative filled volume during the simulation, i.e. time at which the feedstock velocity is null. For reference, the experimental filling time is 0.96 s (see section 4.1.1).

Looking only at the results with a convection coefficient of  $10\,000\text{ W/m}^2\text{ }^\circ\text{C}$ , the model #1 increased slightly the simulation filling time (8.67%) while the simulation with model #2 and #3 predicted an unfilled mold. Additional tests were performed with model #2 using lower convection coefficients with the aim of reducing the heat transfer at the mold walls and thus decrease the pressure loss (the convection coefficient was chosen because it is the only parameter that is not experimentally characterized). The threshold between an unfilled and a filled mold was located just over  $7\,100\text{ W/m}^2\text{ }^\circ\text{C}$  with the model #2. Nevertheless, the maximum filling time obtained is still around 0.5 s even with the new  $\eta_0(T)$  relation.

These new  $\eta_0(T)$  models increase rapidly the viscosity at lower temperature but appear to only force rapid solidification, thus inducing short-shots instead of increasing significantly the filling time. This could be explained by the shear rate level inside the cavity: if the shear rates are high during the filling, the effect of the  $\eta_0(T)$  relation is only important when the feedstock velocity is near zero and at the center line of the filling section. The rectangular geometry used in the simulation has a thin section, so it is very likely to produce high shear rates in the x-z plane. Perhaps, the  $\eta_\infty(T)$  relation has more impact on the filling time for pressure-driven flow in thin-walled geometries.

Table 4.4 Simulation results with old and new  $\eta_0(T)$  temperature models.

$\eta_0(T)$ Temperature Model	Convection Coefficient, $h$ (W/m <sup>2</sup> °C)	Filling Time (s)	% Filled	Short-shot Time (s)
AR-2000	<b>10 000</b>	0,485	100,00	NA
CVO-50	<b>10 000</b>	Unfilled	69,62	1,465
$\eta_0 @ 1.10 \cdot T_g = 5E3$ (#1)	<b>10 000</b>	0,527	100,00	NA
$\eta_0 @ 1.20 \cdot T_g = 5E3$ (#2)	1 000	0,310	100,00	NA
	7 000	0,468	100,00	NA
	7 100	0,502	100,00	NA
	7 200	Unfilled	99,71	0,542
	7 500	Unfilled	98,56	0,527
	8 000	Unfilled	96,77	0,503
	9 000	Unfilled	93,66	0,476
	<b>10 000</b>	Unfilled	90,46	0,539
$\eta_0 @ 1.26 \cdot T_g = 5E3$ (#3)	<b>10 000</b>	Unfilled	81,28	0,343

\* Simulated with  $C_p=2,2$  J/g·°C

A last test was performed to study the impact of a viscosity increase for the complete shear rate range. The entire Cross model was multiplied by a constant until the simulated filling time was near the one measured in experiments. Unfortunately, this simulation was only performed using the erroneous  $C_p$  value of 2.2 J/g·°C because the data from the new specific heat test were not available (see sub-section 4.1.2.3 for more details). Other parameters are the ones shown in Table 4.2. Simulation results were in good agreement with experimentation when the viscosity was increased by a factor of 2.5 for the complete shear rate range. Figure 4.15 shows the results obtained when using this multiplication factor.

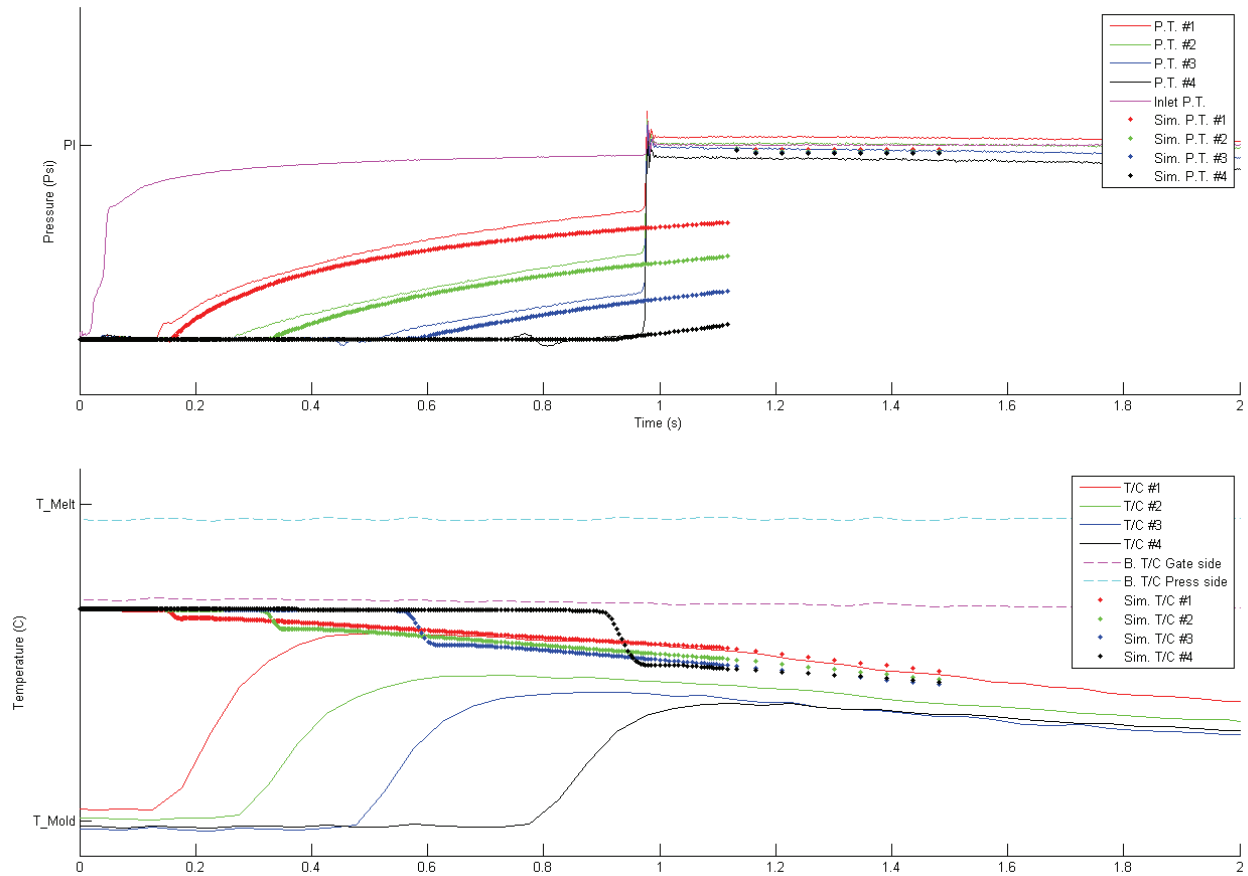


Figure 4.15 Simulation results with AR-2000 viscosity model scaled by 2.5.

The pressures curves are very close to experiments and the filling time is within two experimental standard deviations (1,117 s). The calculated temperature curves overestimate the experimental results, but this could be attributed to the usage of the erroneous higher specific heat value. Emphasis should be made on the fact that the multiplication factor was obtained by an iterative process and should not be considered as a characterization results. However, these results demonstrate that an underestimation of the viscosity could decrease the filling time in the simulation. Since no experimental viscosity data is available at lower temperature, the accuracy of the extrapolation used to define lower temperature behavior cannot be verified. A hypothesis can be made that the AR-2000 model is underestimating the viscosity at lower temperature for the complete shear rate range.

The concluding remarks for this sub-section are the following: the viscosity model has a very large impact on the simulation results and feedstock characterization should be done at lower temperature to define more accurate  $\eta_0(T)$  and  $\eta_\infty(T)$  models.

#### 4.1.3.4 Variable inlet boundary condition

The last discrepancy source identified in the sensitivity study (sub-section 4.1.3.2) is the inlet boundary condition. As mentioned previously, all the presented numerical simulations impose a constant inlet pressure during the complete injection cycle. The experimental data acquisition shows that this assumption is not exact; the inlet pressure is variable during the filling. To take into consideration this behavior, a new inlet boundary condition (B.C.) model is needed. This task was done using three steps.

The first step was the definition of the time-dependent inlet pressure relation,  $p(t)$ , based on the experimental data. As shown by Figure 4.16, the inlet pressure data from the repeatability test (see Figure 4.1) and a piecewise model was used for the  $p(t)$  relation.

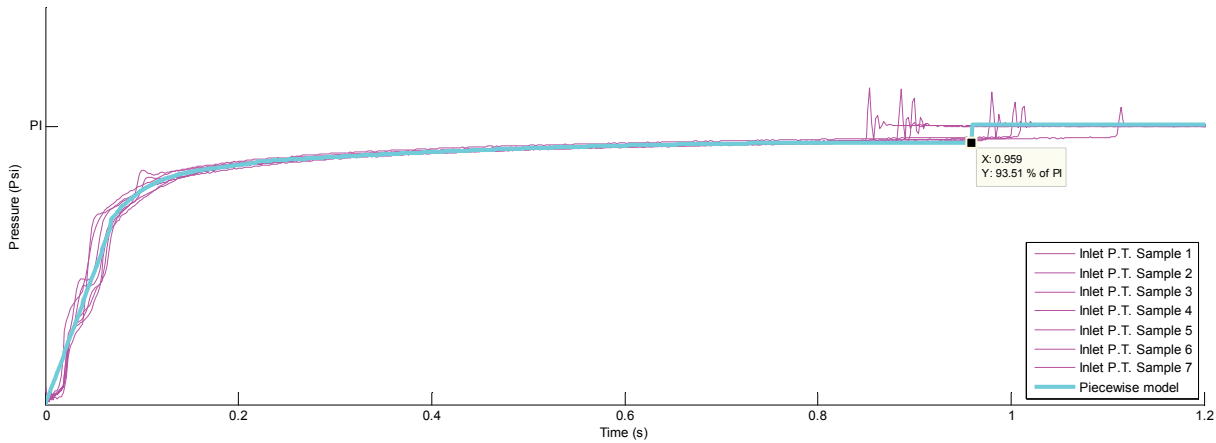


Figure 4.16 Time-dependent inlet pressure model,  $p(t)$ .

The piecewise model, obtained with the least square method, is defined by equation(4.4).

$$\frac{p(t)}{P_1} = \begin{cases} a_1 \cdot t & \text{if } 0 \leq t < t_1 \\ b_4 \cdot t^4 + b_3 \cdot t^3 + b_2 \cdot t^2 + b_1 \cdot t + b_0 & \text{if } t_1 \leq t < t_2 \\ c_3 \cdot t^3 + c_2 \cdot t^2 + c_1 \cdot t + c_0 & \text{if } t_2 \leq t < t_3 \\ d_0 & \text{if } t_3 \leq t < t_4 \\ e_0 & \text{if } t_4 \leq t \end{cases} \quad (4.4)$$

Where:

$$\begin{aligned}
 [a_1] &= [9.386] \\
 [b_4 \quad b_3 \quad b_2 \quad b_1 \quad b_0] &= [-345.6 \quad 295.6 \quad -93.63 \quad 13.49 \quad 0.09146] \\
 [c_3 \quad c_2 \quad c_1 \quad c_0] &= [1.108E-9 \quad -0.1805 \quad 0.2987 \quad 0.8115] \\
 [d_0] &= [0.9351] \\
 [e_0] &= [1] \\
 [t_1 \quad t_2 \quad t_3 \quad t_4] &= [0.06775 \quad 0.2197 \quad 0.8 \quad 0.96]
 \end{aligned}$$

Using this model is only valid for one particular injection condition since the experimental  $p(t)$  relation depends on the imposed inlet pressure. Consequently, if a different inlet pressure is studied this model is no longer valid. To obtain a model that is applicable for all pressures, another independent variable needs to be used. The second step was to find the relation between the time and the filled volume. It was done by using the simulation results that were the most similar to experiments (see Figure 4.15). The numerically predicted relation between the filled volume and the time is shown in Figure 4.17. One should note that the time was normalized by dividing it by the filling time (1.117 s). This normalization is required to define a relation that is independent of the final filling time.

The final step was to use the equation (4.4) and data from Figure 4.17 to define the normalized pressure as a function of the filled volume fraction ( $fvf$ ). A hyperbolic tangent combined with a linear function was fitted to the data with the least square method. The final equation for the inlet boundary condition is defined by equation(4.5).

$$p_{Normalize}(fvf) = (0.4279 + 0.3879 \cdot \tanh(12.69 \cdot fvf - 5.595)) + 0.2371 \cdot fvf - 0.09611 \quad (4.5)$$

Figure 4.18 shows the final model fit (blue curve) with the data extracted from the experimental acquisition and the numerical simulation (green curve). In addition, the same relation obtained with a constant inlet pressure is plotted in red for comparison. The new model reduces substantially the inlet pressure for the complete filling cycle.

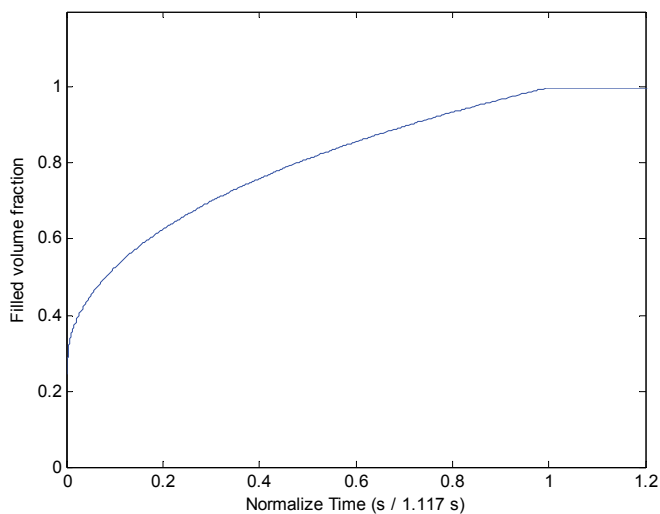


Figure 4.17 Time-dependent filled volume relation,  $f_{vf}(t)$ .

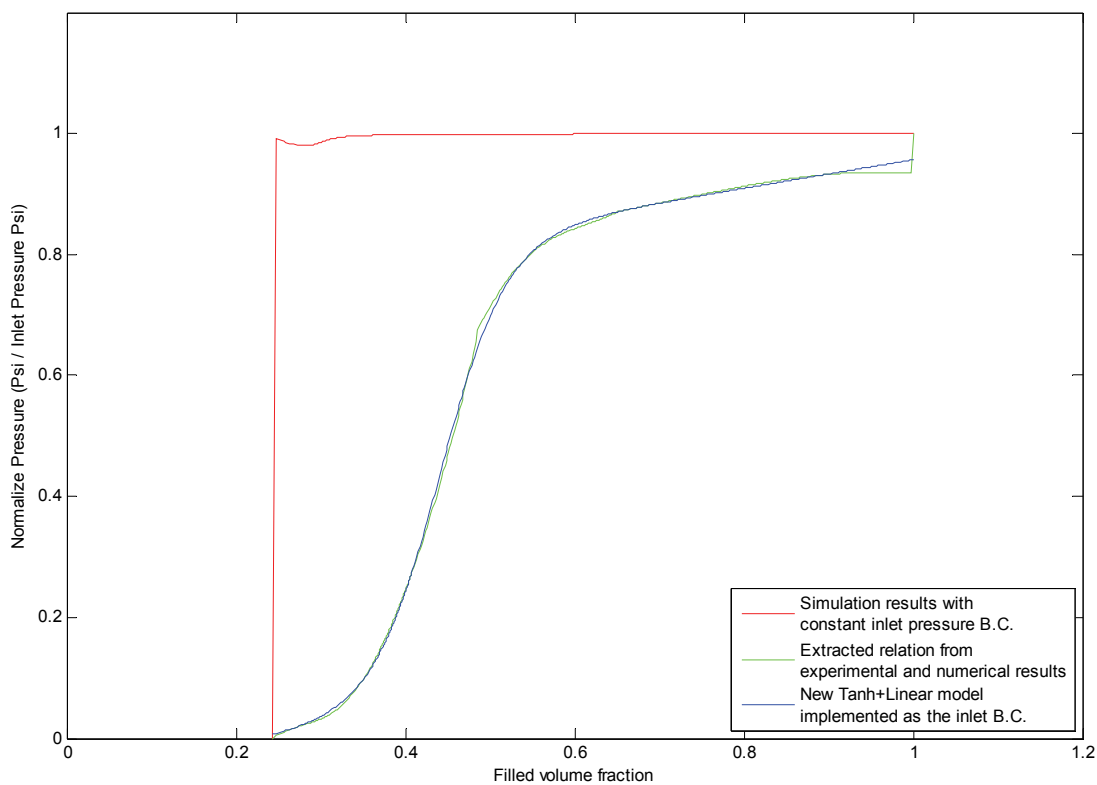


Figure 4.18 Inlet pressure model,  $p(f_{vf})$ .

This new inlet boundary condition was implemented in Plasview 3D and a simulation was performed. The parameters stated in Table 4.2 were used except for the specific heat which

was set to  $2.2 \text{ J/g}\cdot\text{°C}$  since the more accurate value was not available. Figure 4.19 shows the obtained simulation results.

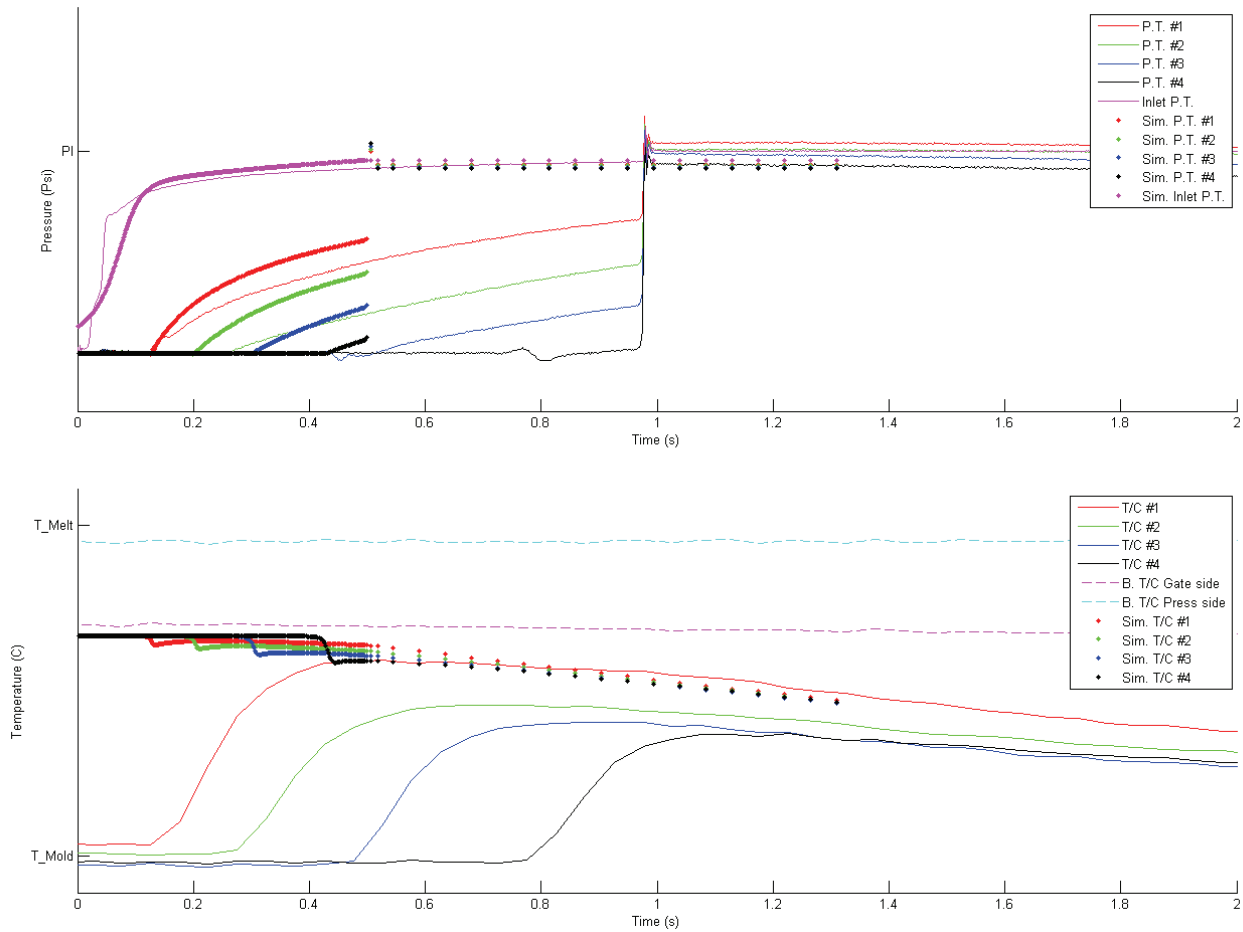


Figure 4.19 Simulation results with a variable inlet pressure condition.

A 27.4% increase in filling time was achieved with the new inlet boundary condition compared with a similar simulation with a constant inlet pressure and a specific heat of  $2.2 \text{ J/g}\cdot\text{°C}$ . However, the new model should be readjusted since the experimental and numerical results for the inlet pressure (respectively the magenta curve and the magenta dots in the upper part of Figure 4.19) do not match. The mean rate of the model should be slightly increased. Still, these results demonstrate that the constant inlet pressure assumption has a great impact on the simulation results and that a variable pressure should be considered for accurate simulation.

#### **4.1.4 Summary**

Despite many trials, no simulation matched accurately the experimental data acquired with the PF505171 mold with the currently available feedstock characterization. The viscosity model and the inlet boundary condition were identified as the most probable explanation to the non-correlation between simulations and experiments.

## 4.2 PF65612 mold

### 4.2.1 High speed camera and simulation results

The simulations with the PF505171 mold were found to be inaccurate with the experimental characterization of the feedstock. The best correlation was obtained by using a scaled viscosity model during the study of the viscosity effect (see Figure 4.15). Since the parameters used in this simulation gave the best results, the PF65612 was simulated using the same parameter except for the inlet pressure. Even if this scaled viscosity model is not proven, it can still help understanding the difference between experiments and simulations. The parameters used for this simulation are given in Table 4.5.

Table 4.5 PF65612 mold simulation parameters.

<i>Inlet pressure</i>	=	$P_T$	[Pa]
<i>Melt Temp.</i>	=	$1.4 \cdot T_g$	[°C]
<i>Mold Temp.</i>	=	$0.7 \cdot T_g$	[°C]
<i>Density</i> ( $\rho$ )	=	6200	[kg/m <sup>3</sup> ]
<i>Specific Heat</i> ( $C_p$ )	=	2.2	[J/g · °C]
<i>Thermal Conductivity</i> ( $k$ )	=	10.912	[W/m · °C]
<i>Convection Coefficient</i> ( $h$ )	=	10000	[W/m <sup>2</sup> · °C]
<i>Gravity</i> ( $g$ )	=	9.80665	[m/s <sup>2</sup> ]
<i>Viscosity</i> ( $\mu$ or $\eta$ )	=	2.5x Equation (4.1)	[Pa · s]
<i>Number of Elements</i>	=	379235	(see Figure 3.7)

The experimental recording and numerical results are illustrated in Figure 4.20 and Figure 4.21. Figure 4.20 shows the position and the shape of the melt front at a given time, while Figure 4.21 shows the shape of the melt front and the time elapsed for it to reach a given position in the cavity. The first five positions were determined arbitrarily within the mold cavity; they are illustrated in Figure 3.6. The results are labelled chronologically from “a)” to “f)”. Each view presents the high speed camera result on the left with the time displayed in milliseconds at the lower left corner and the simulation results on the right also with the time displayed in milliseconds at the lower left corner. For the simulation results, the color gradient represents the feedstock temperature. Black dots were added to identify each

predetermined positions. It should be noted that one quarter (first quarter normal to xy plane) of the geometry was removed to expose the midplane temperature. The lower cylindrical part of the simulated geometry is isothermal since it represents a heated portion of the injection press.

With these parameters, the simulated time to reach the end of the cavity is close to the experimentation: an average of 0.585 s for the experiments and 0.573 s for the simulation, a -2.89% difference. Still, large dissimilarity between experiment and simulation can be observed in Figure 4.20. For the first results, the simulated flow front position does not match the high speed camera results. The simulation overestimates the flow front speed at the beginning and underestimates it at the end of the filling, resulting in a close final time. Since the velocity of the feedstock is linked to the viscosity, this behavior can be explained by an inaccurate viscosity model. As the velocity magnitude is higher at the beginning and lower at the end of the simulation, the lower and higher shear rate range of the viscosity model could be the faulty portion (low shear viscosity overestimated and high shear rate viscosity underestimated). Figure 4.21 compares the melt front shape at determined positions. The shapes are very similar but are not produced at the same time.

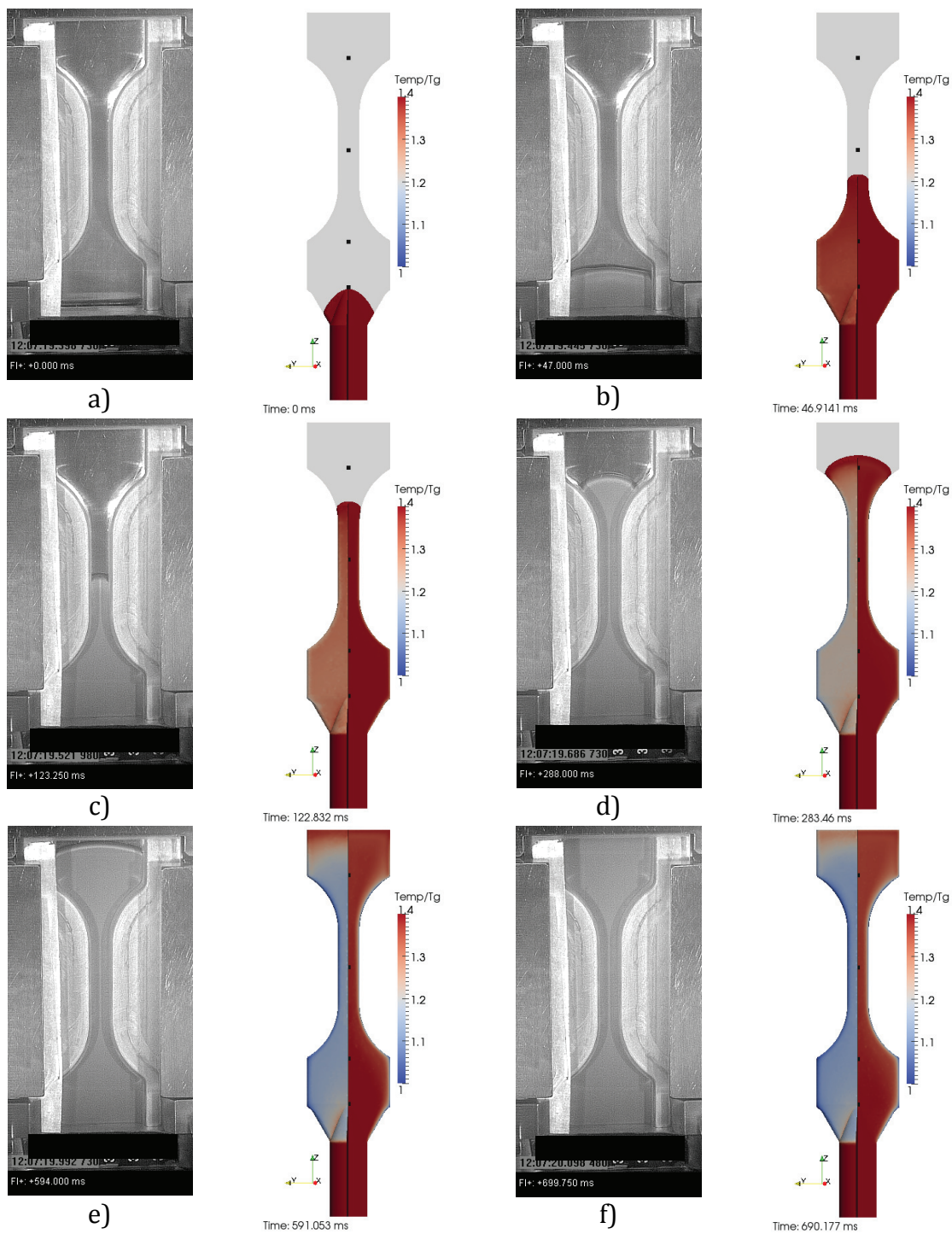


Figure 4.20 Experimental and numerical results comparison, time synchronized.

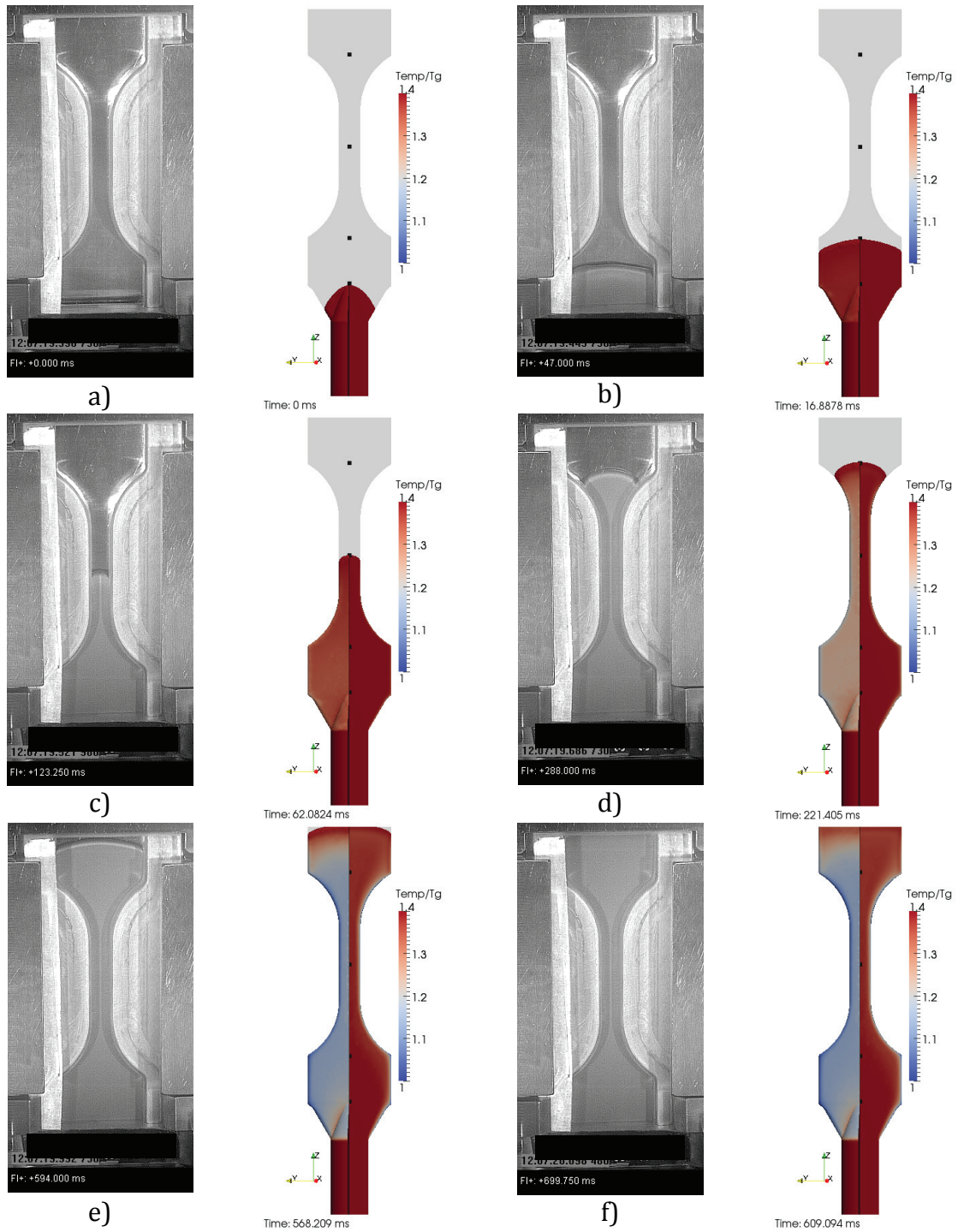


Figure 4.21 Experimental and numerical results comparison, position synchronized.

Even if the shape appears to be similar in Figure 4.21, a closer analysis near the injection start reveals that the shapes of the feedstock front are not identical for the complete cycle. Figure 4.22 shows the melt front shape for an early position.

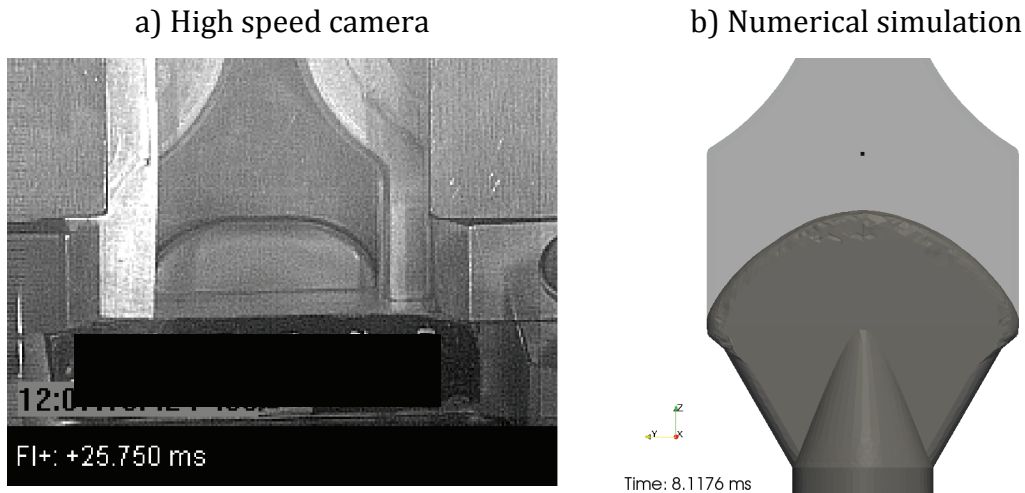


Figure 4.22 Melt front shape comparison at the beginning off the filling.

Looking at the melt front shape, the profile observed with the high speed camera is more flat than the profile predicted by the simulation at this position in the cavity. This can be explained again by an inaccurate viscosity model or an incorrect pressure profile imposed at the inlet boundary. The inlet pressure profile ( $p(t)$ ) cannot be verified since pressure data was not acquired during these tests.

The melt front position results were plotted in Figure 4.23 for an easier comparison where the horizontal axis is the time in seconds and the vertical axis is the position in inches. Experimental and simulation results are plotted respectively by the black and green curves. The standard deviations of the seven samples were added to the experimental curve. In addition, results for a colder mold (blue pluses) and for a hotter mold (red crosses) are also shown in this figure. Note that the top of the melt front was used to determine the time at which the predefined positions were reached.

Even if the time needed to reach the end of the cavity is accurate, the simulation clearly exhibits a different filling profile. Figure 4.23 also demonstrates that the repeatability or the mold temperature should not cause such a large discrepancy.

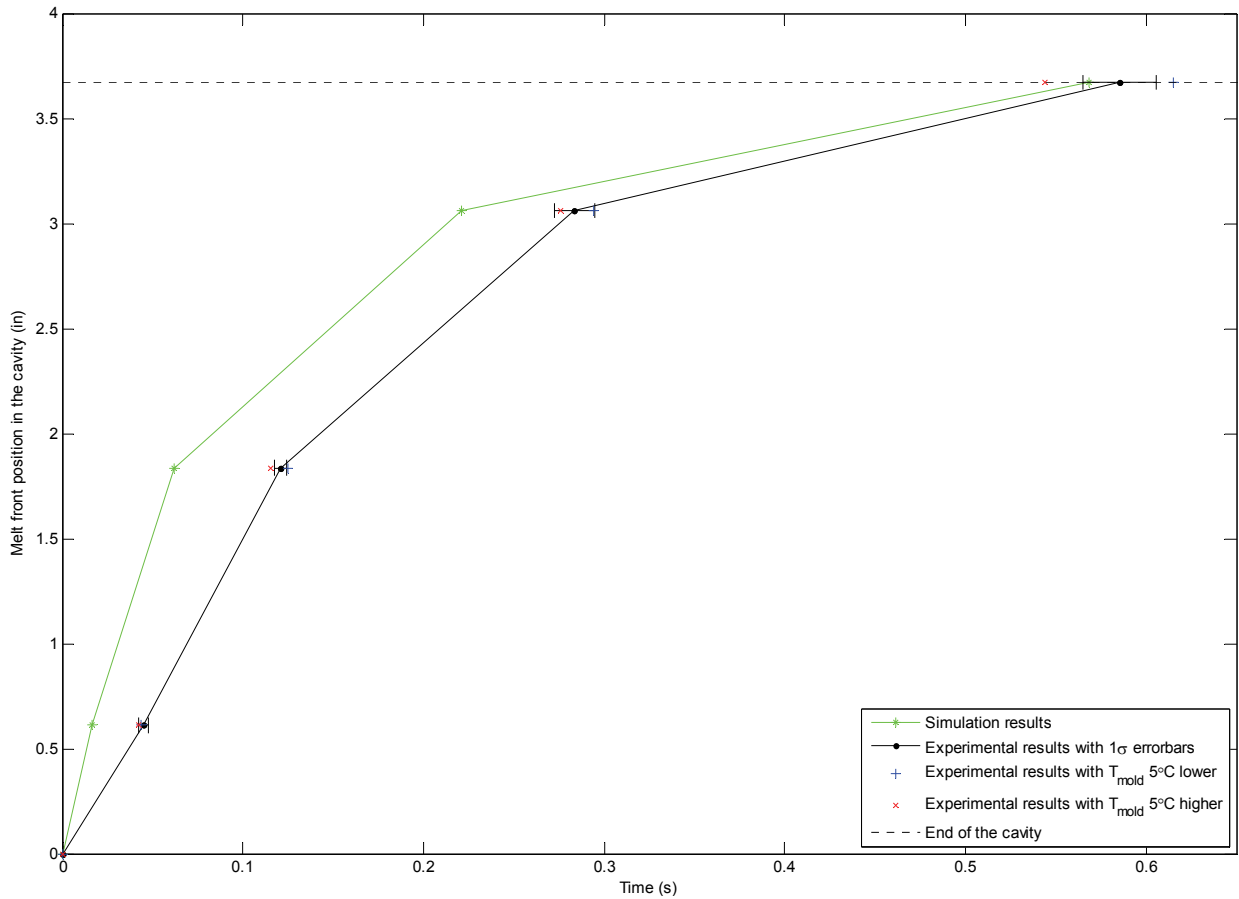


Figure 4.23 Melt front position as a function of time.

## 4.2.2 Summary

The simulation result with the PF65612 mold matched the time needed to reach the end of the cavity. However the simulation failed to predict the correct filling profile when using the parameter that gave the greatest correlation with the PF505171 mold. The viscosity model and the inlet pressure are again assumed to be the major causes of errors.

## CHAPTER 5. DISCUSSION

All the results from experimentation, characterization and simulation were presented and analysed in the previous chapter. Experimental data from two different sources (in-mold instrumentation and high speed camera) using different molds were acquired to observe the correlation with simulation. The results revealed that simulations with the presented feedstock characterization do not satisfactorily match experimentations.

Several simulations were run to explain the non-correlation. Two possible causes have been identified and studied in more detail; the viscosity model and the inlet boundary condition. The use of an artificially increased viscosity model yielded better simulation results. Still, they were not fully comparable to the in-mold measurements and high speed camera images.

Other causes could also affect the simulation results. For example, the heat transfer in the mold was not simulated in the volume of parts, only the cavity surface with heat transfer was considered. The simulation could also be affected by the use of a constant density model with no pressure or temperature dependence. Lastly, the simulation mesh could be not fine enough to catch precisely the boundary layer on the mold walls.

The next section is a discussion divided in five important points regarding the simulation: Viscosity model, inlet condition, heat transfer, characterization models and meshing of the geometry. These points of discussion were chosen because they are important factors for the simulation and the most likely sources of errors. For each of these points, the results will be explained in more details. Then, they will be compared to published results if possible and ways to improve the simulation accuracy will be proposed.

## 5.1 Viscosity model

### 5.1.1 Results summary

Although the first viscosity model used fits well the experimental data (Figure 4.4), the simulation results with that model are not accurate; the simulated filling time is half the experimental time (Figure 4.8). Since the sensitivity tests showed that the viscosity is an important factor for filling time, a validation was done to identify possible errors in this model.

Experimental data was first validated with a Newtonian calibrated fluid which revealed a maximum error of  $\sim 12\%$  which is insufficient to explain the noncorrelation. A second rheological test was performed with a different rheometer and a different geometry. This new experimental data exhibits a slightly higher viscosity level and higher temperature dependence compared to the previous data. These data points were fitted to a new model and simulated. The simulation predicted an unfilled mold. The second model is not completely different from the first one (Figure 4.10), but the differences are sufficient to switch from an overestimated flow front speed to an unfilled cavity. This result supports the hypothesis that the viscosity modeling is causing a major part of the observed differences. A third and final rheometer confirmed the viscosity level of the two previous ones. In every rheological test, the behavior at very low shear rate was not acquired because the capability limits of the rheometers were reached.

Numerical tests were also used to study the effect of the viscosity level and temperature dependencies. The first model, scaled by a 2.5 factor, yielded a filling time within the process deviation. The magnitude of the factor demonstrates that the viscosity should be substantially increased to obtain correlated data. Since the viscosity levels were verified with three different rheometers in a defined range of shear rate, steeper temperature dependence or higher viscosity in extrapolated ranges are more likely to be causing the underestimation of the overall viscosity model. To study this hypothesis, the temperature dependence at low shear rate ( $\eta_0(T)$ ) of the first viscosity model was changed for steeper models in the low temperature range where no experimental data was available. The

simulated filling time with these new modified models was not increased significantly. Instead, the simulation predicted an unfilled mold. It can be assumed that the relation at high shear rate ( $\eta_{\infty}(T)$ ) is more prone to reduce the filling time since the PF505171 mold is a thin-walled geometry which produces many high shear rate regions. Unfortunately, the second temperature dependency at higher shear rate ( $\eta_{\infty}(T)$ ) was not studied.

All these results show that a viscosity model with precise fitting at lower shear rates is needed to accurately predict the P&WC injection process. The shear rate and temperature ranges should be increased to match experimental conditions.

### 5.1.2 Literature

In comparison to published results, the viscosity of the studied process has two important distinctions. First, the process uses a lower viscosity feedstock. Secondly, the process uses a pressure-driven flow to fill the mold as opposed to controlled displacement flow found in most published works. As demonstrated previously, these two characteristics make the P&WC process very sensitive to the feedstock viscosity. Due to this greater sensitivity, the usual viscosity models and rheological methods may not be accurate enough for a representative simulation.

The shear rate range characterised in this work ( $0.1$  to  $1000 \text{ s}^{-1}$ ) is lower than many references [19, 27, 45, 46]. A final Newtonian plateau can be observed but the initial shear rate value is still not low enough to capture the behavior at very low shear rate. As an example, the current viscosity data acquired with the three different rheometers are insufficient to determine if a yield stress should be considered in the model. Adding a yield stress term in the viscosity model would change the simulated velocity profile. The profile would have a less elliptic shape with a constant velocity near the center line (plug flow region) as shown by Figure 5.1. The shape of this profile would be closer to the one observed with the high speed camera presented by Figure 4.22 a). Ilinca *et al* [22] and Thomas *et al* [26] have obtained good correlations between simulation and experimentation using a viscosity model with yield stress (Herschel-Bulkley model). Therefore this model should be considered for further work.

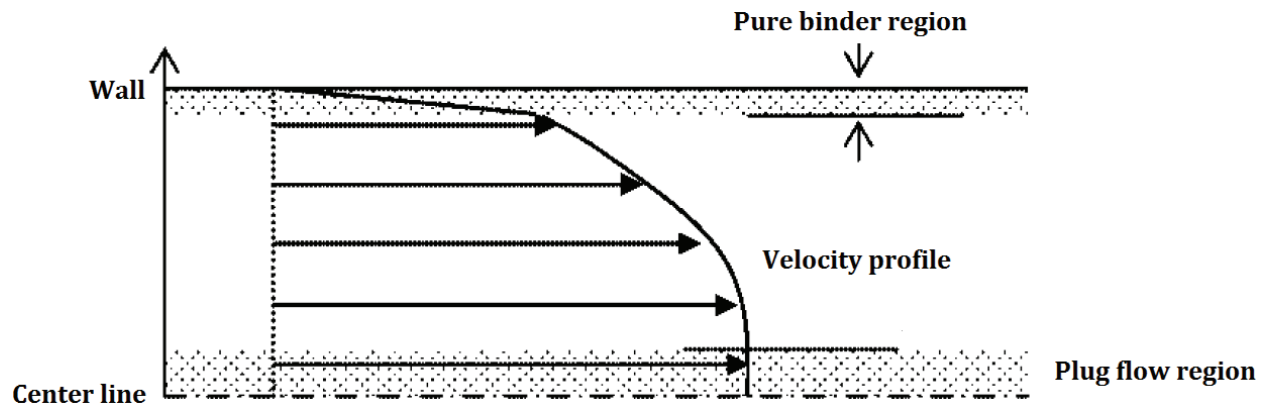


Figure 5.1 Wall slip and yield stress effect (adapted from Ahn *et al.* [19]).

Other phenomena linked to the viscosity can have an impact on the velocity profile. Authors like Hwang *et al.* [28] and Kwon *et al.* [27] recommends the use of slip velocity model or slip layer model for MIM instead of the no-slip condition used in this work. They suggest that a small pure binder region can form at the walls and act as a lubricant and insulation layer (see Figure 5.1). For the current work, it is unlikely that such model would increase the correlation with experiments since the simulated filling times are already underestimated. Using these models would rather diminish the filling time by decreasing the pressure loss and heat transfer.

Thornagel [53] reported similar conclusions about the selection of an appropriate viscosity model for MIM. This author stated that, as opposed to thermoplastic molding, the MIM process needs a more precise characterization and modeling at lower shear rate range for precise simulation. His results showed that a viscosity model with yield stress was more accurate. A good illustration from his results shows the effect of the yield stress in the viscosity model on the simulation (see Figure 5.2).

In Figure 5.2, the velocity profile with yield stress results is very similar to the velocity profile observed in this work with the high speed camera.

The shear rate is not the only dependent variable that needs a larger characterization range. The temperature range should also be increased. The five different temperatures used in this work for the temperature dependency definition are not sufficient to model the rapid increase of viscosity near the solidification. Few published results present the temperature

dependencies of MIM feedstock and no detailed methodology to obtain such dependency was found in the reviewed articles.

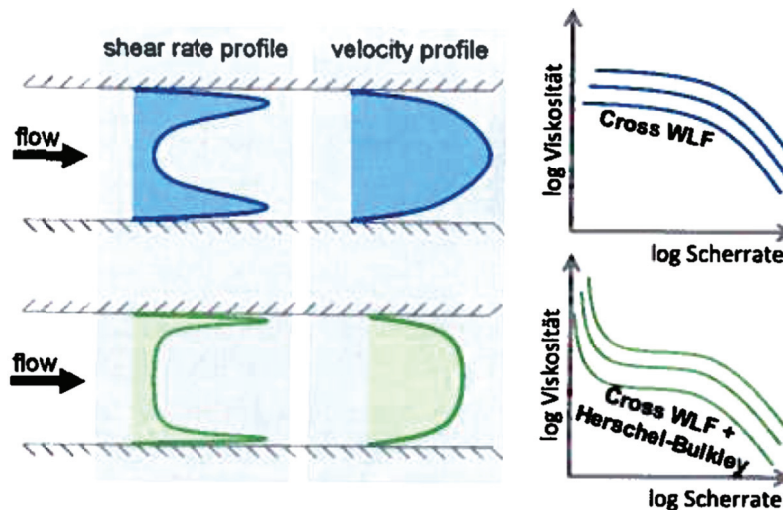


Figure 5.2 Herschel-Bulkley effect on shear rate and velocity profiles (Thornagel [53]).

The pressure is another dependent variable that might need more attention. The current results neglect the pressure effect on the viscosity, but some references state that it could have an important effect on the simulation. Pantani and Titomanlio [3] observed a better correlation with experimental results during the packing with a pressure-dependent viscosity model. According to this author, the viscosity increases with the pressure and can be modelled with a modified Cross model. This effect might be negligible for the current work since the involved pressure with conventional injection molding is orders higher than in the P&WC process. However, the polymers used for the P&WC process are not the same and could exhibit a higher pressure dependency.

Lastly, all the viscosity models used in this work are time independent (steady). The thixotropy of the feedstock was thus neglected; similar procedure was used in most published papers [19, 26, 28, 29]. Work done by Torkar *et al.* [54], however, showed that the thixotropy must be included in the viscosity model to match the flow behavior of alumina-paraffin suspensions. In their work, the thixotropy was observed with a hysteresis loop (continuous viscosity measurement from low to high shear rate and then back to low shear rate). If the up and down viscosity curves diverge, there is thixotropy. A strong

thixotropy could explain the underestimation of the viscosity revealed by the simulation. The hysteresis loop test on P&WC's feedstock is required to determine if the thixotropy must be included or not in the viscosity model.

### **5.1.3 Improvements suggestions**

The presented viscosity characterization and model can be improved in several ways. First the rheological test should be performed at lower shear rate range to avoid modeling errors. For this purpose new apparatus should be selected as the presented rheometer are not suitable for testing P&WC's feedstock at very low shear rate. If a rotational rheometer is selected, a particular attention should be given to the minimum angular velocity and the precision of the controller.

Secondly, the effect of the pressure on the viscosity should be studied within the pressure range of the process. This would permit to determine if a pressure-dependency model is needed or not.

Thirdly, the temperature dependency should be characterized from solidification (as close as possible) up to the maximum process temperature. During this work, some viscosity measurements were made at lower temperature, but the results were not repeatable and unstable close to the solidification temperature. The methodology would need some modification in order to reach lower temperatures.

Fourthly, the thixotropy should be studied to determine if the rheological methodology used is representative of P&WC's MIM process. The injection cycle lasts less than a second for the studied molds while the rheological measurement takes about one and a half minute. If there is a strong thixotropy, reducing the test duration could result in large variation in the viscosity measurement.

Finally, a special geometry for rotational rheometer could be built to reduce the segregation during measurement. The vane tool was chosen to avoid segregation but repetitive tests with the same sample showed that the segregation was not completely avoided since the viscosity was decreasing for each new test. A custom helicoid geometry could reduce the gravitational segregation.

## 5.2 Inlet condition

The inlet condition is another aspect that needs further explanation and discussion. This sub-chapter is a discussion about the inlet modeling.

### 5.2.1 Results summary

First, the experimental data shows that the inlet pressure is not constant during the injection cycle (see Figure 4.16). Since the pressure is imposed upstream in the injection press, some pressure losses occur in the injection channel before the mold entrance. Consequently, during the filling the inlet pressure varies from zero to the imposed pressure minus the pressure loss. This pressure loss depends on many factors like the velocity, the density, the viscosity and the cavity shape. For the PF505171 mold, even if the section is constant, the measured pressure at the inlet tends towards, but never reaches a constant value. A small evolution is still noticeable since the feedstock is cooling down and thus the feedstock viscosity is still changing. In other words, a steady-state is never reached during the filling due to the non-isothermal flow.

For the simulation, this inlet pressure variation was first neglected. Most simulations in this work assume a constant inlet pressure. Thus, this assumption overestimates the pressure levels during the cavity filling since the pressure loss upstream is neglected. This was proven by implementing an inlet pressure model closer to the experimental observations. Simulations with the new model produced a 27.4% increase in filling time, which is significant. This new implemented model is based on the experimental pressure data acquired with the PF505171 mold. Therefore, making the usage of such a model is impossible for an untested mold or numerical three-dimensional model.

As stated previously, a pressure was imposed at the inlet of the mold for all simulations. However, it should be mentioned that this condition is not imposed directly to every nodes on the inlet surface. Due to the finite element discretization method, the pressure at the inlet is imposed in an integral form (weakly imposed). The use of a Dirichlet boundary condition for the complete inlet surface would violates the continuity equation (2.3). The only way to respect the continuity equation and impose a surface pressure is to use a

natural condition. Consequently, the integral of the pressure on the surface respects the imposed pressure, not every discretized point. A more detailed discussion about the imposition of a pressure on a surface with FEM can be found in Fortin's book [6].

Simulation results confirmed that the integral of the pressure on the inlet surface respect well the imposed pressure during filling. For example, the integral of the inlet pressure for a typical simulation with the PF505171 returned a maximum error of only 1.1% as shown by point 2 of Figure 5.3.

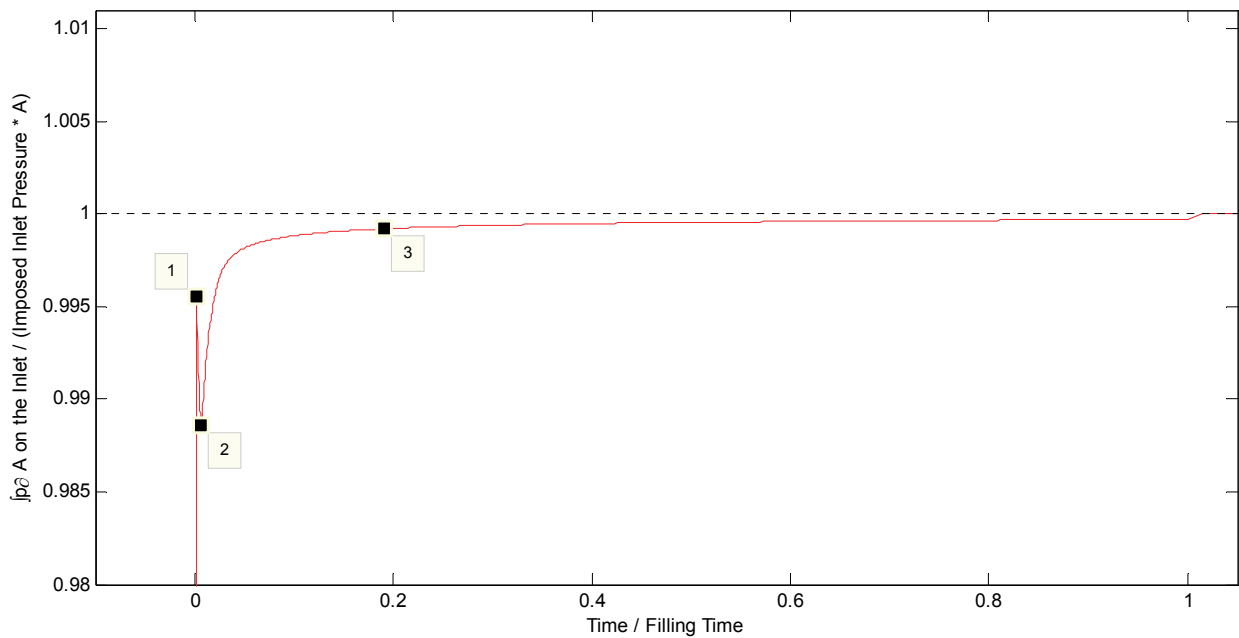


Figure 5.3 Integral of the inlet pressure boundary condition as a function of time.

However, since the pressure is not imposed at every discretized point on the inlet surface, the pressure can still vary and respect the integral condition. Three time steps (labeled from 1 to 3) were chosen in Figure 5.3 to study the pressure variation on the inlet surface. For each time step, the pressure divided by the imposed pressure on the inlet surface is plotted in Figure 5.4. The maximum deviation from the imposed pressure is about 10% located on the surface frontier of the second labeled time step. This deviation can only be found at the beginning of the simulation and occurs only for a short period of time. For most of the simulation, the pressure deviation for every node on the inlet surface is within 1% from the imposed one. Thus, this deviation is considered negligible and it should not reduce the simulation quality.

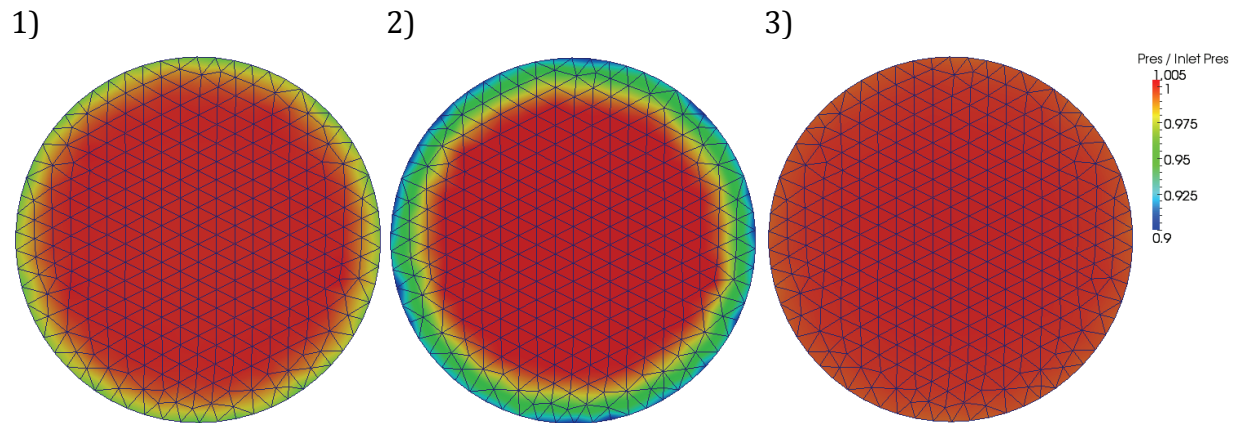


Figure 5.4 Pressure variation on the inlet surface at various time steps.

### 5.2.2 Literature

Most published results use a velocity rather than a pressure for the inlet boundary condition (e.g. articles [9, 19, 25, 26, 28, 55]). This is explained by a majority of injection press using a displacement controlled screw to fill the cavity. As opposed to the P&WC process, the inlet velocity is thus known and precisely controllable. A general review by Kim and Turng [56] stated that velocity or pressure have been used for the inlet condition, but no simulation results using a pressure inlet condition for MIM were found in published results.

Even if a velocity could be acquired at the mold entrance and imposed in the simulation like in literature, this different boundary condition would not be useful since the P&WC process is controlled by an imposed pressure. In fact, the velocity in this process is a dependent variable and thus varies as a function of the pressure, temperature, viscosity, cavity geometry and other factors. Consequently, experimental data would still be needed for every injection condition to obtain accurate simulation with inlet velocity condition.

### 5.2.3 Improvements suggestions

Regardless of imposed velocity or pressure, an accurate simulation must use an independent variable for the inlet boundary condition. In the current work, the simulation pressure was imposed near the entry of the mold. Since the pressure is not controlled at this specific point, variable pressure losses occur upstream and decrease the simulation

accuracy. So, the imposed condition is not completely independent of the flow characteristics and experimental data is needed to impose the right inlet condition. The simulation should be a design tool rather than a validation tool; models based on inlet cavity measurement should be avoided.

This problem would be eliminated if the simulation took into account every geometric feature between the imposed pressure and the mold cavity. Obviously to simulate all these features, a fair amount of additional computational resources would be needed to solve the large number of elements of the increased domain. Since the inlet condition is experimentally known for the current molds, efforts should be first put on increasing the accuracy of the viscosity model to avoid the need for additional computational resources. The acquisition of the velocity inlet in parallel with the inlet pressure data could also help validate the simulation without simulating the complete press geometry. To obtain an accurate inlet condition with a new mold, experimental data or complete simulation of the injection press would still be needed.

## 5.3 Heat transfer

The third aspect is the heat transfer between feedstock and mold. It will be discussed in the following sub-chapter.

### 5.3.1 Results summary

Six thermocouples installed on the PF505171 mold gave the temperature evolution inside the cavity. Moving average filtering with large subsets was necessary to remove noise peaks in the data. The experimental data showed that the initial mold temperature has a great impact on the filling time; ~15 % for a 3°C deviation (see Figure 4.2). Characterization of the feedstock revealed a specific heat of 0.5 J/g·°C and a thermal conductivity of 10.912 W/m·°C (based on the thermal diffusivity). A convection coefficient on the mold walls of 10 000 W/m<sup>2</sup>·°C was used. Since this coefficient cannot be directly measured, it was determined by matching the cooling rate in the temperature curves with numerical iterations.

The external geometries of the mold and the wall thickness variations were not modeled. Instead, the simulations used a constant convection coefficient on the mold cavity walls to model every heat transfer phenomena between the feedstock and the mold. It's important to note that for the simulations with the PF65612 (traction bar mold), the heat properties of the polycarbonate plate used for visualization with the high speed camera was neglected. In addition, the temperature of air inside the cavity was set equal to the feedstock melt temperature for the complete cycle. This last condition causes an overestimation of the feedstock front temperature; at the interface between feedstock and air, at some point the air is hotter and increases slightly the feedstock temperature. An example of the simulation results with the PF505171 mold is given by Figure 5.5. In this figure, the temperature was normalized by subtracting the numerical temperature to the inlet feedstock melt temperature. Thus, a higher normalized value (represented by the blue color in Figure 5.5) yields a colder temperature. Note that the geometry was cut through the middle plane (normal to the y direction) to expose the temperatures inside the cavity.

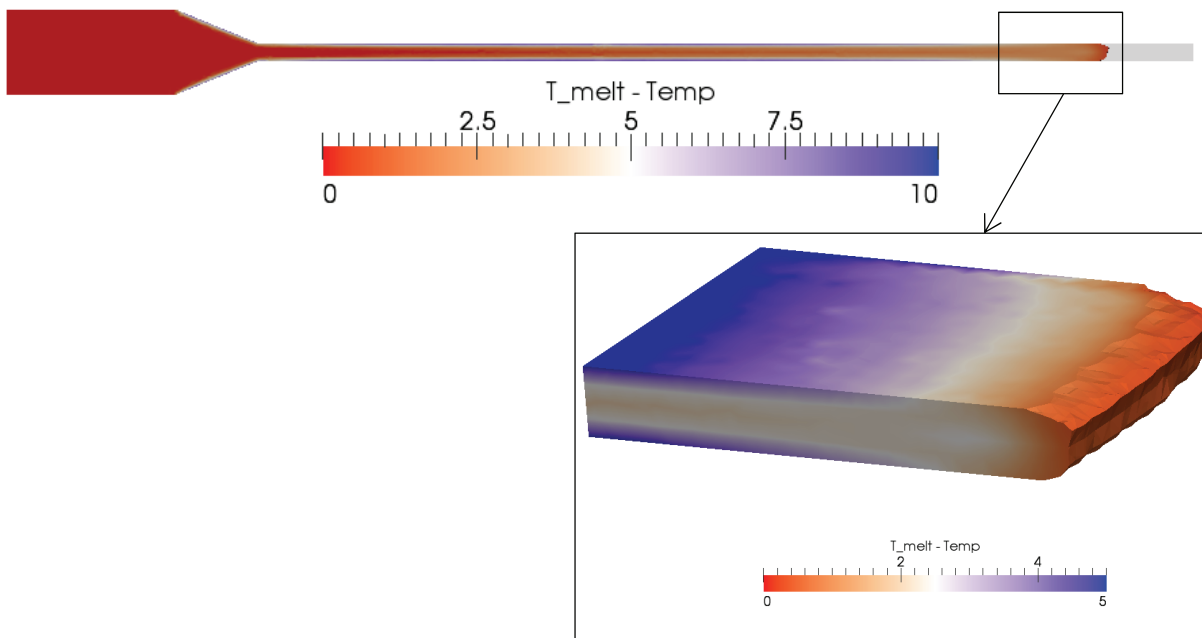


Figure 5.5 Normalized temperature distribution at the middle plane.

The effect of convection coefficient applied to the mold walls is observable through the strong temperature gradient at the surfaces. Looking carefully at the end of the filled geometry, the small temperature increase discussed previously can be seen. This temperature increase could underestimate the viscosity of the melt front and thus the filling time. No tests were made to study the impact of the air temperature during the simulation.

Lastly, a sensitivity study showed (see Table 4.3) that the feedstock specific heat is the simulation parameter that has the greatest impact on the cooling rate. Unsurprisingly, the viscosity and convection coefficient are also non-negligible parameters for accurate temperature curves.

### 5.3.2 Literature

Very little details are given in literature regarding the value of the convection coefficient. A wide range have been used; values of 1 000, 4 000 and 100 000  $\text{W}/\text{m}^2\cdot^\circ\text{C}$  were used in the work of Ilinca and Héту [3, 22, 57]. In addition, no detailed methodology to obtain an accurate convection coefficient was found in the literature. The estimated value of 10 000  $\text{W}/\text{m}^2\cdot^\circ\text{C}$  found in this work is within the range of typical simulation and is close to the value obtained in previous work done by Turenne on the P&WC process [30].

In the work of Pantani and Titomanlio [3], a time dependent model for the convection coefficient is proposed instead of a constant value. The purpose of the model is to take into account the evolution of the thermal contact resistant inside the mold. A gap between the feedstock and the mold wall caused by the thermal contraction can greatly reduce the convection coefficient during the simulation. Such model is valid for the cooling state; it is unlikely that this model would have a significant impact for the filling phase since the injection pressure forces the contact between the feedstock and the walls. Furthermore, the reduction of the convention coefficient as a function of time would yield lower temperature losses, and thus decrease the already underestimated filling time.

It's interesting to note that in the consulted and published results, none of the simulations included the mold geometry. Haagh *et al.* [58] stated that for gas-assisted injection, including the mold geometry in the simulation would yield better result. However, the impact of neglecting or not the mold geometry for MIM was not studied in all the consulted papers. A complete thermal analysis would be challenging for the current work because molds used have no cooling channels for temperature control. They are made with multiple parts which cause many thermal contact resistances; natural convection and conduction need to be considered in the analysis and the experimental temperature distribution of the mold have never been characterized.

The influence of the polycarbonate window on the experimental results with the PF65612 mold is unknown. Most injection process uses higher pressure and select quartz to make parts for inside-cavity visualization. Yokoi [3], based on experimentations, stated that for plastic injection at specific parameters, the filling pattern is slightly affected by the glass windows. He also mentioned that using glass windows during cooling is inappropriate since the thermal properties of the steel and glass are very different. For the current work, no visual indications were found when comparing the steel part side and the polycarbonate part side in the high speed videos. It is expected that the feedstock in contact with the polycarbonate part side have a slightly higher temperature due to the lower thermal conductivity of the polycarbonate.

### 5.3.3 Improvements suggestions

To improve the accuracy of the experimental data, some points can be proposed. First, usage of smaller diameter thermocouples would help minimize the response time. Even if the thermocouple of the instrumented mold were only 1/16" in diameter, smaller thermocouples would still decrease the thermal inertia and give more accurate data for rapid temperature variation measurements. Secondly, reducing the number of junctions in the thermocouple wire or selection of a data acquisition system with more precision would help reduce the size of the oversampling noise reduction technique. Though, the current data are considered suitable for further simulation development without any accuracy increase. Thirdly, using a temperature-controlled mold would help increase the repeatability of the experiment and help finding a representative convection coefficient. Lastly, the influence of the polycarbonate could be quantified for various outputs by comparing the filling behavior with one, two and no polycarbonate parts. This would determine whether the material has a negligible impact or not.

For simulation, the heat transfer at the interface between feedstock and air should be studied. Various air temperatures should be simulated to remove or not this phenomenon from possible source of error. Next, the complete mold geometry and external conditions could be simulated. To achieve this, experimental temperature acquisition on the mold would be needed to characterize the external convection coefficient and heat flux generated by the press contact. Lastly, for the simulation of the mold with a polycarbonate window, two different convection coefficients could be used at the mold walls.

## 5.4 Characterization models

The viscosity model is not the only model that can be improved by extended characterisation range. All other feedstock properties can be modeled as a function of temperature and pressure. The next sub-chapter is a discussion about modeling properties of the feedstock.

### 5.4.1 Results summary

Although many feedstock properties were characterized for a wide temperature range, the majority of the properties used for simulation were considered constant: a density of 6.2 g/cm<sup>3</sup>, a specific heat of 0.5 J/g·°C and a thermal conductivity of 10.912 W/m·°C.

For the density, the constant value of the pycnometer was used because no apparatus to measure the impact of the temperature and the pressure (PVT) at appropriate operating parameters was found. The specific heat was set to a constant value since only slight variations were observed in the experimental data for the complete operational range of temperature. Note that no latent heat model was used or included in the specific heat. Finally, as the thermal conductivity depends on the density and specific heat (see equation (2.20)), it was also set to a constant value.

Results from the sensitivity analysis showed that the specific heat has a large impact on the simulation results. While the density and thermal conductivity seems to have lesser impact on key simulation outputs.

### 5.4.2 Improvements suggestions

Ideally, a model for each feedstock properties should be implemented in the simulation code:  $\rho(T, p)$ ,  $C_p(T)$  and  $k(T)$ . Some models could be built with data provided by the current work, except for the density model for which not enough data was acquired. A PVT apparatus with the lower operational pressure would be needed to get an accurate density model. One could possibly use the presented apparatus at higher pressures to obtain additional data and extrapolate the density behavior at lower pressure. The pycnometer density could be also used as a reference value around the atmospheric pressure and

temperature. Such extrapolation would not require a special apparatus and would give an approximation for the density model implementation.

A method to simulate the latent heat should be studied to define if it can be neglected during the filling of the mold. This could be done by increasing the value of specific heat substantially in the model at the solidification temperature. Adding the latent heat generation in the simulation should reduce the filling time by increasing the mean temperature. Thus, such a model would not increase the current simulation correlation.

A final suggestion concerns the segregation. All characterized feedstock properties are affected by solid loading variation. In order to accurately simulated segregation during filling, studying the impact of the solid loading on these properties is essential. Solid loading variations could be included for the next characterization works for simulation enhancement.

## 5.5 Mesh

The next and last discussion point is related to the discretization mesh.

### 5.5.1 Results summary

A limited convergence study was performed for the current work. Three meshes were tested for the PF505171 mold: a coarse mesh with 267 408 elements, a medium mesh with 576 720 elements and a fine mesh with 1 393 092 elements. The difference between the coarser and finer mesh (5.2 times more elements) was -3.35% for the filling time and less than -0.1% for the maximum temperature. The mesh refinement was thus excluded of the major causes of non-correlation.

The mesh used for majority of the simulation was made with 373 228 elements; in-between the coarser and medium mesh of the convergence analysis and without refinement near the walls. Figure 5.6 illustrates this mesh. Nevertheless, during the study of various temperature models for the viscosity (see section 4.1.3.3), solution convergence was not reached with this mesh. A refined mesh with boundary layers was needed (see Figure 5.7) to simulate the increased temperature dependency of the viscosity model.

To control the number of element precisely near the wall in the meshing software, some geometric feature had to be excluded. This simplification was needed since no boundary layer meshing was available in the software at that time.

### 5.5.2 Improvements suggestions

To capture accurately high velocity and temperature gradients near the walls, boundary layer refinement must be added to the mesh. One should look for a better CFD mesher with the boundary layer refinement feature for the continuity of this project.

If new models are implemented in the simulation, the convergence should be studied again to define an appropriate number of elements. Especially if a steeper temperature dependency is used in the viscosity model.

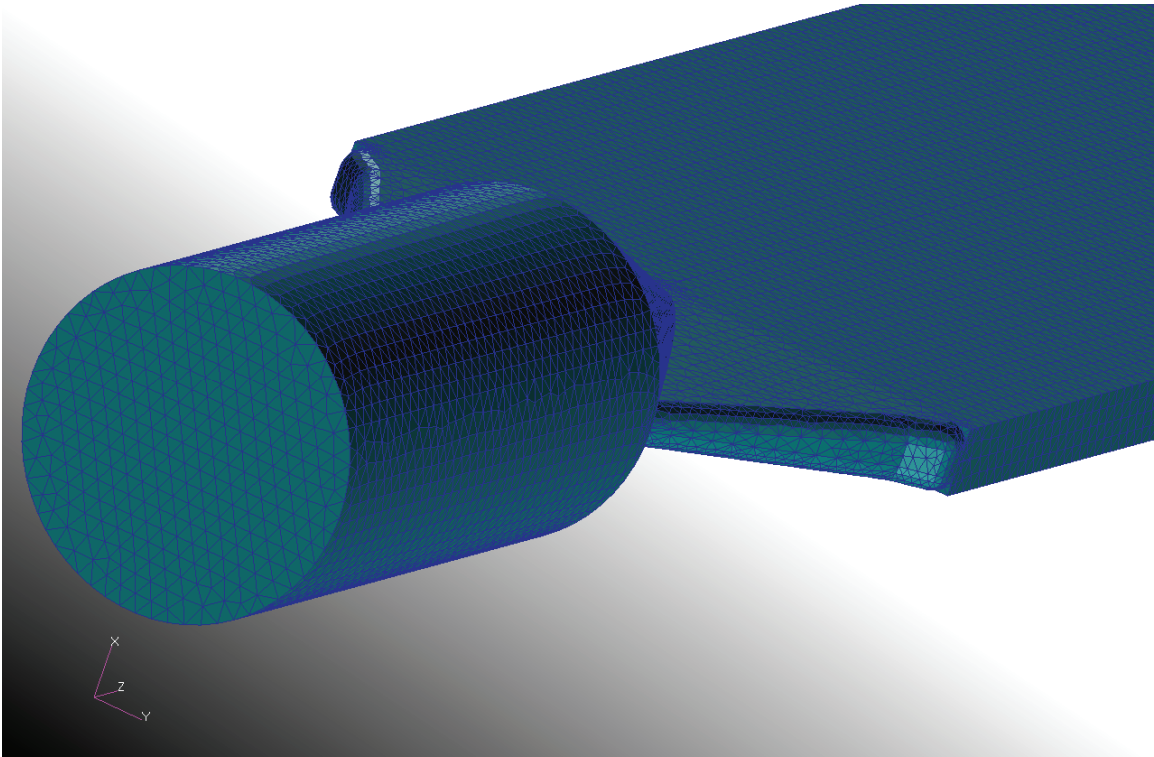


Figure 5.6 Simulation mesh including all geometric features for the PF505171 mold.

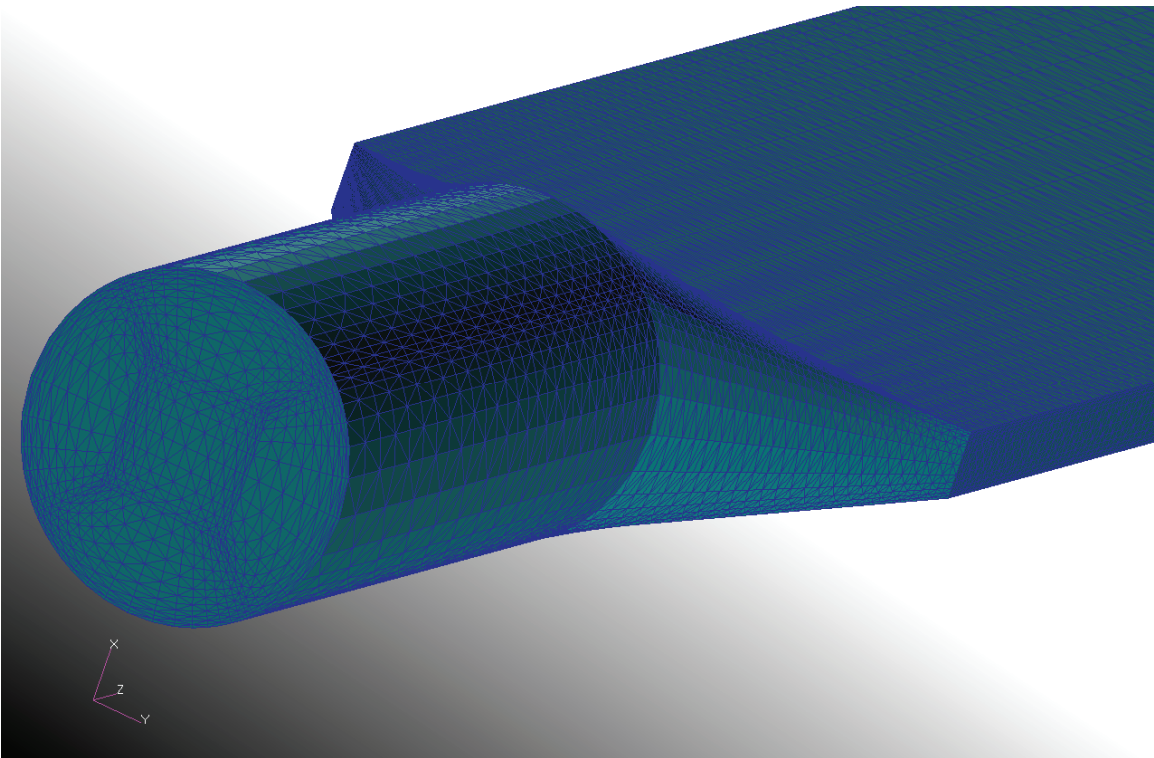


Figure 5.7 Refined and simplified mesh with boundary layers for the PF505171 mold.

## 5.6 Final thoughts

The present results can be useful despite the lack of correlation between the simulation and experimentation obtained so far. For example, the results could be used to help understand the filling behavior of feedstock inside the mold. Data acquired from thermocouples, pressures sensors and high speed camera give information normally unknown to the operators and designers.

Also, the sensitivity results could be useful to analyse injection defects and to predict the impact of changing the feedstock properties. In particular if a different metal is chosen to make the feedstock.

Likewise, the experimental relation between the initial mold temperatures and the filling time is worthy information for mold design. Since the impact of the temperature is quantified, the mold temperature control could be selected to obtain the desired repeatability.

Another example of how to use the experimental data would be for validation of a new injection press or the quality control of the process. Data from the instrumented mold could be used to compare the level of pressure and temperature of a press prior to injection. This would be sensitive enough to detect process deviations without the need for feedstock characterization.

For the next feedstock characterization, the improvements suggestions can provide a guideline to select the right specifications prior to selecting a new methodology or apparatus. Like for the range of shear rate for the viscosity characterization of P&WC feedstock.

Last but not least, these results will accelerate subsequent simulation validation. A great amount of experimental data is already available for the continuity of this project, so one can put more effort on characterization and simulation.

These are just a few examples of how to use the results of this work. It is important to mention that simulation is clearly possible and little work is left to develop this valuable

tool. If a better viscosity characterization can be obtained, correlation is expected with only slight modifications to the simulation parameters.

## CONCLUSION

The objective of this project was to find and validate software for the simulation of the injection step of the MIM process. To perform this task, many characterization tests and experimental acquisitions were required.

First, software suitable for MIM was selected following a literature review on available numerical tools with published results. Plasview3D was selected for its three-dimensional and segregation capabilities. Second, the feedstock properties required for simulation were characterized with various apparatus. These properties are the viscosity, density, specific heat and thermal conductivity. Third, molds were modified to acquire experimental data on the process. One mold was instrumented with pressure sensors and thermocouples and a second mold incorporated a polycarbonate clear part for visualization. A special acquisition system was built to transform the sensor signals into numerical data. Fourth, various tests were performed with the modified molds to obtain data for simulation validation. During these tests, most injection parameters were studied and a repeatability test was performed. Finally, with the characterization results, simulations were executed. Despite several trials, a satisfactory correlation between simulation and experimentation was not achieved. Although, many suggestions have been made to improve this correlation.

The analysis of the results presented in this work led to the following conclusions about injection simulation of the MIM process used by P&WC:

1. Simulation of this process is possible, but more development work will be needed to get accurate solutions.
2. The presented characterization of the feedstock is not comprehensive enough to match the experimental data with the simulation.
3. The experimental viscosity appears to be underestimated because the best correlation was achieved by using an artificially increased viscosity model in the simulation.

4. Experimentations will be needed to determine if a yield stress needs to be implemented in the viscosity model since the images from the high speed camera showed a plug flow region in the velocity profile.
5. The Cross viscosity model with two temperature-dependent variables correlates well with the experimental data if the time and pressure dependence are neglected.
6. Using a constant pressure at the mold entrance is not perfectly accurate and leads to an underestimation of the numerical filling time. Simulation with the complete press geometry would avoid this source of error.
7. A value of  $10\,000\text{ W/m}^2\cdot\text{°C}$  for the heat transfer coefficient of the molds seems to be a good approximation. However, this coefficient approximation will need to be re-adjusted when a new comprehensive rheology model is implemented in the simulation.
8. The melt temperature and the viscosity have a large impact on the simulated filling time while the specific heat strongly affects the cooling rate based on the sensitivity analysis.

This work also led to more general conclusions regarding the MIM process used by P&WC:

9. Controlling the mold temperature during injection is crucial to obtain repeatable results.
10. The instrumented mold developed for this work could be a valuable tool for quality control of the process or for validating of a new press.
11. Polycarbonate parts can be successfully integrated in P&WC's molds for visualization purposes.
12. No jetting occurs during the filling of traction bar for the injection press used in this work relying on the high speed camera images.

The goal of this work is thus achieved: promising software was selected, tested and validated through experimental data. Even if the simulation results did not match the

experimental measurements, many improvements could be made by adding more effort and time to pursue this project. When a good level of accuracy will be reached with the simulation, it will help greatly the development of this process.

## REFERENCES

- [1] R. M. German and A. Bose, *Injection Molding of Metal and Ceramics*. Princeton: MPIF, 1997.
- [2] R. M. German, *Powder Metallurgy & Particulate Materials Processing*. Princeton: MPIF, 2005.
- [3] M. R. Kamal, *et al.*, *Injection Molding Technology and Fundamentals*. Munich: Hanser, 2009.
- [4] R. B. Bird, *et al.*, *Transport Phenomena*, Second ed. New York: John Wiley & Sons, Inc., 2002.
- [5] J. Blazek, *Computational Fluid Dynamics: Principles and Applications*. Kidlington: ELSEVIER SCIENCE Ltd, 2001.
- [6] A. Fortin and A. Garon, *Les éléments finis: de la théorie à la pratique*: Not published, 2007.
- [7] H. Schlichting, *Boundary-Layer Theory*, Seventh ed.: McGraw-Hill, 1979.
- [8] Z. S. Zheng and X. H. Qu, "Numerical simulation of powder injection moulding filling process for intricate parts," *Powder Metallurgy*, vol. 49, pp. 167-172, 2006.
- [9] S. K. Samanta, *et al.*, "A numerical study of solidification in powder injection molding process," *International Journal of Heat and Mass Transfer*, vol. 51, pp. 672-682, 2008.
- [10] H. Yin, *et al.*, "Computational simulation and experimental analysis of the mold-filling process in  $\mu$ PIM," *Journal of Micromechanics and Microengineering*, vol. 21, 2011.
- [11] M. Jenni and T. Wilfinger, "PIMSIM: optimisation of powder injection moulding using advanced moulding simulations," *Powder Metallurgy*, vol. 52, pp. 279-281, 2009.
- [12] I. Andrews, *et al.*, "A Case Study on Computational Fluid Dynamics Analysis of Micro-MIM Products," *Powder Injection Moulding International*, vol. 4, pp. 55-65, 2010.
- [13] F. Petzoldt, *et al.*, "Broadening the Scope of MIM," *Materials and Manufacturing Processes*, vol. 12, pp. 691-711, 1997.
- [14] Cornell University. (20/07/2011). Available: <http://www.research.cornell.edu/VPR/SBD/companies/moldflow-corporation/>
- [15] Z.-x. Zheng, *et al.*, "Numerical simulation of tungsten alloy in powder injection molding process," *Transactions of Nonferrous Metals Society of China*, vol. 18, pp. 1209-1215, 2008.
- [16] V. V. Bilovol, *et al.*, "Comparison of numerical codes for simulation of powder injection moulding," *Powder Metallurgy*, vol. 46, pp. 55-60, 2003.
- [17] S. V. Atre, *et al.*, "Process simulation of powder injection moulding: identification of significant parameters during mould filling phase," *Powder Metallurgy*, vol. 50, pp. 76-85, 2007.
- [18] R. Urval, *et al.*, "CAE-based process design of PIM for microfluidic device components," *Powder Injection Moulding International*, vol. 1, pp. 7-12, 2007.
- [19] S. Ahn, *et al.*, "Integrated filling, packing and cooling CAE analysis of powder injection moulding parts," *Powder Metallurgy*, vol. 51, pp. 318-326, 2008.
- [20] S. Ahn, *et al.*, "Application of a simulation tool in powder injection moulding," *Powder Injection Moulding International*, vol. 3, pp. 60-65, 2009.

- [21] F. Ilinca, *et al.*, "Three-dimensional filling and post-filling simulation of metal injection molding," *Journal of Injection Molding Technology*, vol. 6, pp. 229-238, 2002.
- [22] F. Ilinca, *et al.*, "Metal injection molding: 3D modeling of nonisothermal filling," *Polymer Engineering & Science*, vol. 42, pp. 760-770, 2002.
- [23] F. Ilinca and J. F. Héту, "Three-dimensional free surface flow simulation of segregating dense suspensions," *International Journal for Numerical Methods in Fluids*, vol. 58, pp. 451-472, 2008.
- [24] R. J. Phillips, *et al.*, "A constitutive equation for concentrated suspensions that accounts for shear-induced particle migration," *Physics of Fluids A: Fluid Dynamics*, vol. 4, pp. 30-40, 1992.
- [25] F. Ilinca, *et al.*, "Three-dimensional numerical modeling of segregation in powder injection molding," presented at the Advances in Powder Metallurgy & Particulate Materials, Las Vegas, 2009.
- [26] Y. Thomas, *et al.*, "Development of titanium dental implant by MIM : Experiments and simulation," presented at the Advances in Powder Metallurgy & Particulate Materials, Las Vegas, 2009.
- [27] T. H. Kwon and J. B. Park, "Finite element analysis modeling of powder injection molding filling process including yield stress and slip phenomena," *Polymer Engineering & Science*, vol. 35, pp. 741-753, 1995.
- [28] C. J. Hwang and T. H. Kwon, "A full 3D finite element analysis of the powder injection molding filling process including slip phenomena," *Polymer Engineering & Science*, vol. 42, pp. 33-50, 2002.
- [29] V. V. Bilovol, *et al.*, "The effect of constitutive description of PIM feedstock viscosity in numerical analysis of the powder injection moulding process," *Journal of Materials Processing Technology*, vol. 178, pp. 194-199, 2006.
- [30] S. Turenne, "Détermination des propriétés rhéologiques de mélanges de poudre de IN625 et de liant pour simulation numérique dans ProCAST," Pratt & Whitney Canada, Internal Report, 2007.
- [31] S. Turenne, "Conditions de moulage de mélanges de poudre de IN625 et de liant et validation par simulation numérique dans ProCAST," Pratt & Whitney Canada, Internal Report, 2007.
- [32] M. Thornagel, "Simulating flow can help avoid mould mistakes," *Metal Powder Report*, vol. 65, pp. 26-29, 2010.
- [33] J. C. Gelin, *et al.*, "Experiments and Computational Modeling of Metal Injection Molding for Forming Small Parts," *CIRP Annals - Manufacturing Technology*, vol. 48, pp. 179-182, 1999.
- [34] J.-C. Gelin, *et al.*, "Improved mould design in metal injection moulding by combination of numerical simulations and experiments," *Proceedings of the Institution of Mechanical Engineers, Part B: Journal of Engineering Manufacture*, vol. 216, pp. 1533-1547, December 1, 2002 2002.
- [35] T. Barrière, *et al.*, "Improving mould design and injection parameters in metal injection moulding by accurate 3D finite element simulation," *Journal of Materials Processing Technology*, vol. 125-126, pp. 518-524, 2002.

- [36] T. Barriere, "Determination of the optimal process parameters in metal injection molding from experiments and numerical modeling," *Journal of Materials Processing Technology*, vol. 143-144, pp. 636-644, 2003.
- [37] J. C. Gelin, *et al.*, "Processing Defects and Resulting Mechanical Properties After Metal Injection Molding," *Journal of Engineering Materials and Technology*, vol. 132, pp. 011017-9, 2010.
- [38] Don W. Green and R. H. Perry, *Perry's Chemical Engineers' Handbook*, 8th ed.: McGraw-Hill, 2008.
- [39] J. F. Steffe, *Rheological Methods in Food Process Engineering*, second ed. East Lansing: Freeman Press, 1996.
- [40] C. W. Macosko, *RHEOLOGY Principles, Measurements, and Applications*. New York: WILEY-VCH, 1994.
- [41] B. Huang, *et al.*, "The rheology of metal injection molding," *Journal of Materials Processing Technology*, vol. 137, pp. 132-137, 2003.
- [42] J. Aho and S. Syrjälä, "Measurement of the pressure dependence of viscosity of polymer melts using a back pressure-regulated capillary rheometer," *Journal of Applied Polymer Science*, vol. 117, pp. 1076-1084, 2010.
- [43] J. Z. Liang, "Pressure effect of viscosity for polymer fluids in die flow," *Polymer*, vol. 42, pp. 3709-3712, 2001.
- [44] F. Ilinca and J.-F. Héту, "Three-dimensional free surface flow simulation of segregating dense suspensions," *International Journal for Numerical Methods in Fluids*, vol. 58, pp. 451-472, 2008.
- [45] C. Binet, *et al.*, "Experimental and numerical analysis of metal injection molded products," *Journal of Materials Processing Technology*, vol. 164-165, pp. 1160-1166, 2005.
- [46] Z. Y. Liu, *et al.*, "Characterization of powder injection molding feedstock," *Materials Characterization*, vol. 49, pp. 313-320, 2002.
- [47] L. Kowalski and J. Duszczuk, "Specific heat of metal powder-polymer feedstock for powder injection molding," *Journal of Materials Science Letters*, vol. 18, pp. 1417-1420, 1999.
- [48] L. Kowalski, *et al.*, "Thermal conductivity of metal powder-polymer feedstock for powder injection moulding," *Journal of Materials Science*, vol. 34, pp. 1-5, 1999.
- [49] S. R. SUBIA, *et al.*, "Modelling of concentrated suspensions using a continuum constitutive equation," *Journal of Fluid Mechanics*, vol. 373, pp. 193-219, 1998.
- [50] M. S. Ingber, *et al.*, "An improved constitutive model for concentrated suspensions accounting for shear-induced particle migration rate dependence on particle radius," *International Journal of Multiphase Flow*, vol. 35, pp. 270-276, 2009.
- [51] H. Yokoi, *et al.*, "Visualization analysis of flow front behavior during filling process of injection mold cavity by two-axis tracking system," *Journal of Materials Processing Technology*, vol. 130-131, pp. 328-333, 2002.
- [52] L. Piche, *et al.*, "Ultrasonic Characterization of Polymers Under Simulated Processing Conditions," Canada Patent US 4,754,645, 1988.
- [53] M. Thornagel, "Injection moulding simulation: New developments offer rewards for the PIM industry," *Powder Injection Moulding International*, vol. 6, pp. 65-68, 2012.

- [54] D. Torkar, *et al.*, "Apparent viscosity prediction of alumina–paraffin suspensions using artificial neural networks," *Journal of Materials Processing Technology*, vol. 203, pp. 208-215, 2008.
- [55] F. Ilinca and J.-F. Héту, "Finite element solution of three-dimensional turbulent flows applied to mold-filling problems," *International Journal for Numerical Methods in Fluids*, vol. 34, pp. 729-750, 2000.
- [56] S.-W. Kim and L.-S. Turng, "Developments of three-dimensional computer-aided engineering simulation for injection moulding," *Modelling and Simulation in Materials Science and Engineering*, vol. 12, pp. S151-S173, 2004.
- [57] F. Ilinca and J.-F. Héту, "Three-dimensional simulation of multi-material injection molding: Application to gas-assisted and co-injection molding," *Polymer Engineering & Science*, vol. 43, pp. 1415-1427, 2003.
- [58] G. A. A. V. Haagh, *et al.*, "A 3-D finite element model for gas-assisted injection molding: Simulations and experiments," *Polymer Engineering & Science*, vol. 41, pp. 449-465, 2001.

## APPENDIX 1 – Moving average C# program

```

using System;
using System.Collections.Generic;
using System.ComponentModel;
using System.Data;
using System.Drawing;
using System.Linq;
using System.Text;
using System.Windows.Forms;
using System.IO;

namespace big_file
{
    public partial class frmMain : Form
    {
        public frmMain()
        {
            InitializeComponent();
        }

        private double convertDouble(string v)
        {
            try
            {
                string sepDecimal =
System.Globalization.CultureInfo.CurrentCulture.NumberFormat.NumberDecimalSeparator;
                v = v.Replace(".", sepDecimal);
                v = v.Replace(",", sepDecimal);
                return Convert.ToDouble(v);
            }
            catch (Exception ex)
            {
                // Logger.LogInfo(ex);
                MessageBox.Show(ex.ToString());
                return 0;
            }
        }

        private void paseFile()
        {
            double strValueAverage;
            int NblineAverage = 10;
            int firstCol = 1;
            int lastCol = 12;
            int byPassLine = 2;
            string text_line;
            char[] delimiterChars = { '\t' };

            try
            {
                string file_name = this.txtFileToParse.Text; // string file_name = @"c:\temp\2 test.txt";
                NblineAverage = Convert.ToInt32(this.txtSampleSize.Text);
                double[,] strValue = new double[NblineAverage+1, 20];

                lastCol = Convert.ToInt32(this.txtLastColumn.Text);
                byPassLine = Convert.ToInt32(this.txtLineByPass.Text);

                string file_name_out = file_name.Replace(".TXT", "_out.TXT");
                file_name_out = file_name.Replace(".txt", "_out.txt");

                StreamReader freader = File.OpenText(file_name);
            }
        }
    }
}

```

```

// by-pass 2 first lines
for (int i = 0; i < byPassLine; i++)
{
    freader.ReadLine();
}

StreamWriter fwriter = File.CreateText(file_name_out);
int lineNo = 1;
while ((text_line = freader.ReadLine()) != null)
{
    string[] words = text_line.Split(delimiterChars);
    for (int col = firstCol; col < (lastCol+1); col++)
    {
        if (col == 1)
        {
            words[0] = words[0].Replace("+0", "");
            strValue[lineNo, col] = TimeSpan.Parse(words[0]).TotalSeconds +
this.convertDouble(words[col]) / 1000;
        }
        else
        {
            strValue[lineNo, col] = this.convertDouble(words[col]);
        }
    }

    if (lineNo == NblineAverage)
    {
        // Average

        for (int col = firstCol; col < (lastCol+1); col++)
        {
            strValueAverage = 0;
            for (int j = 1; j < (NblineAverage+1); j++)
            {
                strValueAverage = strValueAverage + strValue[j, col];
            }
            strValueAverage = strValueAverage / NblineAverage;

            fwriter.Write(strValueAverage);
            if (col < (lastCol+1))
            {
                fwriter.Write("\t");
            }
        }
        fwriter.WriteLine();
        lineNo = 1;
    }
    else
    {
        lineNo++;
    }
}
// must explicitly close the readers
freader.Close();
fwriter.Close();
MessageBox.Show("Terminated! Ouput file is " + file_name_out);
}

catch (Exception ex)
{
    MessageBox.Show(ex.ToString());
}
finally
{
    // dispose
}
}

```

```
private void btQuit_Click(object sender, EventArgs e)
{
    Application.Exit();
}

private void btLaunch_Click(object sender, EventArgs e)
{
    Cursor.Current = Cursors.WaitCursor;
    this.paseFile();
    Cursor.Current = Cursors.Default;
}
}
```

## APPENDIX 2 – AR-2000 complete settings

PWME-10-34\_1.8Tg\_steady shear\_2sept-0015f  
 02/09/2010 6:12:46 PM

Sample name PWME-10-34\_1.8Tg\_steady shear\_2sept  
 Sample notes  
 Experiment notes Conditioning  
 Run shorter with feedstock PWME-10-34 @ 1.8Tg  
 Vane + serrated cup  
 Operator Default User

Sample density 1.000 g/cm<sup>3</sup>  
 Results file name PWME-10-34\_1.8Tg\_steady shear\_2sept  
 Run number 15  
 Results directory C:\Documents and Settings\Ar2000\My Documents\Data\Frederic&Vincent\2-09-2010  
 Experiment was run on 02/09/2010 6:17:49 PM

Procedure name Flow procedure  
 Procedure notes  
 Step name Conditioning Step  
 Step notes

Perform step Yes  
 Initial temperature 1.8 Tg  
 Wait for correct temperature Yes  
 Do set temperature Yes  
 Wait for normal force No  
 Perform pre-shear Yes  
 Pre-shear variable 100.0 1/s  
 Pre-shear duration 0:05:00 hh:mm:ss  
 Motor mode auto

Perform equilibration Yes  
 Equilibration duration 0:01:00 hh:mm:ss  
 Wait for zero velocity No  
 Control normal force Uses current instrument settings

Purge gas only No  
 Step name Steady state flow step  
 Step notes

Perform step Yes  
 Ramp type Steady state flow  
 Start controlled variable shear rate 0.1000 1/s  
 End controlled variable shear rate 1000 1/s  
 Ramp mode log  
 Points per decade 7

Temperature 1.8 Tg  
 Wait for temperature Yes  
 Sample period 0:00:06 hh:mm:ss  
 Percentage tolerance 5.0  
 Consecutive within tolerance 3  
 Maximum point time 0:00:05 hh:mm:ss  
 Motor mode auto  
 Step name Post-Experiment Step  
 Step notes  
 Perform step No  
 Set temperature system idle No  
 Geometry name vane-serrated cup  
 Geometry notes vane-serrated cup  
 Geometry material Aluminum  
 Stator inner radius 15.30 mm  
 Rotor outer radius 14.00 mm  
 Cylinder immersed height 50.00 mm  
 gap 8000 micro m  
 Gap offset 0 micro m  
 Geometry inertia 16.13 micro N.m.s<sup>2</sup>  
 Gap temperature compensation 0 micro m/°C  
 Gap temperature compensation enabled No  
 Shear rate factor 11.29  
 Shear stress factor 14920 1/m<sup>3</sup>  
 Measurement system factor 1321 1/m<sup>3</sup>  
 Fluid density factor 3.733E-10 m<sup>5</sup>  
 Normal force factor 1.000 1/m<sup>2</sup>  
 Backoff distance 90000 micro m  
 Approximate sample volume 38.14 ml  
 Gap zero mode Normal force - 1.000 N  
 Sample compression Normal force - 50.00 N  
 Compression distance 1000.0 micro m  
 Compression velocity 100.0 micro m/s  
 Fine velocity 1000.0 micro m/s  
 Coarse velocity 3000.0 micro m/s  
 Other velocity 3000.0 micro m/s  
 Current temperature system Peltier concentric cylinders  
 Temperature control Enabled  
 Purge gas only No  
 Temperature calibration Peltier plate - 0 micro m/°C  
     Torsion oven - plate - 0 micro m/°C  
     Torsion oven - solid sample - 0 micro m/°C

Peltier concentric cylinders - 0 micro m/°C  
 None - 0 micro m/°C  
 Stress relaxation - 0 micro m/°C  
 Cooling water temperature 0 °C  
 Cooling water range 0 °C  
 Bearing friction correction Yes  
 Bearing friction 0.968 micro N.m/(rad/s)  
 Bearing offset 0 micro N.m  
 Temperature system span and offset Peltier plate - span 1.0000 , offset 0.4000 °C  
 Torsion oven - plate - span 1.0000 , offset 0.0300 °C  
 Torsion oven - solid sample - span 1.0000 , offset 0 °C  
 Peltier concentric cylinders - span 1.0330 , offset -0.4740 °C  
 None - span 1.0000 , offset 0 °C  
 Stress relaxation - span 1.0000 , offset 0 °C  
 Bearing mapping type precision  
 Number of mapping iterations 2  
 Last mapping date 02/09/2010 2:40:36 PM  
 Last mapping geometry vane-serrated cup  
 MType AR-2000  
 Version 7.20 03/10/06  
 Cnf version 301  
 Prm version 301  
 PCB Number \*NOT\_SET\*  
 Comms port COM1  
 Baud rate 9600  
 Software version V5.1.17  
 Windows version Windows XP 5.1 (Service Pack 3)  
 Instrument inertia 3.605 micro N.m.s<sup>2</sup>  
 Auto increment run number Yes  
 Prompt for file name at start of run Yes  
 Auto save results file Yes  
 Results file storage Consecutive steps of same type to 1 file  
 Temperature tolerance 0.2 °C  
 Temperature duration 0:00:10 hh:mm:ss  
 Wait for temperature even if OK Yes  
 Gap tolerance 4 micro m  
 Gap duration 0:00:02 hh:mm:ss  
 Override wait for gap No  
 Velocity tolerance 0.1000 rad/s  
 Zero speed after pre-shear Leave as is  
 Zero normal force before run No  
 Zero timer before run Before pre-shear

Non-equilibrium minimum velocity 1.000E-4 rad/s  
Zero strain at the start of each flow step Yes  
Inertia correction No  
Collect negative shear rate data if stress is positive Yes  
Collect all points No  
Display flow point graph during run Yes  
Store flow point graph with results Yes  
Creep zero displacement Yes  
Display oscillation waveform graph during run Yes  
Store oscillation waveform graph with results Yes  
Display strain control tries during run Yes  
Store strain control tries with results Yes  
Stress relaxation zero displacement Yes  
Flow torque limit 10.00 micro N.m  
Flow velocity limit 1.000E-3 rad/s  
Oscillation torque limit 5.00 micro N.m  
Oscillation displacement limit 1.00E-5 rad  
Oscillation raw phase limit 170.0 degrees  
Oscillation minimum normal force limit 0.1000 N  
Oscillation maximum normal force limit 50.00 N  
Flow velocity tolerance 5.00 %  
Oscillation torque tolerance 1.00 %  
Oscillation displacement tolerance 5.00 %  
Oscillation velocity tolerance 5.00 %  
Temperature tolerance 1.0 °C

# APPENDIX 3 – Detailed summary of the simulations

	Dimensionless Simulation Parameters								Viscosity models				Mesh					
	Inlet Pressure	Melt Temp. (% of T <sub>g</sub> )	Mold Temp. (% of T <sub>g</sub> )	Density	Specific Heat	Thermal Conductivity	Convection coefficient	Gravity	Poly	ETS	2.5* Poly	Poly+ η <sub>0</sub> =5000 @50°C	Poly+ η <sub>0</sub> =5000 @55°C	Poly+ η <sub>0</sub> =5000 @60°C	Poly+ η <sub>0</sub> =5000 @63°C	Number of elements	Number of nodes	Mesher
Mold	P <sub>i</sub>	1,7	0,8	4	2,2	0,010912	0,0254	-386,0889	X							373228	66873	TetMesh
	P <sub>i</sub>	1,7	0,8	4	4,6	0,010912	0,0254	-386,0889	X							373228	66873	TetMesh
	P <sub>i</sub>	1,7	0,8	4	2,2	0,010912	0,1016	-386,0889	X							373228	66873	TetMesh
	Model	1,7	0,8	4	2,2	0,010912	0,0254	-386,0889	X		X					373228	66873	TetMesh
	Model	1,7	0,8	4	2,2	0,010912	0,0254	-386,0889	X							373228	66873	TetMesh
	Model	1,4	0,8	4	2,2	0,010912	0,0254	-386,0889	X							373228	66873	TetMesh
	Model	1,4	0,8	4	2,2	0,010912	0,254	-386,0889	X							373228	66873	TetMesh
	P <sub>i</sub>	1,7	0,8	3,758	2,2	0,010912	0,0254	-386,0889	X							373228	66873	TetMesh
	P <sub>i</sub>	1,4	0,8	4	2,2	0,010912	0,0254	-386,0889	X							373228	66873	TetMesh
	P <sub>i</sub>	1,4	0,8	4	2,2	0,010912	0,254	-386,0889	X							373228	66873	TetMesh
	P <sub>i</sub>	1,4	0,8	4	0,5	0,010912	0,254	-386,0889	X							373228	66873	TetMesh
	P <sub>i</sub>	1,4	0,8	4	2,2	0,010912	0,254	-386,0889	X			X				373228	66873	TetMesh
	P <sub>i</sub>	1,4	0,8	4	0,5	0,010912	0,254	-386,0889					X			373228	66873	TetMesh
	P <sub>i</sub>	1,4	0,8	4	2,2	0,010912	0,254	-386,0889						X		373228	66873	TetMesh
	P <sub>i</sub>	1,4	0,8	4	0,5	0,010912	0,254	-386,0889						X		373228	66873	TetMesh
	P <sub>i</sub>	1,4	0,8	4	0,5	0,010912	0,254	-386,0889							X	1535904	310407	IsoMesh
	P <sub>i</sub>	1,4	0,8	4	0,5	0,010912	0,0254	-386,0889							X	1535904	310407	IsoMesh
	P <sub>i</sub>	1,7	0,8	4	0,5	0,010912	0,0254	-386,0889							X	1535904	310407	IsoMesh
	P <sub>i</sub>	1,4	0,8	4	0,5	0,010912	0,1778	-386,0889							X	1535904	310407	IsoMesh
	P <sub>i</sub>	1,4	0,8	4	0,5	0,010912	0,18034	-386,0889							X	1535904	310407	IsoMesh
	P <sub>i</sub>	1,4	0,8	4	0,5	0,010912	0,18288	-386,0889							X	1535904	310407	IsoMesh
	P <sub>i</sub>	1,4	0,8	4	0,5	0,010912	0,1905	-386,0889							X	1535904	310407	IsoMesh
	P <sub>i</sub>	1,4	0,8	4	0,5	0,010912	0,2032	-386,0889							X	1535904	310407	IsoMesh
	P <sub>i</sub>	1,4	0,8	4	0,5	0,010912	0,2286	-386,0889							X	1535904	310407	IsoMesh
	P <sub>i</sub>	1,4	0,8	4	2,2	0,010912	0,254	-386,0889						X		373228	66873	TetMesh
	P <sub>i</sub>	1,4	0,8	4	0,5	0,010912	0,254	-386,0889						X		373228	66873	TetMesh
	P <sub>i</sub>	1,4	0,8	4	0,5	0,010912	0,254	-386,0889						X		1535904	310407	IsoMesh
	42,9% of P <sub>i</sub>	1,4	0,8	4	2,2	0,010912	0,254	-386,0889			X					373228	66873	TetMesh
	71,4% of P <sub>i</sub>	1,4	0,8	4	2,2	0,010912	0,254	-386,0889			X					373228	66873	TetMesh
	P <sub>i</sub>	1,4	0,8	4	2,2	0,010912	0,254	-386,0889			X					373228	66873	TetMesh
	P <sub>i</sub>	1,4	0,8	4	0,5	0,010912	0,254	-386,0889			X					373228	66873	TetMesh
	Model	1,4	0,8	4	2,2	0,010912	0,254	-386,0889			X					373228	66873	TetMesh
	P <sub>i</sub>	1,3	0,8	4	2,2	0,010912	0,254	-386,0889			X					373228	66873	TetMesh
142,9% of P <sub>i</sub>	1,4	0,8	4	2,2	0,010912	0,254	-386,0889			X					373228	66873	TetMesh	
171,4% of P <sub>i</sub>	1,4	0,8	4	2,2	0,010912	0,254	-386,0889			X					373228	66873	TetMesh	
P <sub>i</sub>	1,4	0,8	4	2,2	0,010912	0,1016	-386,0889	X							373228	66873	TetMesh	
P <sub>i</sub>	1,4	0,8	4	2,2	0,0135	0,0254	-386,0889	X							373228	66873	TetMesh	
P <sub>i</sub>	1,7	0,8	4	2,2	0,010912	0,254	-386,0889		X						373228	66873	TetMesh	
P <sub>i</sub>	1,4	0,8	4	2,2	0,010912	0,254	-386,0889		X						373228	66873	TetMesh	
P <sub>i</sub>	1,7	0,8	4	2,2	0,010912	0,1016	-386,0889		X						373228	66873	TetMesh	
Traction Bar Mold (PF65612)	P <sub>T</sub>	1,4	0,8	4	2,2	0,010912	0,254	-386,0889			X				379235	67731	TetMesh	
	Model	1,4	0,8	4	2,2	0,010912	0,254	-386,0889			X				379235	67731	TetMesh	
	40,0% of P <sub>T</sub>	1,4	0,8	4	2,2	0,010912	0,254	-386,0889			X				379235	67731	TetMesh	
	200,0% of P <sub>T</sub>	1,4	0,8	4	2,2	0,010912	0,254	-386,0889			X				379235	67731	TetMesh	
	240,0% of P <sub>T</sub>	1,4	0,8	4	2,2	0,010912	0,254	-386,0889			X				379235	67731	TetMesh	

\*The yellow highlighting indicates changes from the previous simulation